Advances in 3d-4f Transition Metal Rare Earth

Perovskite Oxides

Ihab Abdel-Latif Abdel-Latif

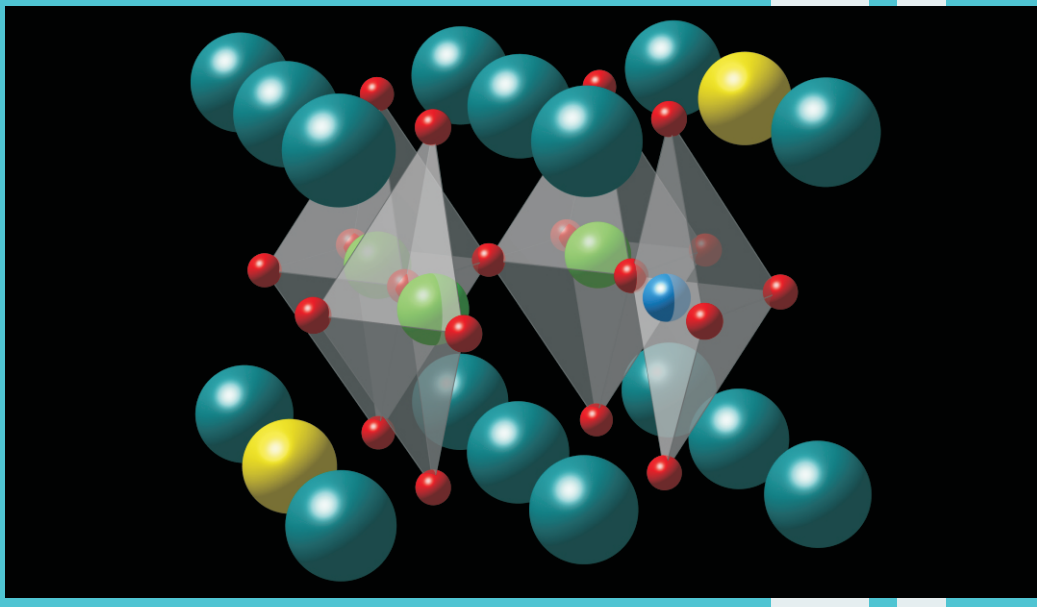

Rare earth manganites
Synthesis
Crystal structure
Perovskites
Semiconductor

SciencePG
Science Publishing Group

Advances in 3d-4f Transition Metal Rare Earth Perovskite Oxides

Ihab Abdel-Latif Abdel-Latif

Najran University

SciencePG
Science Publishing Group

Published by

Science Publishing Group

548 Fashion Avenue
New York, NY 10018, U.S.A.

http://www.sciencepublishinggroup.com

ISBN: 978-1-940366-62-3

Preface

Advances in a 3d-4f oxides are one of the most interesting subjects in the field of materials science which has attracted the scientific community and up till now we found ourselves in front of a new progress and a new applications for these materials.

There is a lake in the text books that deal with these important topics so the idea of this book jumped to me and started working with and I hope to present some of the basics related to these materials.

It is important to highlight on the physical properties of these materials, besides its potential applications. All the presented work and results in this book belong to the keen efforts of the scientists from different places and here in this book, it is collected and presented.

Ihab Abdel-Latif

Najran, November 2015.

To

My Wife

and

My Children

Contents

1

Introduction

Manganites, Ferrites and coblates are the materials which composed of manganese, iron and cobalt respectively so any material in its content manganese is so called manganites. There are many types of compounds in their content exists manganese, for example manganese oxides. In the recent years, a lot of interest has been devoted to research on rare earth manganese oxides, within perovskites-like structure. These rare earth manganese oxides have exciting properties such as the colossal magnetoresistance (CMR) [1] and multiferroic effects [2]. These compounds could be used as a magnetic storage media and magnetic sensors [3-4]. The great attention increased due to the potential applications in spintronics [5-6] and in ferroelectromagnets [7-8].

Perovskites have the general formula ABO_3 where A and B are metallic cations and O is a nonmetallic anion [9]. A is a large cation, similar in size to O^{2-}; B is a small cation such as Mn^{3+} or Mn^{4+}, octahedrally-coordinated by oxygen. In the present case A is rare earth element (Nd, Eu, Sm, …), B is 3d transition metal element (Mn, Fe, Co, …) and O is oxygen. The ideal cubic structure is shown in Fig. 1.1 One can say that the ideal perovskite structure is considered as a cubic close-packed array formed of O^{-2} anions and A^{+3} cations with small B^{+3} cations in octahedral interstitial sites. Partially replacement of rare earth element by divalent element in this compound (a divalent element like Ca, Sr, Ba, …) has been extensively investigated [9]. The ideal, cubic perovskite structure is distorted by cation size mismatch and the *Jahn & Teller effect*, whereby a distortion of the oxygen octahedron surrounding the B site cation splits the energy levels of a 3d ion such as Mn^{3+}, thus lowering the energy. The distorted structures are frequently orthorhombic. So one can say crystal structure of these materials not only has cubic structure but also is found to be in the orthorhombic, rhombohedral, hexagonal.

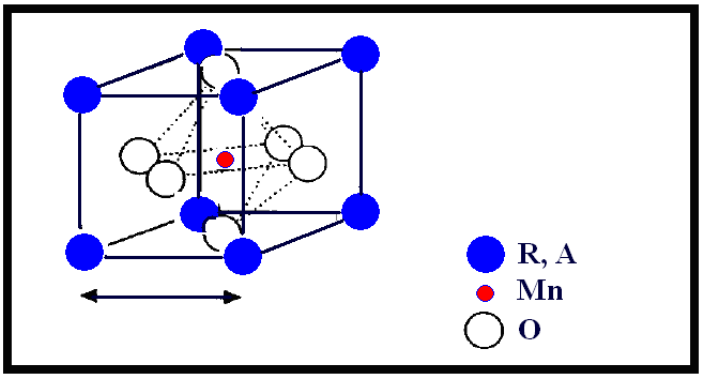

Fig. 1.1 *The ideal, cubic perovskite structure.*

Mixed-valence manganites are solid solutions based on $AMnO_3$ where A is a rare earth ion. [10] In the ABO_3 perovskite structure, Mn is on the B site in octahedral oxygen coordination, with crystal field splitting Δ_{cf} between the t_{2g} and e_g orbitals.

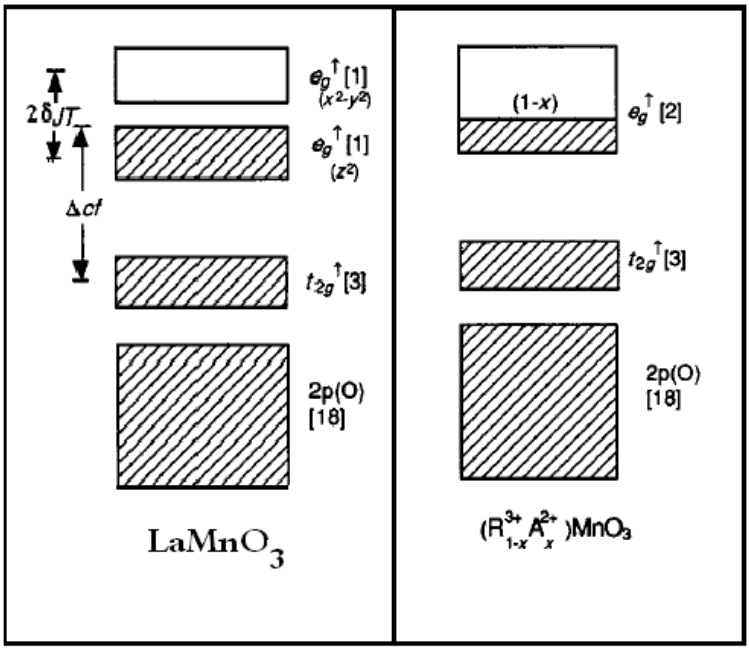

Fig. 1.2 *Schematic band structure of $LaMnO_3$ and $R_{0.7}A_{0.3}MnO_3$.*

The simple cubic perovskite structure undergoes a double distortion in the end member, reducing the symmetry to orthorhombic (O ´structure). There is a buckling of the MnO_6 octahedral array to accommodate the size discrepancy between R^{3+} and O^{2-}, and a chequerboard distortion to the octahedral in the basal plane that is due to the Jahn -Teller effect for Mn^{3+}, which splits the $e^{\uparrow}_{g}$ orbitals (dz^2 and dx^2-y^2). The Jahn-Teller splitting δ_{JT} is slightly greater than the e_g bandwidth W [11]. $LaMnO_3$ is an insulator, with a small activation energy *ca*. 0.1 eV. $LaMnO_3$ is A-type antiferromagnet with a Neel temperature of 130 K. [9]

In particular, the neutron data revealed a very rich magnetic phase diagram where, for different doping levels, antiferromagnetism can take different configurations (A, C, G types) and can even coexist with ferromagnetism (B type). The magnetic structures are indicated on Fig. 1.3. There are three main regions: for small amounts of Mn^4 the compounds have essentially antiferromagnetic properties. For x around 0.3, they become ferromagnetic but, for $x > 0.5$, they revert to antiferromagnetism up to the end-member $CaMnO_3$. From magnetization and susceptibility results, Jonker [9] concluded that the exchange is weakly positive (ferromagnetic) between two 3d4 Mn^{+3} ions, negative (antiferromagnetic) between two 3d3 Mn4 ions and positive between a 3d4 Mn^{+3} and a 3d3 Mn^{+4} ion. These measurements provided the first clear evidence of a ferromagnetic exchange interaction in an oxide. Moreover, resistivity measurements revealed a strong correlation between electron transport and magnetic properties in these oxides. The resistivity is lowest for the $x = 0.3$ composition corresponding to the best ferromagnetism, whereas high resistivities are associated with the antiferromagnetic compositions.

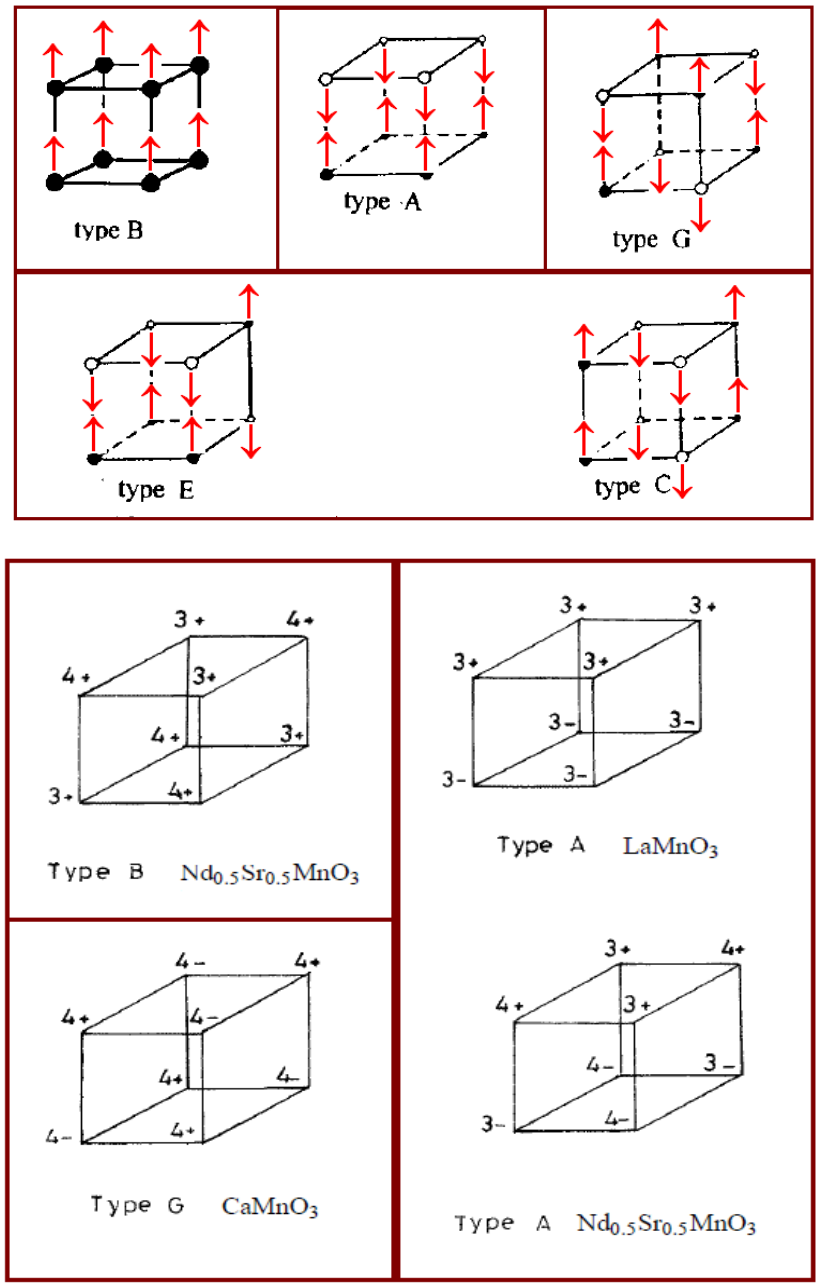

Fig. 1.3 *Magnetic ordering in Perovskites.*

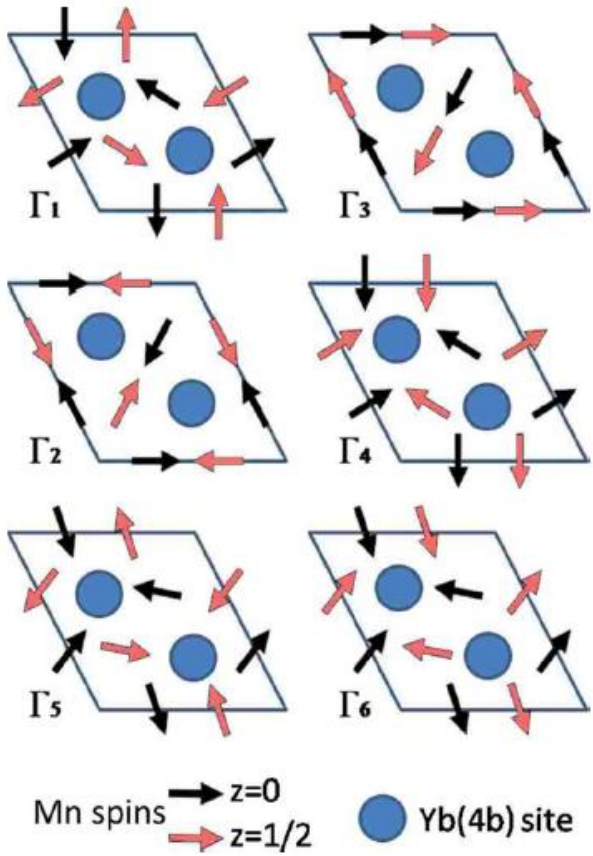

Fig. 1.4 *Symmetry allowed Mn spin orders in hexagonal $RMnO_3$ [12].*

Double exchange concept for rare earth manganites doped with divalent element was developed and explained by Zener in 1951 in terms of his theory of indirect magnetic exchange between 3d atoms was discussed [9]. He considered that the intra-atomic Hund rule exchange was strong and that the carriers do not change their spin orientation when hopping from one ion to the next, so they can only free energy of the system, Zener found that ferromagnetic interactions are favored when the magnetic atoms are fairly well separated and conduction hop if electrons are present. The theory was applied to the manganese perovskites the spins of the two ions are parallel (see fig. 1.5). On minimizing

the total with the aim of explaining the strong correlation between conductivity and ferromagnetism, and the value of the zero-temperature saturation magnetization which corresponds to the sum of all the unpaired electron spins. Starting from the insulating antiferromagnetic $LaMnO_3$ end member where electrons are localized on the atomic orbitals, Zener showed how the system should gradually become more ferromagnetic upon hole doping [9].

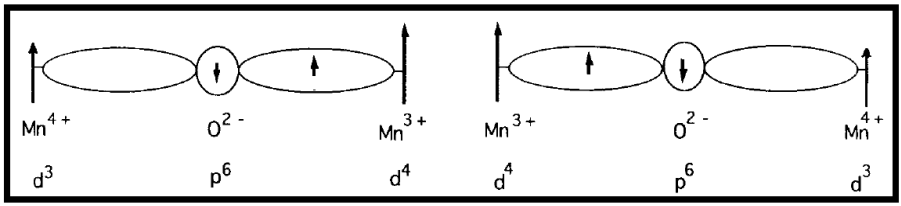

Fig. 1.5 *Schematic diagram of the double-exchange mechanism. The two states Mn^{3+}-Mn^{4+} and Mn^{4+}-Mn^{3+} are degenerate if the manganese spins are parallel [9].*

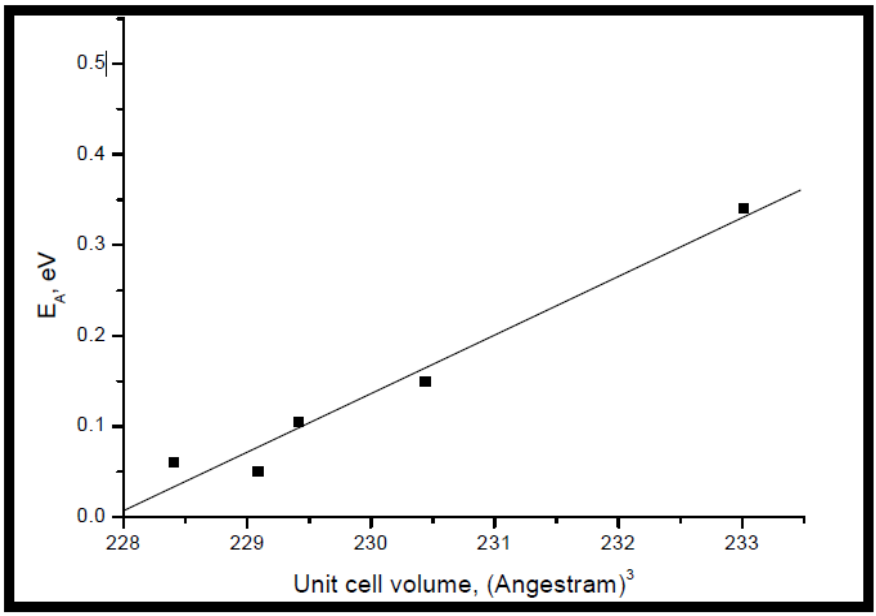

Fig. 1.6 *The activation energy E_A as a function of unit cell volume of $Nd_{0.65}Sr_{0.35}Fe_xMn_{1-x}O_3$.*

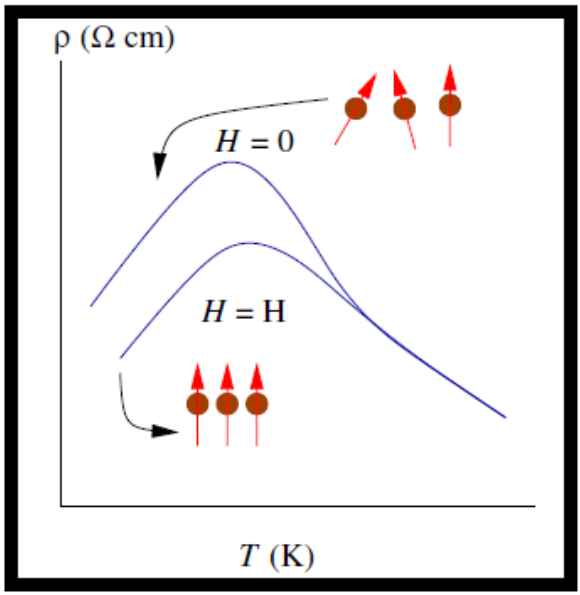

Fig. 1.7 *Effect of Magnetic field on resistivity (Magnetoresistance).*

The correlation between crystal structure and its physical properties plays an important role in understanding and interpretation these interesting phenomena. An example for this correlation between crystal structure and electrical activation energy in $Nd_{0.65}Sr_{0.35}Fe_xMn_{1-x}O_3$ is is represented in Fig. 1.6 which reported by *Abdel-latif et al*., [3]. It is clear that the volume of unit cell is directly proportional to activation energy. Many ferromagnetic elements display an intrinsic negative magnetoresistance in the vicinity of their ferromagnetic transitions. This is because in the vicinity of the ferromagnetic transition, conduction electrons are scattered by magnetic fluctuations. Switching on a magnetic field suppresses such fluctuations and this results in a reduction of such scattering and consequently, a reduction in the electrical resistivity. Magnetoresistance MR is defined as the change in the electrical resistance produced by the application of an external magnetic field. It is usually given as a percentage [1].

$$MR = [(\rho_H - \rho_0) / \rho_0] \times 100\%$$

Where ρ_0 is resistivity with no applied magnetic field and ρ_H is resistivity with o applied magnetic field. For rare-earth cations smaller than Tb^{3+} (*R* = Ho, Er, Tm, Yb, Lu) as well as Y^{3+} and Sc^{3+}, in the rare earth manganites $RMnO_3$ with perovskite structure becomes metastable and a new hexagonal polytype stabilizes (space group $P6_3cm$). In the hexagonal phase, a ferroelectric behavior has been described to coexist with magnetic ordering at low temperature. The ferroelectricity in hexagonal $RMnO_3$ was discovered by *Bertaut*, *Forrat*, and *Fang* in 1963 [12].

All these interests were the main goals to continue in research in this interesting field and the presented review deals mainly with studying different classes of the rare earth manganites; Orthorhombic distorted perovskites and hexagonal perovskites.

2

Synthesis of 3d-4f Oxides

The rare earth manganites are synthesized using different methods. The well known methods for fabrication manganites are solid state reaction, co-precipitation method, hydrothermal reaction method, sol gel method.

2.1 Solid State Method

Solid state reaction method is called conventional method of preparation manganites. In this method pure oxides or carbonates of transition metal and rare earth are mixed together with the proper ratio [13-20].

Let us take an example how to synthesis $SmMnO_3$?

The steps of solid state reaction method could be represented in the schematic diagram shown in Fig. 2.1. First of all, the reaction which is used to get $SmMnO_3$ could be written as follow;

$$0.5(Sm_2O_3) + 0.5(Mn_2O_3) \rightarrow SmMnO_3$$

We need to calculate the atomic weight of each oxide to know how much oxides needed to get $SmMnO_3$ (From periodic table see Fig. 2.2 Atomic Wt (Mn) = 54.93805, Atomic Wt (O) = 15.9994, Atomic Wt (Sm) = 150.36). This is so called calculations step and results are shown in table 2.1.

Table 2.1 *Calculations of initial Oxides.*

	Initial oxides 0.5 (Sm_2O_3)	**Initial oxides 0.5 (Mn_2O_3)**	**Final oxides $SmMnO_3$**
Atomic Wt	174.3591	78.9372	253.2963
(Initial oxides/ Final oxides)	0.6884	0.31164	
Mass	0.6884 g	0.3116 g	1.0000 g

Let us return back to our example to get 1g of $SmMnO_3$ we need to weighting 0.68836g of pure Sm_2O_3 (99.9%) and 0.31164g of pure Mn_2O_3 (99.9%) to mix, then grinding carefully using agate mortar to get homogenous and well mixed

powder. Next step is to press the well mixed powder from initial oxides into disc form or into any other forms (pressure range 2-3 ton). The pressed pelt (disc) is place inside furnace and setting the temperature of the firing at the calcinating temperature of rare earth manganites which in our case starts from 1000°C. The calcinating firing process talks 12h - 24h and could be done in environmental or in the presence of oxygen gas. The obtained disc is grinded again and repeating firing but with increasing firing temperature up to 1100°C in environmental condition or in the presence of oxygen gas. Each time we must test the fired powder using X-Ray diffraction in order to know how much from our phase is formed. The calcination process may be made for the well mixed and grinded powder form without pressing. The last step is to fire the disc formed from our powder at sintering temperature ($T_{sintering} \approx 1200°C - 1400°C$). The instrumental equipments which are used in solid state reaction method are shown in Fig. 2.3. The sintered disc is examined again with X-Ray diffraction to define the structural parameters and carrying out different characterizations (optical, electrical and magnetic transport).

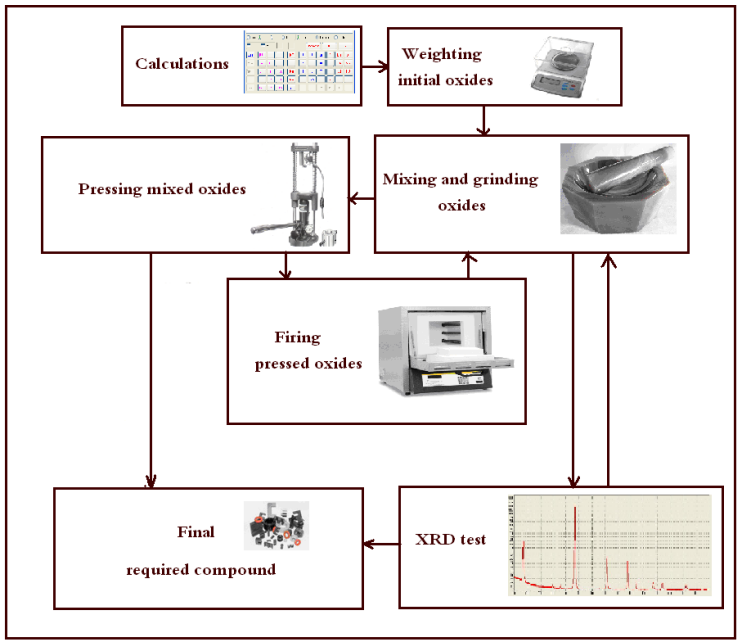

Fig. 2.1 *Schematic representation of the solid state reaction process.*

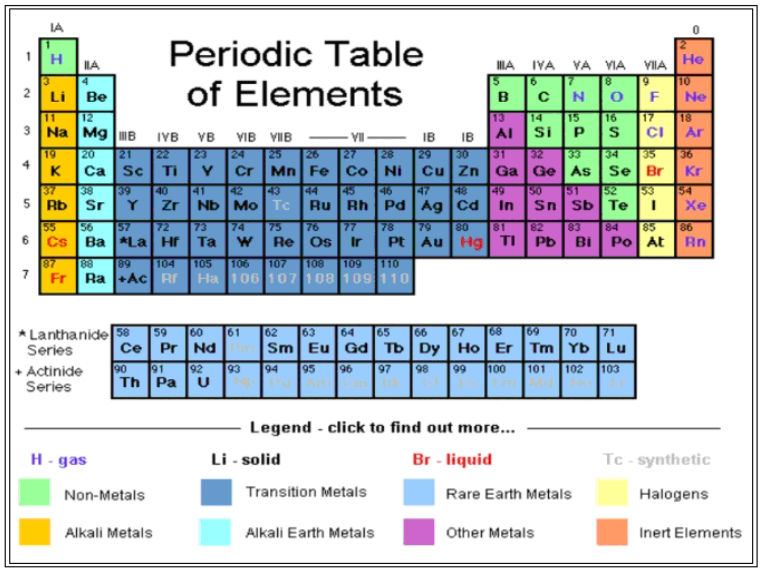

Fig. 2.2 *Periodic table of elements.*

Electronic Balance

Agate Mortar

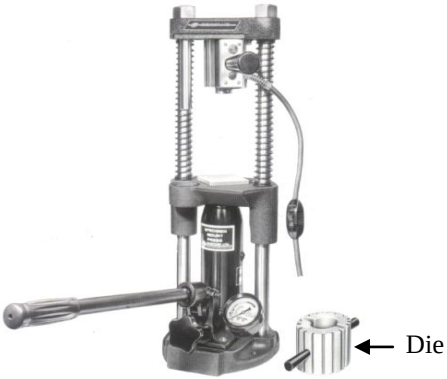

High pressure Press (2o Ton)

Furnace

Fig. 2.3 *Experimental equipements for solid state synthesis.*

2.2. Co-precipitation Method

The synthesis of manganites using chemical reaction methods are widely used in fabrication nano-sized manganites. Co-precipitation [21-30], hydrothermal reaction, sol gel are the well known example chemical reaction method, where we are using chlorides, nitrates or phosphates as initial chemical to start our reaction.

Let us take the same example (synthesis $SmMnO_3$ which we discussed before using solid state reaction) but in this case we apply co-precipitation reaction. Looking at the schematic diagram of chemical reaction process shown in Fig. 2.4, one can realize that we need first to make calculations for how much starting precursors required for beginning our reaction.

Calculations step: 1mol of $SmCl_3.6H_2O$ and 1mol $MnCl_2.4H_2O$ react with 5mol Na(OH). The chemical reaction could be represented as:

$$1mol\ SmCl_3.6H_2O + 1mol\ MnCl_2.4H_2O + 5mol\ Na(OH) \rightarrow 1mol\ SmMnO_3 + 5mol\ NaCl + 10\ mol\ H_2O + 2.5mol\ H_2O$$

The details of calculations are required for chemical reactions are represented below in this table 2.2.

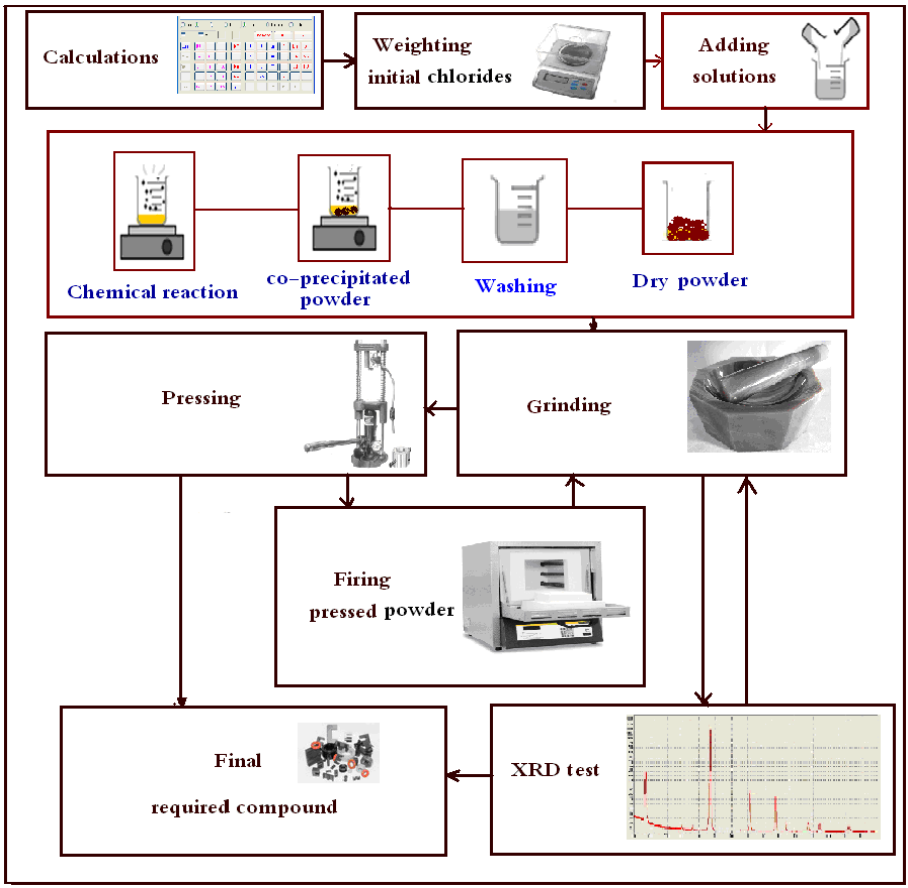

Fig. 2.4 *Schematic representation of the chemical reaction process.*

Electronic balance

pH meter

Magnetic stirrer with hot plate

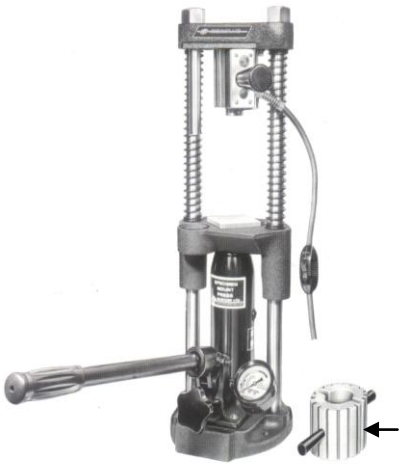

High pressure Press (2o Ton)

Agate mortar

Furnace

Fig. 2.5 *Experimental equipements for chemical synthesis.*

Table 2.2 *Calculations details of chemical reaction.*

$SmCl_3$ =256.7181	$SmCl_3.6H_2O$ =364.8099		NaCl =58.4425	H_2O =18.0153
$MnCl_2$ =125.8435	$MnCl_2.4H_2O$ =197.9047	$SmMnO_3$ =253.29625	5NaCl =292.2125	H_2O =180.153 +45.0383 =225.1913
Na(OH) =39.9971	5Na(OH) =199.9855			
Total	Input =762.7	Output 770.7		

According to our calculation, to get 1g of $SmMnO_3$ we need to take the following weights of starting precursors; 1.4403g of $SmCl_3.6H_2O$, 0.7813g of $MnCl_2.4H_2O$ and 0.7895g Na(OH). One can ask reasonable question; why there is difference in atomic weights of input and output of reaction? The difference in weights is of 0.5 of oxygen weight which equal 8 and it is taken from air.

Following the schematic representation of synthesis process, the next step is to weight starting precursors with the calculated values. Taking into consideration all starting precursors must be of high-purity compounds. After weighting our initial powders the 1.4403g of $SmCl_3.6H_2O$ and the 0.7813g of $MnCl_2.4H_2O$ are dissolved in distilled water (200 mLiter). The 0.7895g Na(OH) is dissolved in distilled water separately to give us alkaline solution. Then this alkaline solution is slowly poured into the solution of metal ion until the pH of the suspension reach ~ 13 to avoid differences in precipitate composition. Digital pH meter is used and you can use any other pH indicators, all experimental equipments required to sensitize our manganites are shown in Fig. 2.5. Looking at the solution when adding alkaline solution we can see the color of solution is changing we see small particles in this solution. The aqueous mixture stirred magnetically for 180-300 minutes at 85℃ using magnetic stirrer. The precipitated Powder composed of our $SmMnO_3$ compound and NaCl compound so we need to dissolve NaCl in water and get red of this NaCl which is dissolved in water. This

step is so called washing process and we are washing for several times using distilled water until the pH value of the solution became neutral, or until get rid of sodium chloride. Finally, the precipitated powder is dried at 90 ℃ for 3h in air using hot plate. The obtained powder grinded using agate mortar to get well disperse $SmMnO_3$ powder and testing it with X-Ray diffraction. After this step you may need to thermal treatment for this powder to form required $SmMnO_3$ structure. The powder is pressed into a disk- shaped form of 13 mm diameter to be sintered in air for 12 hours at different temperatures 650 ℃, 750 ℃, 850 ℃ and 1000 ℃. The sintered pellets constituted the final sample and has certain shape (disc, rectangular, or torrid) to examine (electrical, magnetic, optical, … etc.) properties of our synthesized material according to certain conditions (either heat treatment or chemical reaction).

2.3 Hydrothermal Method

The hydrothermal reaction [31-35] is also one of the well known examples of chemical reaction method, where we can use chlorides, nitrates or phosphates as the initial chemicals to start our reaction. Looking at the schematic diagram of hydrothermal reaction process shown in Fig. 2.6, one can realize that next step after calculations is weighting starting precursors; 1.4403g of $SmCl_3.6H_2O$, 0.7813g of $MnCl_2.4H_2O$ and 0.7895g of Na(OH). After weighting our initial powders the 1.4403g of $SmCl_3.6H_2O$ and the 0.7813g of $MnCl_2.4H_2O$ are dissolved in distilled water (200 mLiter). The 0.7895g Na(OH) is dissolved in distilled water separately to give us alkaline solution. Then this alkaline solution is slowly poured into the solution of metal ion until the pH of the suspension reach ~ 13. The solution is placed inside the hydrothermal reactor and closed tightly and put them together inside furnace with temperature 200°C for 3h.

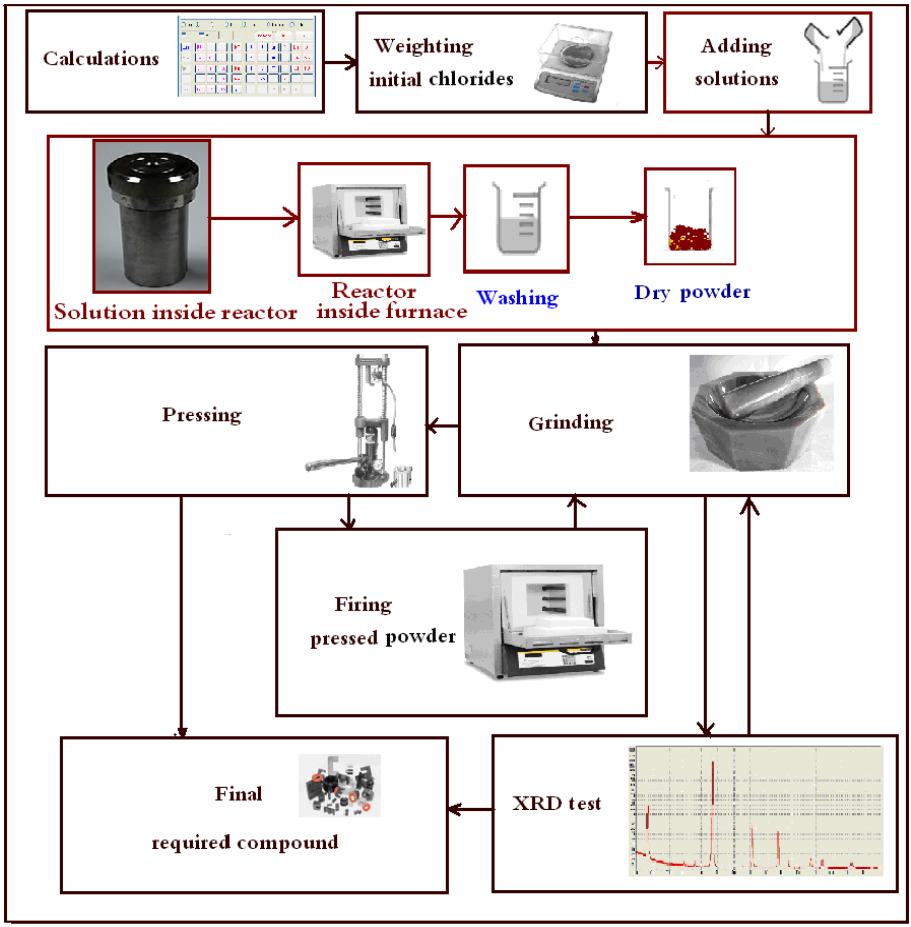

Fig. 2.6 *Schematic representation of the hydrothermal reaction process.*

Return to our example (synthesis $SmMnO_3$) and let us see the difference in the hydrothermal reaction method. For the calculation of how much of initial materials are needed in hydrothermal reaction we can say the same procedure of the co-precipitation method and the same materials could be used. So we can take the same calculations shown in table 2.2 for hydrothermal reaction. According to that calculation, we will repeat "we need to take the following weights of starting precursors; 1.4403g of $SmCl_3.6H_2O$, 0.7813g of $MnCl_2.4H_2O$ and 0.7895g of Na(OH) to obtain 1g of $SmMnO_3$".

The precipitated Powder composed of our $SmMnO_3$ compound and NaCl compound so we need to dissolve NaCl in water and get red of this NaCl which is dissolved in water. This step is so called washing process and we are washing for several times using distilled water until the pH value of the solution became neutral, or until get rid of sodium chloride. Finally, the precipitated powder is dried at 90 ℃ for 3h in air using hot plate. The obtained powder grinded using agate mortar to get well disperse $SmMnO_3$ powder and testing it with X-Ray diffraction. After this step you may need to thermal treatment for this powder to form required $SmMnO_3$ structure. The powder is pressed into a disk-shaped form of 13 mm diameter to be sintered in air for 12 hours at different temperatures 650 ℃, 750 ℃, 850 ℃ and 1000 ℃. The sintered pellets constituted the final sample and has certain shape (disc, rectangular, or torrid) to examine (electrical, magnetic, optical, … etc.) properties of our synthesized material according to certain conditions (either heat treatment or chemical reaction).

2.4 Sol-gel Method

The Sol-gel method is very efficient for producing various functional materials in which particle size, porosity, thin layer thickness, separation of particles of different compositions and structure may be controlled [36-50].

For synthesize rare earth manganites; rare earth acetate hydrate, and manganese (II) acetate tetrahydrate were used as precursors in this method. [37]. For preparing perovskites $R_{1-x}Sr_xMnO_3$ (R= La, Er, Nd, Sm or Yb), [38] an appropriate amount of $La(NO_3)_3\ 6H_2O$, $Er(NO_3)_3\ 6H_2O$ $Nd(NO_3)_3\ 6H_2O$, $Sm(NO_3)_3\ 6H_2O$ or $Yb(NO_3)_3\ 6H_2O$ and $Mn(NO_3)_2\ 6H_2O$ were dissolved in 100 ml H_2O, and then citric acid (the molar ratio of citric acid to nitrate salts is 2:1) was added with continuous stirring at 80 ℃ for 60 minutes. Afterward, 1g of poly (ethylene glycol) was added to mixture with stirring at 80 ℃ for

two hours to get clear solution at pH = 8. The produced sol was aged at 80 ℃ for 24 hours to evaporate water until the gels formed. The produced gel was calcined at 500 ℃ for 2 hours and then annealed at 800 ℃ fo 5 hours to obtain $R_{1-x}Sr_xMnO_3$ (R= La, Er, Nd, Sm or Yb).

So we can say that the proper stoichiometric quantities of the nitrates or chlorides are dissolved in water. This solution was mixed with citric acid solution in 1:1 volume ratio. On heating this mixture in water bath at 80 ℃, a yellowish transparent gel was formed on complete evaporation of water. Continued heating caused the gel to swell and fill the beaker with a foamy precursor. Upon subjecting it to a temperature of 400 ℃ for 2h, the foamy precursor decomposed to give very light, homogenous, black-colored flakes of extremely fine particle size. Further, the powder obtained by crushing these flakes was subjected to final sintering temperature of 800 ℃ for duration of 2h. The powder was magnetically filtered to ensure that there are no traces of carbon in the sample.

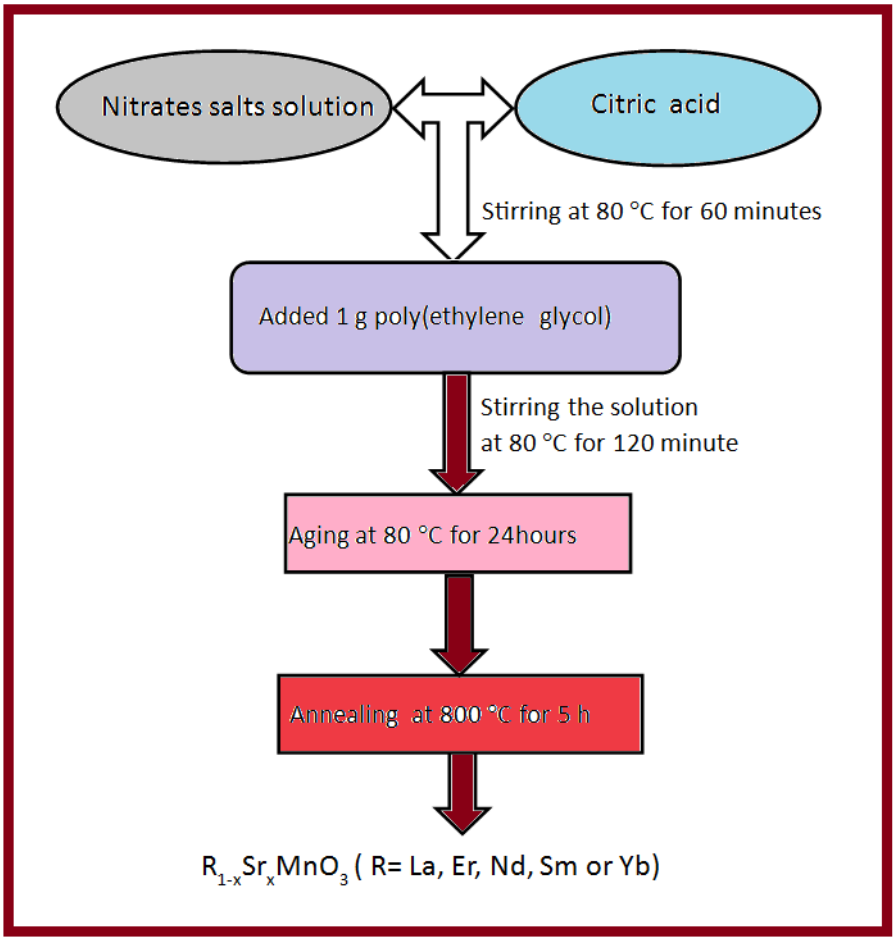

Fig. 2.7 *Schematic representation of the sol gel reaction process.*

Let us see some examples; how we prepared different compounds using different methods. Solid state reaction was used to prepare Samarium [1, 51-52], Europium [53-55] and a part of ytterbium manganites ($Yb_{0.6}Sr_{0.4}MnO_3$, $Yb_{0.6}Sr_{0.}4Mn_{0.98}Fe_{0.02}O_3$ and $Yb_{0.6}Sr_{0.4}Mn_{0.98}{}^{57}Fe_{0.02}O_3$ samples) [56] while chemical reaction was used to prepare nano crystalline size of ytterbium manganites [57-58].

2.5 Samarium Ferrimanganites

Samarium ferrimanganites $SmFe_xMn_{1-x}O_3$ [11, 51] were prepared using solid state method from pure oxides; Sm_2O_3, Fe_2O_3, $^{57}Fe_2O_3$ and Mn_2O_3 with the proper ratio. $^{57}Fe_2O_3$ is used to enable measuring Mossbauer spectra which given in ref. [51]. Strontium is doped to samarium manganite in ref [1] where $Sm_{0.6}Sr_{0.4}MnO_3$ was synthesized from initial pure oxides; Sm_2O_3, Mn_2O_3 and carbonate $SrCO_3$. These oxides and carbonate were mixed together within the appropriate ratios then milled and pressed in disc form. The obtained disc was fired at 950 ℃ for 12h in air. The sample was fired again at 1350 ℃ for 72h, after repetition of milling and pressing process.

2.6 Europium Ferrimanganites

$Eu_{0.65}$ $Sr_{0.35}$ $Mn_{1-x}Fe_xO_3$ were prepared from the initial pure oxides (Eu_2O_3, Fe_2O_3, Mn_2O_3 and SrO) using the solid state reaction method [52-53]. These pure oxides were well mixed with appropriate ratios to be milled together using agate mortar then pressed in disk form under a pressure = 15 ton/cm^2. The pressed disks were fired at 1200 ℃ for 12h in air. The pre-sintered samples were ground again and pressed under the same pressure in the form of disk with 12 mm diameter. All samples were fired again at 1350 ℃ for 72h with an intermediate grinding to ensure homogenization; this heat treatment was followed by natural furnace cooling.

2.7 Ytterbium Manganites

The $Yb_{0.6}Sr_{0.4}MnO_3$, $Yb_{0.6}Sr_{0.}4Mn_{0.98}Fe_{0.02}O_3$ and $Yb_{0.6}Sr_{0.4}Mn_{0.98}{}^{57}Fe_{0.02}O_3$ samples were prepared using standard solid solution method from pure oxides (SrO, Yb_2O_3, Fe_2O_3, $^{57}Fe_2O_3$, and Mn_2O_3) [56]. The purity of the initial oxides was 99.9%. These oxides were carefully mixed, milled and pressed then calcined at a temperature of 1050 ℃ for 25h. After that, obtained compound

milled and pressed again to be burned at a temperature of 1250 ℃ for 12h. Finally the last process was repeated but the firing (sintering) temperature was 1350 ℃ for 40h. The burning was done at the air environment.

Chemical reaction method (co-precipitation method) was used to synthesize $YbMnO_3$ and $Yb_{0.9}Sr_{0.1}MnO_3$ samples from initial pure Chloride solutions; $YbCl_3.6H_2O$, $SrCl_2.6H_2O$, $MnCl_2.4H_2O$ [57]. These Solutions were mixed with NaOH solution within the appropriate molar ratios. The resulting compounds are milled and pressed in the disc form. The obtained discs were fired at 750 ℃, 850 ℃ and 1000 ℃ in air to give $YbMnO_3$ and $Yb_{0.9}Sr_{0.1}MnO_3$.

3

Elemental Analysis and Microstructure of 3d-4f Oxides

Elemental analysis is very important step that enable us to test our compound if it is formed in the proper way or we have strange elements in our compound. Elemental analysis and microstructure micrographs were performed for both ytterbium [56-57] and europium [54] managnites. The details of these studies will be presented in the following sections.

3.1 Ytterbium Manganites

The elemental analysis using EDXS was carried out for europium and ytterbium manganites in order to test the elements which constitute the proposed compounds. The used accelerating voltage was 25KeV within resolution of 128 eV of EDXS spectra for both $Yb_{0.6}Sr_{0.4}MnO_3$ and $Yb_{0.6}Sr_{0.4}Mn_xFe_{1-x}O_3$. The following standards; K quartz, K Mn, L SrF_2 and YbF_3 were used for identifying the elements that constitute $Yb_{0.6}Sr_{0.4}MnO_3$ (Oxygen, manganese, Strontium and Ytterbium). The obtained peaks correspond to Oxygen, Manganese, Strontium and Ytterbium which form the $Yb_{0.6}Sr_{0.4}MnO_3$ are noted [16]. From analysis of the measured spectra it is found that ytterbium, strontium, manganese and oxygen are the elements which form $Yb_{0.6}Sr_{0.4}Mn_xFe_{1-x}O_3$ where X=1 while ytterbium, strontium, manganese, iron and oxygen are observed for X=0.98 with the proper concentration. The concentration of each element in the compound is in agreement with the theoretically calculated concentrations (see table 3.1). For identification of the elements constituting the $Yb_{0.6}Sr_{0.4}Mn_{0.98}Fe_{0.02}O_3$ composite the same standards for identifying the $Yb_{0.6}Sr_{0.4}MnO_3$ were used in addition to *K*Fe for identifying iron. It is quite clear that the experimentally observed percentages of elements (which constitute the proposed composites) are in agreement with those calculated.

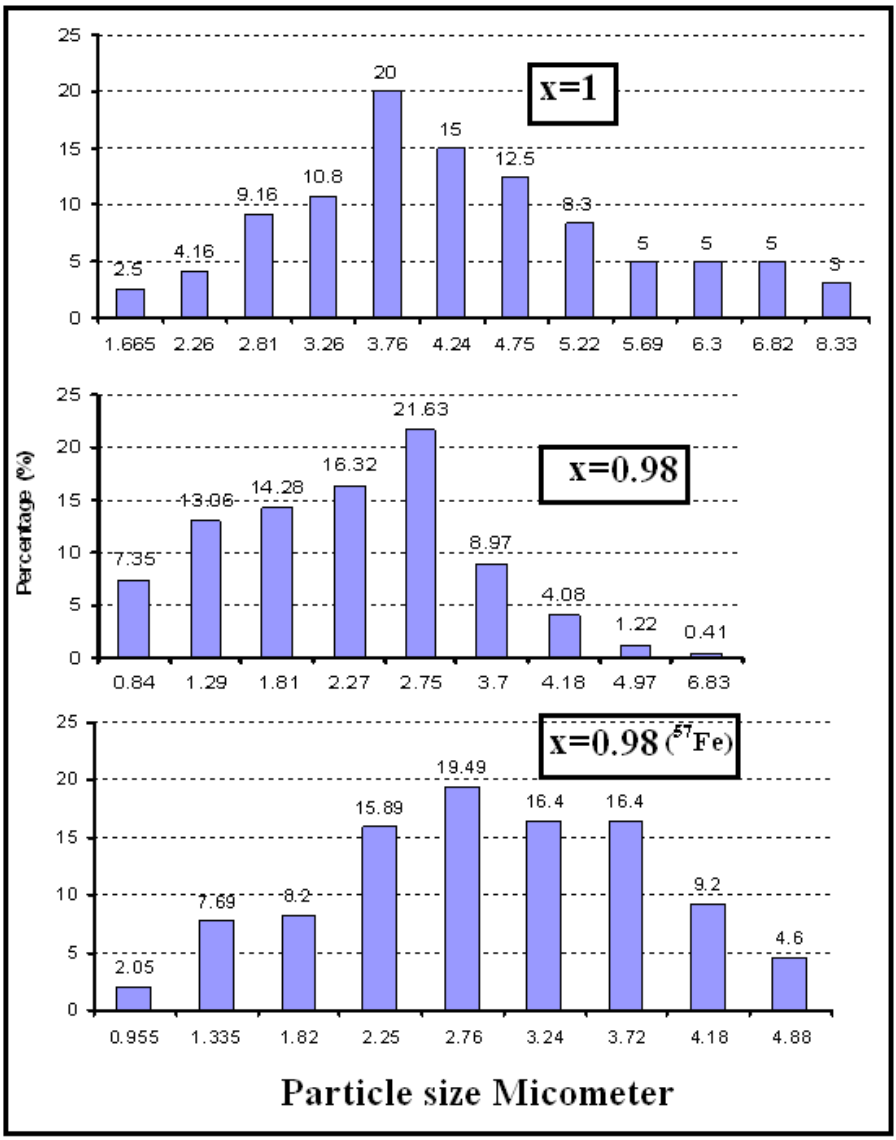

Fig. 3.1 *The particle size distribution of* $Yb_{0.6}Sr_{0.4}Mn_xFe_{1-x}O_3$.

The elemental analysis reveals that the synthesized composites of the proposed structure are in proper stoichometry. Particle size distribution of $Yb_{0.6}Sr_{0..4}MnO_3$, $Yb_{0.6}Sr_{0.4}Mn_{0.98}{}^{57}Fe_{0.02}O_3$ and $Yb_{0.6}Sr_{0.4}Mn_{0.98}Fe_{0.02}O_3$ was done.

The obtained micrographs were analyzed according to digital imaging processing method. The particle size distribution of the $Yb_{0.6}Sr_{0.4}Mn_xFe_{1-x}O_3$ is illustrated in Fig. 3.1. It is quite clear that the minimum observed size of the composite where x=1 is of 1.665 μm. Those particles represent 2.5%. The maximum particle size was 8.33 μm which is 3%. The maximum percentage is 20% for 3.76 μm. In the case of x=0.98 (for ^{57}Fe) it is noted that 2.05% of minimum size of 0.955 μm while 4.6% of maximum size of 4.88 μm. 2.76 μm particle size is the peak of this distribution within 19.49%. The minimum size of 0.84 μm represents 7.35% while 4.6% the maximum size of 6.83 μm represents 0.41% and 2.756 μm is the peak of this distribution within 21.63%. One can note that the particle size of both $Yb_{0.6}Sr_{0.4}Mn_{0.98}{}^{57}Fe_{0.02}O_3$ and $Yb_{0.6}Sr_{0.4}Mn_{0.98}Fe_{0.02}O_3$ is identical and the difference in particle size is obtained in the sample x=1.

The elemental analysis using EDXS was carried out for $Yb_{0.9}Sr_{0.1}MnO_3$ and $YbMnO_3$ as shown in Fig. 3.2 and Fig. 3.3. The used accelerating voltage was 15KeV. The following standards; quartz, Mn, SrF_2 and YbF_3 were used for identifying the elements that constitute $Yb_{0.9}Sr_{0.1}MnO_3$ (Oxygen, manganese, Strontium and Ytterbium). The obtained peaks correspond to Oxygen, manganese, Strontium and Ytterbium which form the $Yb_{0.9}Sr_{0.1}MnO_3$ are illustrated in Fig. 3.2 On the other hand the obtained peaks correspond to Oxygen, manganese and Ytterbium which form the $YbMnO_3$ are illustrated in Fig. 3.3. The concentrations of each element in both compounds theoretically calculated and experimental are listed in table 3.1.

Table 3.1 *Elements identifications of* $Yb_{0.6}Sr_{0.4}Mn_xFe_{1-x}O_3$.

X	Element	Exp. Percentage, %	Cal. Percentage, %
	Yb	41.84 (18)	42.93
	Sr	14.04 (11)	14.49
1.00	Mn	25.05 (11)	22.72
	Fe	00.00	00.00
	O	19.07 (16)	19.85
	Yb	46.00 (19)	42.92
	Sr	11.97 (11)	14.49
0.98	Mn	24.21 (12)	22.72
	Fe	00.19 (60)	00.46
	O	19.85 (19)	19.85

It is quite clear that the experimentally observed percentages of elements are in a good agreement with those calculated. So one can say that, the elemental analysis reveals that the synthesized composites of the proposed structure are in the proper stoichiometry. The microstructure graphs $Yb_{0.9}Sr_{0.1}MnO_3$ and $YbMnO_3$ are taken using Field Emission Scanning Electron Microscope FE-SEM – JEOL (JSM-5600) at 15KeV and magnification X - 43000, see Fig. 3.4 and Fig. 3.5. From Fig. 3.6, it is clear that the particle size of $Yb_{0.9}Sr_{0.1}MnO_3$ composite fired at 850 ℃ at 12h are on the range of 80 nm. One can say there is homogeneity in the size of particles all over the graph.

Looking at the microstructure of $YbMnO_3$ one can note that the composite which fired at 750 ℃ has nano tube structure of size 60 nm. In the same composite but fired at 1000 ℃ the particles aggregated and the particle size increased (110 nm).

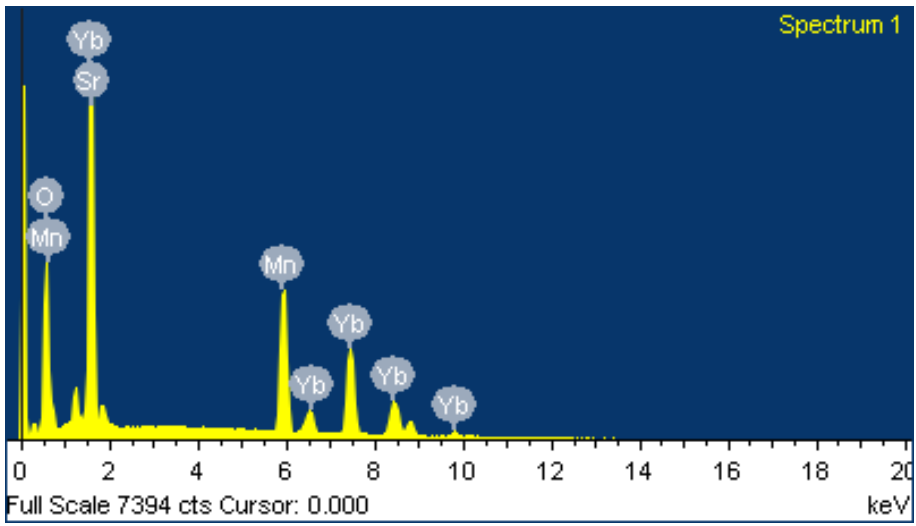

Fig. 3.2 *EDX spectra of* $Yb_{0.9}Sr_{0.1}MnO_3$.

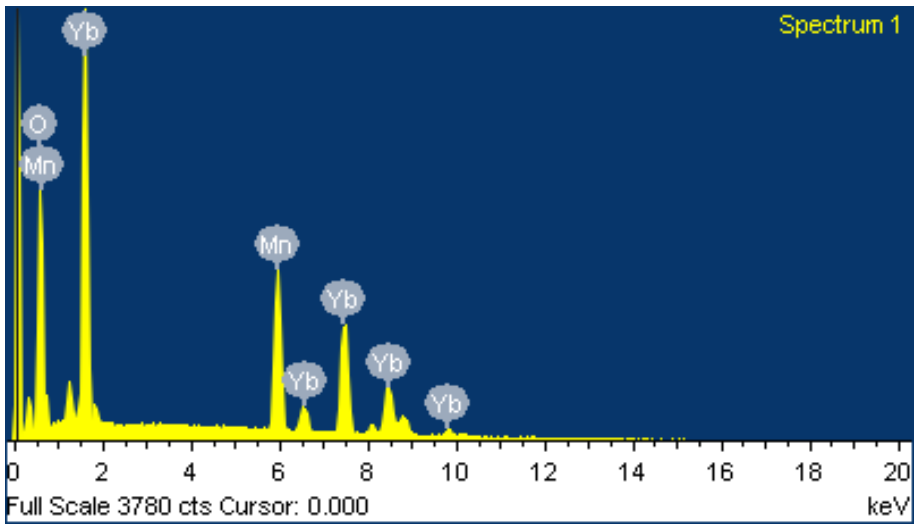

Fig. 3.3 *EDX spectra of* $YbMnO_3$.

Table 3.2 *Element identification of* $Yb_xSr_{1-x}MnO_3$.

X	Element	Exp. Percentage, %	Cal. Percentage, %
0.9	Yb	55.27	58.23
	Sr	2.19	3.28
	Mn	19.10	20.54
	O	23.44	17.95
1	Yb	56.70	62.70
	Mn	16.98	19.91
	O	26.31	17.39

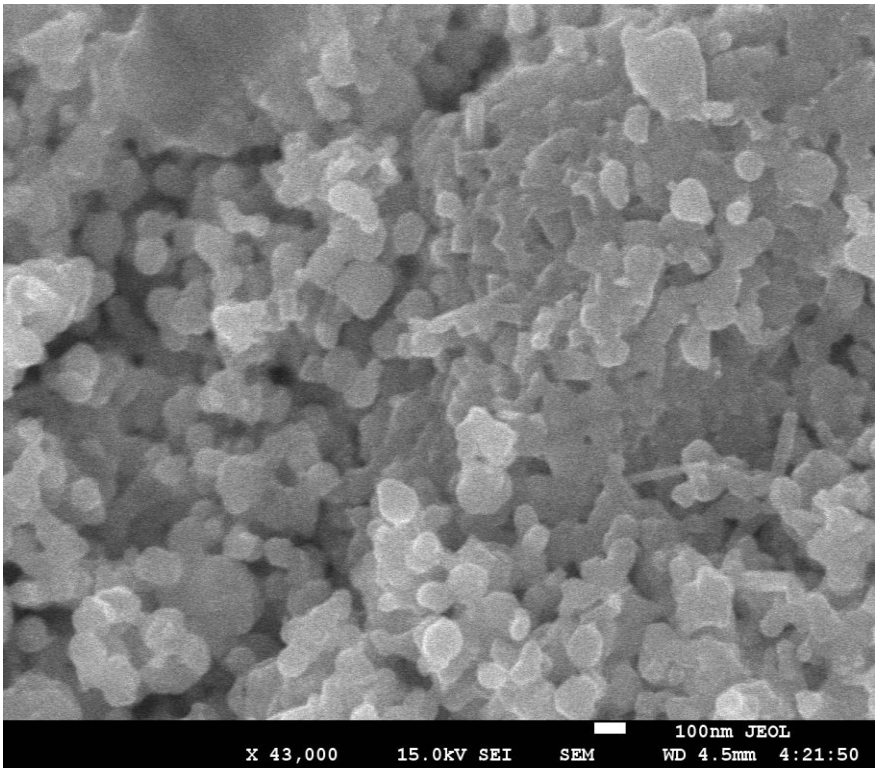

Fig. 3.4 *Microstructure of the* $Yb_{0.9}Sr_{0.1}MnO_3$ *composite.*

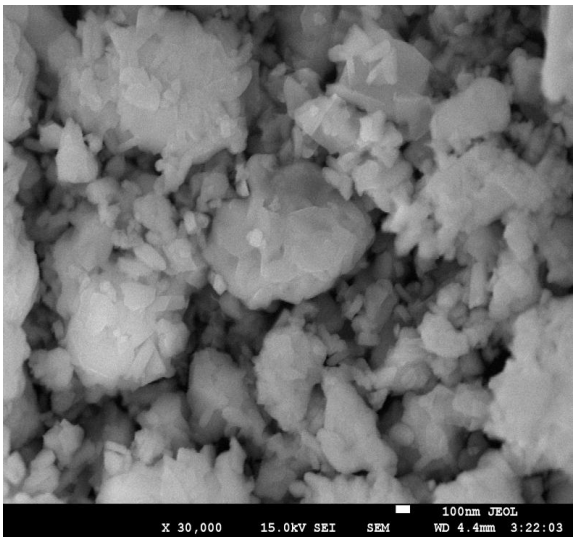

(a)

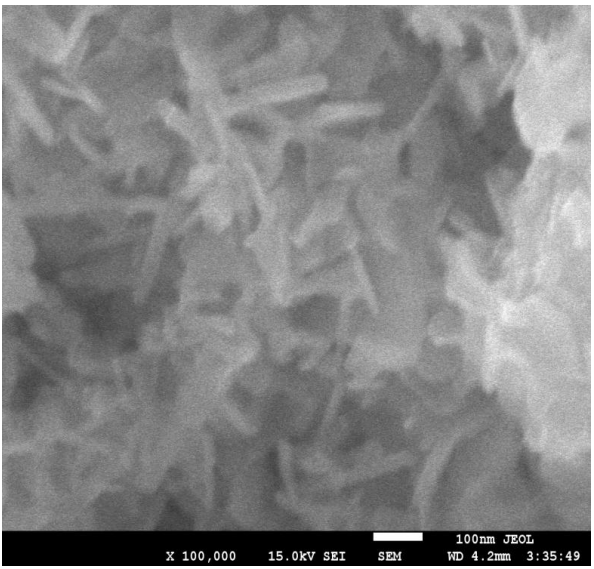

(b)

Fig. 3.5 *Microstructure of the $YbMnO_3$ composite; (a) fired at 1000 ℃ and (b) fired at 750 ℃.*

The particle size of the composite as prepared is closed to 50 nm. Recently reported by Rößler et. al [58] that the morphology of thin films has a strong influence on the local conductivities in manganite thin films. The magnetic properties of manganites also depend on the morphology of these manganites. It was reported by Marttinez et. al. [59], that the magnetoresistance and the magnetization of ceramic $La_{2/3}A_{1/3}MnO_3$ (A = Sr, Ca) oxides have been studied as a function of the grain size. It was found that [2] these ceramics become magnetically harder when reducing the particle size exhibiting a large magnetic anisotropy that increases when reducing the grain size.

3.2 Europium Manganites

The elemental analysis using EDXS was carried out for $Eu_{0.65}Sr_{0.35}Mn_{1-x}Fe_xO_3$ (x=0.1 and 0.5) samples [54]. The following standards; SiO_2, Mn, Fe, SrF and EuF were used for identifying Oxygen O, manganese Mn, Iron Fe, Strontium Sr and Europium Eu elements respectively that constitute $Eu_{0.65}Sr_{0.35}Mn_{1-x}Fe_xO_3$. The obtained peaks correspond to Oxygen, Manganese, Iron, Strontium and Europium which forms the $Eu_{0.65}$ $Sr_{0.35}$ $Mn_{1-x}Fe_xO_3$ that is good indication for the absence of impurities in synthesized compounds (see table 3.3). This means the quality of synthesis.

Table 3.3 *Elements identifications of* $Eu_{0.65}Sr_{0.35}Mn_{1-x}Fe_xO_3$.

X	**0.1**		**0.5**	
Element	**Exp. Weight %**	**Cal. Weight %**	**Exp. Weight %**	**Cal. Weight %**
O	18.67	20.65	28.49	20.62
Mn	21.05	21.27	10.41	11.80
Fe	3.56	2.40	11.26	11.99
Sr	7.05	13.19	11.38	13.17
Eu	49.67	42.49	38.46	42.43
Totals	100.0	100.0	100.0	100.0

The concentration of each element in the compound are in good agreement with the theoretically calculated, see table 3.3. As it is quite clear that the experimentally observed percentages of elements (which constitute the proposed composites) are in good agreement with those calculated. The elemental analysis reveals that the synthesized composites of the proposed structure are in proper stoichiometry and this is in a good agreement with the crystal structure analysis using X-ray diffraction which reported in ref., [53]. The microstructure graphs $Eu_{0.65}Sr_{0.35}Mn_{1-x}Fe_xO_3$ are taken at 15KeV and magnification X-43000, see Fig. 3.2. From Fig. 3.2, it is clear that the grain size of in the composite where x=0.1 is on the range of 2.5 – 3.5 μm. One can say that the homogeneity size of grains is not completely represented. Looking at the microstructure of composite where x=0.5 one can note that the lower grain size is quite clear compared with the grain size in x=0.1. The grain size in the case of x=0.5 in the range 0.5 – 1 μm.

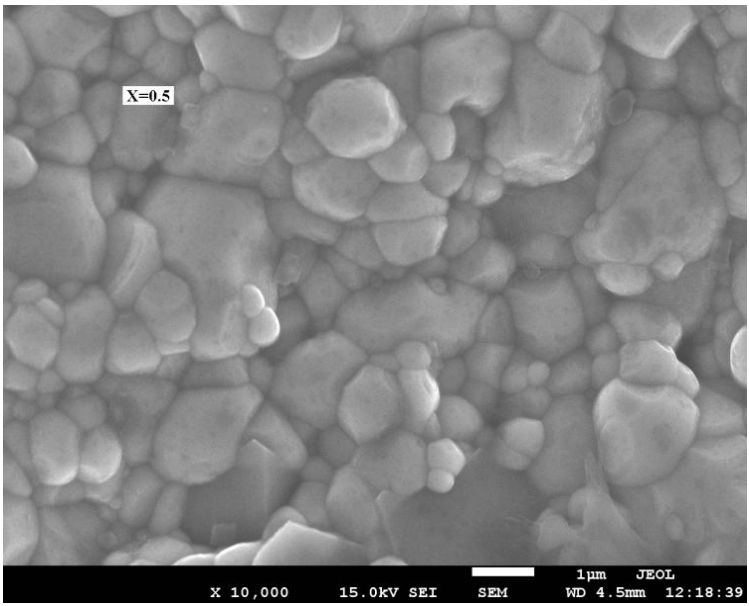

X=0.5

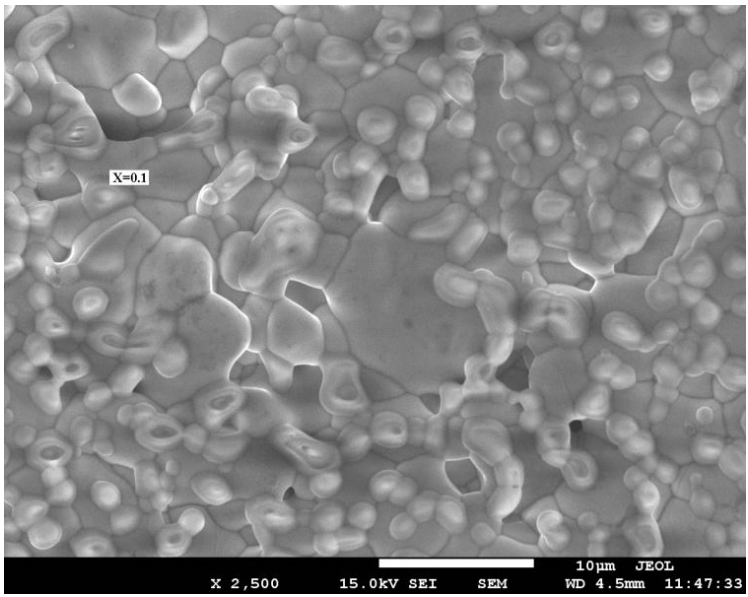

X=0.1

Fig. 3.6 *Micrographs of $Eu_{0.65}Sr_{0.35}Mn_{1-x}Fe_xO_3$ (X= 0.1 and 0.5) measured at 15 kV.*

3.3 Neodymium Manganites

The elemental analysis using EDXS was carried out for one sample $Nd_{0.6}Sr_{0.4}Mn_{0.7}Co_{0.3}O_3$ as shown in fig. 3.7. The used accelerating voltage was 15KeV. Looking at table 3.4, it is quite clear that the experimentally observed percentages of elements are in a good agreement with those theoretically calculated. So, one can say that the elemental analysis reveals that the synthesized composites of the proposed structure ($Nd_{0.6}Sr_{0.4}Mn_{0.7}Co_{0.3}O_3$) are in the proper stoichiometry.

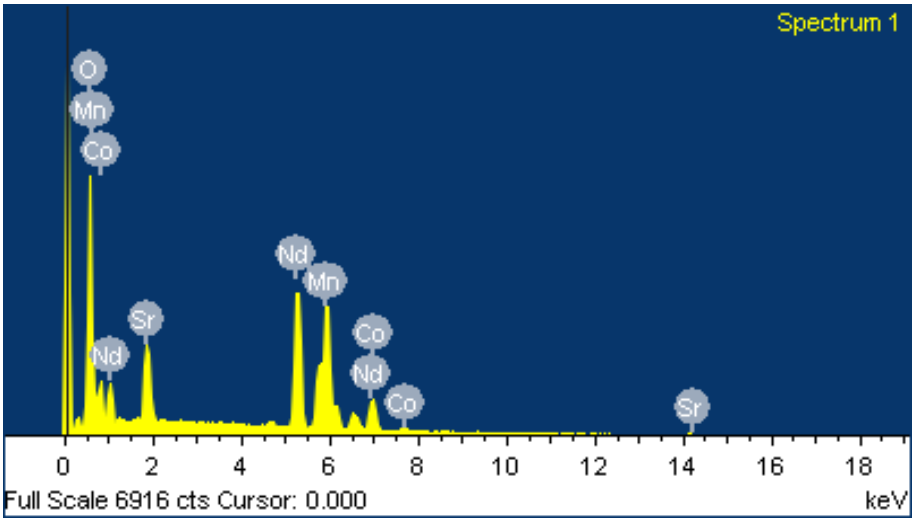

Fig. 3.7 *EDX spectra of* $Nd_{0.6}Sr_{0.4}Mn_{0.7}Co_{0.3}O_3$.

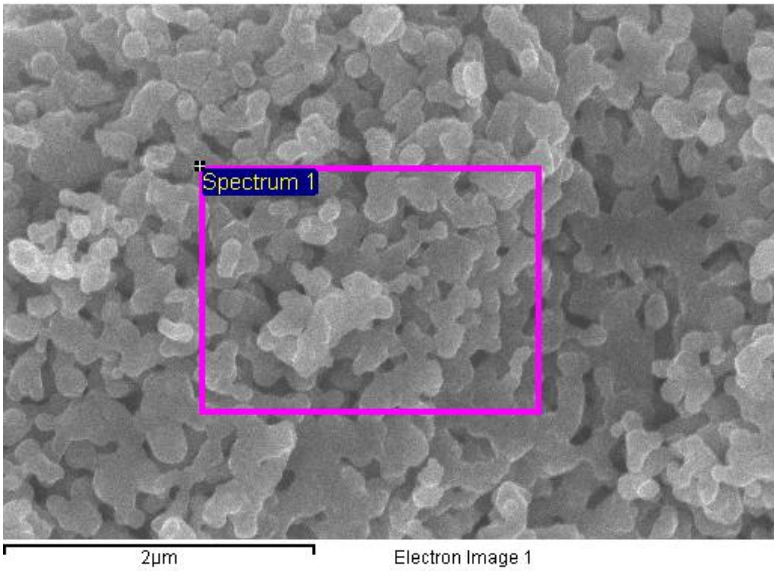

Fig. 3.8 *Micrograph of* $Nd_{0.6}Sr_{0.4}Mn_{0.7}Co_{0.3}O_3$ *annealed at 850 ℃ for 12h.*

Table 3.4 *Element identification of* $Nd_{0.6}Sr_{0.4}Mn_{0.7}Co_{0.3}O_3$.

Element	Exp. Percentage, %	Cal. Percentage, %
Nd	38.81	38.34
Sr	10.25	15.53
Mn	16.42	17.04
Co	6.00	7.83
O	28.50	21.26

The microstructure graphs $Nd_{0.6}Sr_{0.4}Mn_{0.7}Co_{0.3}O_3$ are illustrated in Fig. 3.8. It is quite clear that say there is homogeneity in the size of particles all over the graph. The minimum particle size is 119.05 nm while the maximum particle size is 190.48 nm. The mean value of the particle size is 150.80 nm which in good agreement with the crystalline size deduced from XRD measurements (147.4 nm).

4

Crystal Structure of 3d-4f Oxides

3d-4f has the perovskite -like structure, where a perovskite is any material with the same type of crystal structure as calcium titanium oxide ($CaTiO_3$, known as the *perovskite structure*. Perovskites take their name from this compound, which was first discovered in the Ural mountains of Russia by Gustav Rose in 1839 and is named after Russian mineralogist, L. A. Perovski (1792-1856). The general chemical formula for perovskite compounds is ABX_3, where 'A' and 'B' are two cations of very different sizes, and X is an anion that bonds to both. The 'A' atoms are larger than the 'B' atoms.

The correlation between the electronic and magnetic transport and the crystal structure is very important topics. Study crystal structure will help us to understand very interesting physical phenomena represented by these materials. Crystal structure in the present review has been studied using different technique; X-ray diffraction, neutron diffraction and Raman scattering.

4.1 X-ray Diffraction

Crystal structure of europium manganites was investigated using X-ray diffraction and reported in ref [13]. A distorted orthorhombic crystal structure is noted in europium manganites. It was found that the $Eu_{0.65}$ $Sr_{0.35}$ $Mn_{1-x}Fe_xO_3$ samples with x = 0.1, 0.5 and 0.7 consist of one phase single perovskite of orthorhombic system that matched with the ICDD card No. (82-1474). The X-ray diffraction patterns of all samples were refined using Rietveld method to calculate the accurate unit cell dimensions, using the space group P_{bnm}, Z = 4 with A site cations (Sr/Eu) situated at Wyckoff position 4c (x, y, 1/4), B-site cations (M = transition metal cations Mn and/or Fe) situated at Wyckoff position 4b (0.5, 0, 0) and two oxygen atoms O1 and O2 situated at 4c and 4d Wyckoff positions, respectively. A full profile analysis included a refinement of background, scaling factor, lattice parameters, Brag peak profile, positional and thermal parameters were done. The overall good agreement between the

calculated and observed patterns for $Eu_{0.65}Sr_{0.35}Mn_{1-x}Fe_xO_3$, x = 0.1, 0.5 and 0.7 is illustrated in Fig. 4.1. The agreement factors show that the refinement procedures are acceptable for all samples. All the crystallographic data obtained after the refinement of the structure of the investigated samples are summarized and reported in ref. [13]. It is obviously that the volume of unit cell is increased with increasing the iron contents. This small increase seems to be due to the difference between the ionic radii of iron (Fe^{+3} = 0.55Å) and manganese (Mn^{+4} = 0.53 Å). The mean bond length of M – O increases linearly with increasing the iron content x in the $Eu_{0.65}Sr_{0.35}Fe_x\ Mn_{1-x}O_3$ samples. This increase in bond length may explain the increase in the resistivity of the $Nd_{0.65}Sr_{0.35}Fe_xMn_{1-x}O_3$ with the increase in the iron content as reported by Abdel-Latif *et al.* [3]. The octahedral tilt of the perovskite structure has a significant meaning, which describes the charge and magnetic transfer.

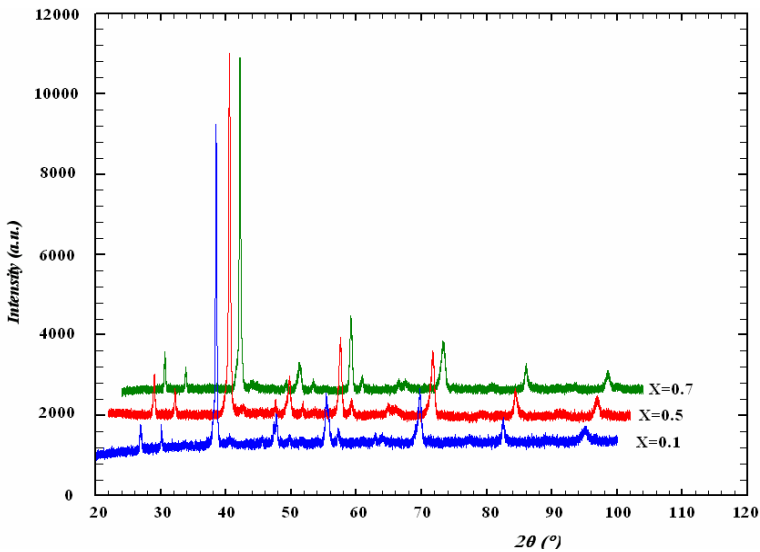

Fig. 4.1 *XRD patterns of the $Eu_{0.65}Sr_{0.35}Fe_x\ Mn_{1-x}O_3$ composite.*

The results of XRD analysis of $Sm_{0.6}Sr_{0.4}MnO_3$ showed that it has an orthorhombic crystal structure of space group *Pnma*. The quality factors of the

acceptable range. The Sm/Sr atoms have (x, 1/4, z) coordinates while the Mn atoms have (0, 0, 1/2) coordinates. Concerning the oxygen atoms; four of them occupy the (x, 1/4, z) coordinates and eight have (x, y, z) coordinates. The x and z of Sm/Sr atoms have the values; 0.0170 and 0.0214 while their values for O (1) atoms are 0.5290 and 0.0310, respectively. The lattice parameters and Mn–O bond lengths of $Sm_{0.6}Sr_{0.4}MnO_3$ in the work presented in ref [20] are compared with those for $Sm_{0.6}Sr_{0.4}MnO_3$ that is prepared in different lab using the same solid state reaction but with different conditions. It is clear that, there is a good agreement between the lattice constants in both samples however, a difference was found only in the bond length of Mn–O. This deviation in the result of the bond length can be attributed to the different values of the octahedral tilting (MnO_6). The tilt of MnO_6 is calculated according to the well-known formula given in Ref. [1]. The tilt angles of the sample under-investigation are [b] tilt ~ 6.8755◦ and [c] tilt ~ 1.05725◦ and they have small values compared with those calculated for $Sm_{0.6}Sr_{0.4}MnO_3$ prepared with different conditions and reported in Ref. [20] namely; [b] tilt ~ 10.65◦ [c] tilt ~ 10◦. This is an indication that in our sample there is less distortion on the MO_6 octahedron than that in the sample. The crystal structure research, here, is one of the most important subjects because of the strong correlation between this crystal structure and electromagnetic transport phenomena as we will see latter.

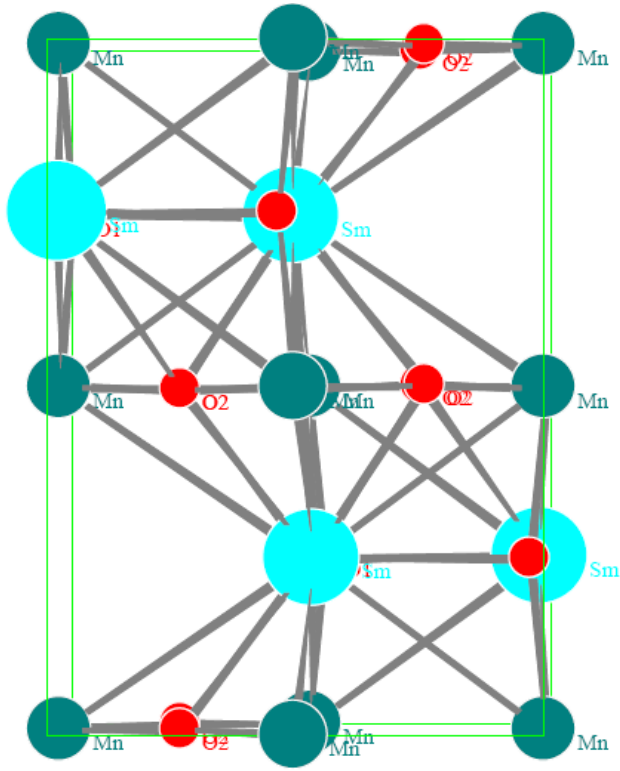

Fig. 4.2 *Crystal structure of $SmSrMnO_3$.*

X-ray diffraction pattern of $Nd_{0.6}Sr_{0.4}Mn_xCo_{1-x}O_3$ composites (x=0 and x=1) which annealed at 850 ℃ for 12h and (x=0.3 and 0.7) annealed at 750 ℃ for, measured at room temperature, is shown in Fig. 4.3. It is quite clear that all reflections are corresponding to the orthorhombic crystal system of space group *Pnma* (No 62). All the reflections which belong to the orthorhombic crystal system of P_{nma} space group for $Nd_{0.6}Sr_{0.4}Mn_xCo_{1-x}O_3$ where x=0.3, and 0.7 are represented in Fig. 4.4. The maximum refection intensity at 121 planes is observed as illustrated in Fig. 4.4. The lattice parameters of this composites resulting from fitting of the experimental XRD pattern using Fullprof program [67] are listed in table 4.1. The crystalline parameters are calculated using the well known Scherrer formula;

$$\text{Crystalline size} = k\lambda/(B \sin\theta)$$

where B is FWHM and equal to $B_{obs.} - B_{std.}$ ($B_{obs.}$ is FWHM of observed sample and B_{std} is FWHM of standard sample).

One can note that the good agreement between the particle sizes deduced from the SEM micrograph and the XRD diffraction.

Table 4.1 *Lattice parameters and volume of unit cell of* $Nd_{0.6}Sr_{0.4}Mn_xCo_{1-x}O_3$.

x	a Å	b Å	c Å	V $Å^3$	Crystalline Size (nm)
0.0	5.227	7.5388	5.4058	213.046	74.8
0.3	5.4479	7.6708	5.4080	225.999	113.5
0.7	5.4417	7.7124	5.4400	228.309	147.4
1.0	5.4285	7.6850	5.4847	228.811	34.2

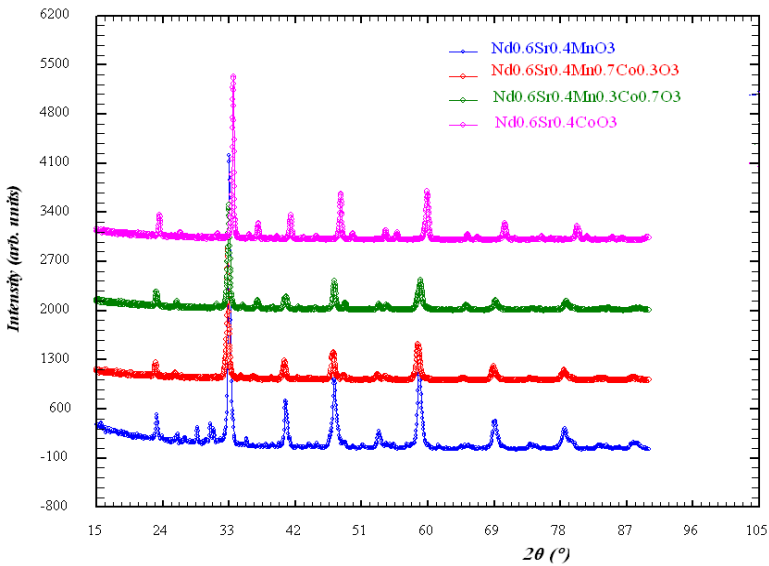

Fig. 4.3 *XRD pattern of* $Nd_{0.6}Sr_{0.4}Mn_xCo_{1-x}O_3$ *(x=0 and x=1) annealed at 850 ℃ for 12h and (x=0.3 and 0.7) annealed at 750 ℃ for 12h.*

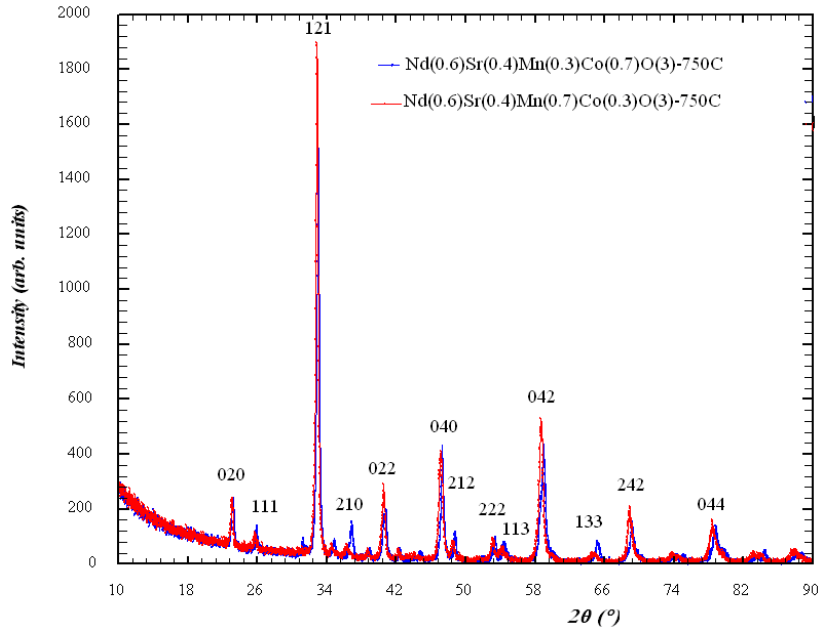

Fig. 4.4 *XRD patterns of $Nd_{0.6}Sr_{0.4}Mn_xCo_{1-x}O_3$ where x=0.3, and 0.7 annealed at 750 ℃ for 12h.*

All XRD patterns of different concentrations of iron in $Nd_{0.65}Sr_{0.35}Fe_xMn_{1-x}O_3$ compounds, measured at room temperature, are displayed in Fig. 4.4. Looking at the observed reflections of the measured XRD it is found that they are corresponding to orthorhombic crystal system.

The refined crystal structure of $Nd_{0.65}Sr_{0.35}Fe_xMn_{1-x}O_3$ phases were deduced by powder X-ray Rietveld analysis. One can say that all compounds crystallize in the orthorhombic structure of space group P*nma* (no. 62). The lattice parameters of $Nd_{0.65}Sr_{0.35}Fe_xMn_{1-x}O_3$ are summarized in Table 4.2. The increase of Iron concentration may lead to decrease in the volume of unit cell. The lattice constants and volume of unit cell for the compounds where x=0.3 and x=0.6 are closed. The lattice parameters of calculated for $Nd_{0.65}Sr_{0.35}Fe_{0.6}Mn_{0.4}O_3$ sample

from XRD are in a good agreement with those calculated by Abdel-Latif et al [24] from neutron diffraction.

Table 4.2 *The lattice parameters of* $Nd_{0.65}Sr_{0.35}Fe_xMn_{1-x}O_3$.

x	*a*, Å	*b*, Å	*c*, Å	V, Å^3
0.1	5.4636	7.7424	5.4662	231.2278
0.3	5.4555	7.7264	5.4595	230.1254
0.6	5.4638	7.7322	5.4595	230.6486

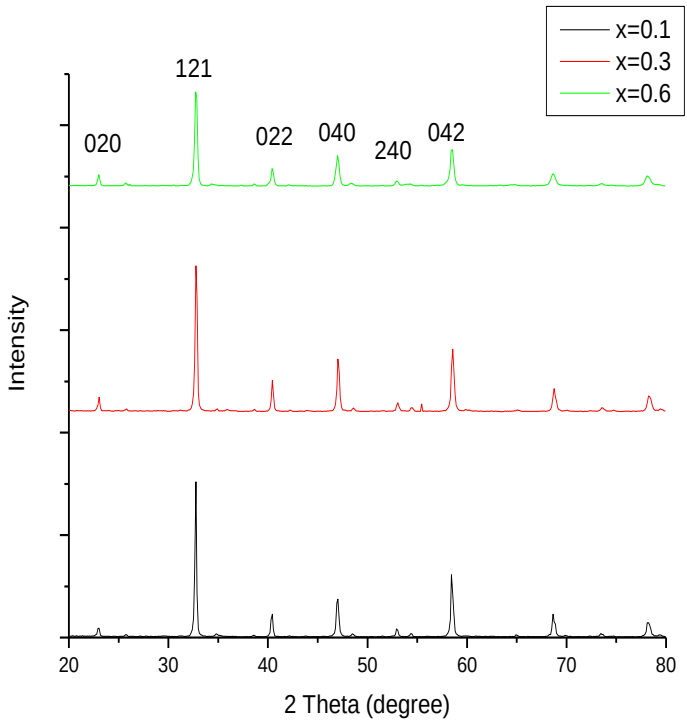

Fig. 4.5 *XRD patterns of different concentrations of iron in* $Nd_{0.65}Sr_{0.35}Fe_xMn_{1-x}O_3$.

Hexagonal crystal structure was observed for ytterbium manganites [17, 21]. X-ray diffraction pattern of the $YbMnO_3$ composite [17] is shown in Fig. 4.6. The XRD of $YbMnO_3$ at different firing temperatures 750 ℃ and 1000 ℃

spectra are refined according to space group $P6_3cm$ where the Yb/Sr atoms occupy two positions *2a* and *4b*. Yb1/Sr1 has (0, 0, 0.2754) and (1/3, 2/3, 0.2274) coordinates while Mn atoms are in 6*c* (0.3518, 0, 0) [22-23]. The fitted lattice parameters of hexagonal crystal system are in a good agreement with those reported by H. A. Salama et al., [24], van Aken et al., [68] Zhoi et al., [69] and Katsufuji et al., [70].

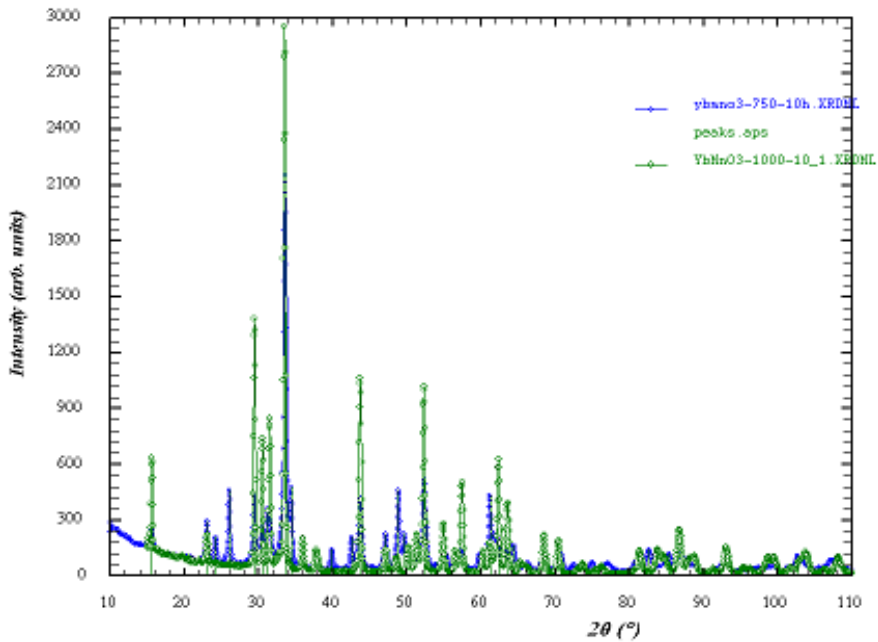

Fig. 4.6 *XRD patterns of the $YbMnO_3$ composite; fired at 1000℃ and at 750℃. The orthorhombic system is refined according to space group Pnma where the Yb/Sr atoms have (x, 1/4, z) coordinates and the Mn atom has (0, 0, ½) coordinates. Concerning the oxygen atoms; four of them occupy the (x, 1/4, z) coordinates and eight have (x, y, z) coordinates. On the other hand the hexagonal system is refined according to space group $P6_3c$. [17].*

The effect of strontium doping on crystal structure is showed in the present review where the diffraction pattern of $Yb_{0.9}Sr_{0.1}MnO_3$ showed that this compound has mixed crystal structure phases (hexagonal and orthorhombic) [17].

4.2 Neutron Diffraction

Neutron diffraction measurements for $Yb_{0.6}Sr_{0.4}MnO_3$ and $Yb_{0.9}Sr_{0.1}MnO_3$ in the temperature range from 2.5K up to room temperature are shown in Fig. 4.7 (a-b). It is noted from the lattice parameters of $Yb_{0.6}Sr_{0.4}MnO_3$ that the volume of unit cell of both hexagonal and orthorhombic depends on the temperature where it increase with decreasing temperature see Fig. 4.7. Neutron diffraction patterns were refined using Fullprof software [76] which based on Rietveld method. According to refinement of neutron diffraction patterns of $Yb_{0.6}Sr_{0.4}MnO_3$ it is found that the crystal structure of $Yb_{0.6}Sr_{0.4}MnO_3$ is possessing mixed orthorhombic/hexagonal phase with space group P*nma* (62) for orthorhombic phase while a space group $P6_3cm$ (185) for hexagonal phase. It is noted from the lattice parameters that the volume of unit cell of both hexagonal and orthorhombic depends on the temperature; increase with decreasing temperature. From the analysis of neutron diffraction patterns of $Yb_{0.9}Sr_{0.1}MnO_3$ it has mixed orthorhombic/hexagonal phase with space group P*nma* (62) for orthorhombic phase while a space group $P6_3cm$ (185) for hexagonal phase as well as in the case of $Yb_{0.6}Sr_{0.4}MnO_3$.

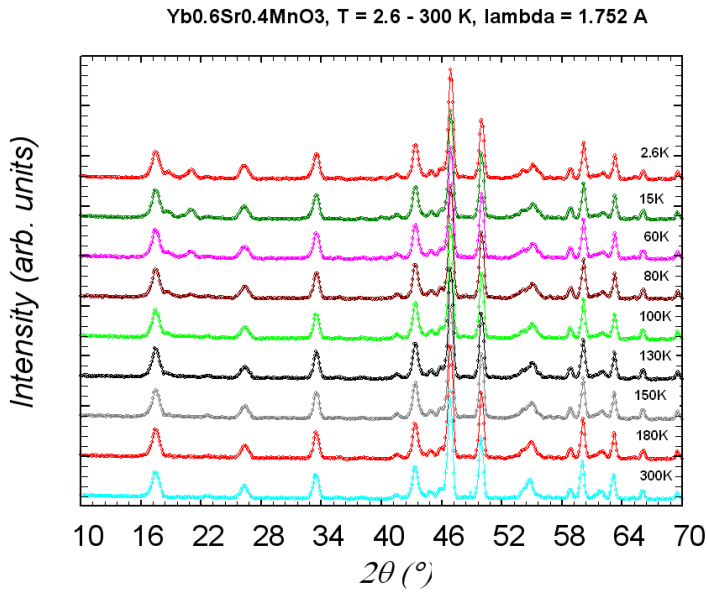

$Yb_{0.9}Sr_{0.1}MnO_3$; T=2.5 – 300K, Lambda =1.752 Å

Fig. 4.7 *The neutron diffraction patterns of $Yb_{0.6}Sr_{0.4}MnO_3$ at different temperatures.*

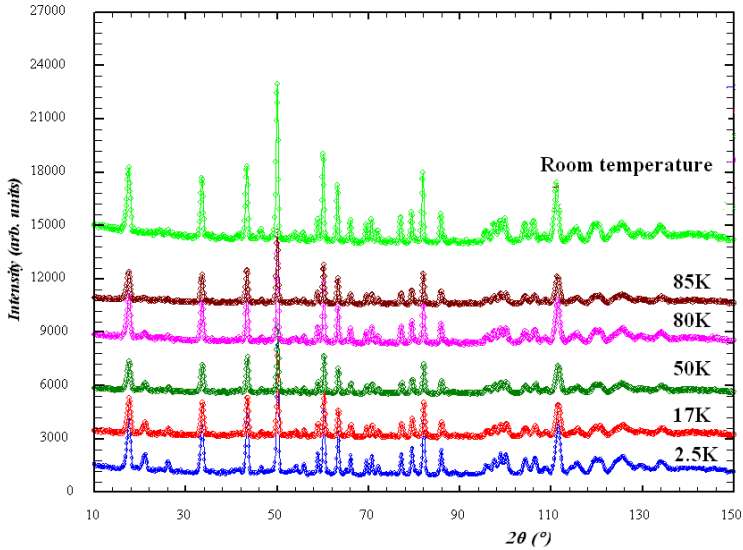

Fig. 4.8 *The neutron diffraction patterns of $Yb_{0.9}Sr_{0.1}MnO_3$ at different temperatures.*

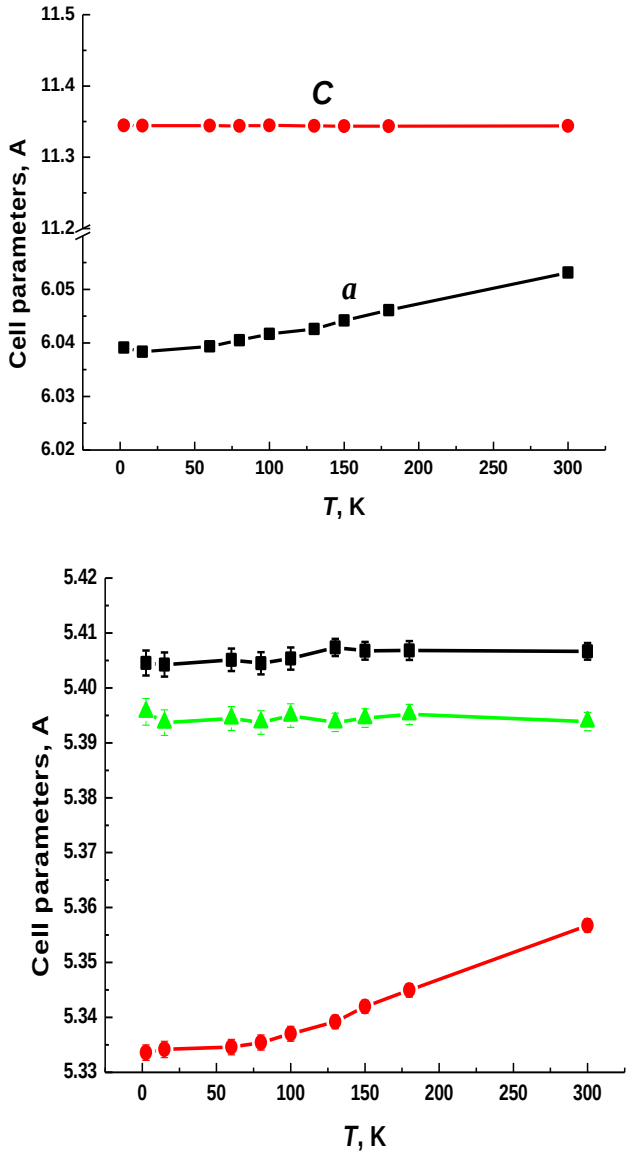

Fig. 4.9 *Lattice parameters of $Yb_{0.6}Sr_{0.4}MnO_3$ of both hexagonal and orthorhombic phases as a function of temperature.*

The neutron diffraction patterns of the $NdFe_{0.6}Mn_{0.4}O_3$ at different temperatures (114 K and 287 K) are showed in Fig. 4.10. The analysis of the magnetic structure, of these diffraction patterns, shows that this compound has non-collinear ordering (weak ferromagnetic ordering) at 114 K. temperature.

The component of magnetic moment at x-, y- and z-axis and the resulting magnetic moment are given in table 4.3. It is clear that the components of magnetic moment in y and z axis are constant with increasing the temperature while the increase only in x-axis. The X-ray diffraction analysis as well as the neutron diffraction and Mössbauer spectroscopy [7] analysis approved the formation of a single phase structure of the samples. The experimentally obtained density of such samples compared with those defined by X-ray is in the range of 88-90%, thus the porosity is of the range 10-12%, (in the acceptable range). The lattice parameters of all samples are given in Table 4.3 and the neutron diffraction pattern of $Nd_{0.65}Sr_{0.35}Mn_{0.4}Fe_{0.6}O_3$ is shown in Fig. 4.7. All spectra are refined according to space group Pnma where the Nd/Sr atoms have (x, 1/4, z) coordinates and the Fe/Mn atoms have (0, 0, ½) coordinates. Concerning the oxygen atoms; four of them occupy the (x, 1/4, z) coordinates and eight have (x, y, z) coordinates. The x and z of Nd/Sr atoms have values from 0.024 and0.002 to 0.071 and 0.033, respectively while their values for O(1) atoms vary from 0.495 and 0.001 to 0.642 and 0.042, respectively. The O(2) atoms coordinates x, y and z are in the range from -0.251, 0.001, 0.221 to -0.345, 0.033, 0.353, respectively. The refined thermal parameters, obtained from the analysis of X-ray diffraction patterns, are anisotropic for all x, see Table 4.3. The quality factors of the refinements are in the range of acceptable values as listed in Table 4.4.

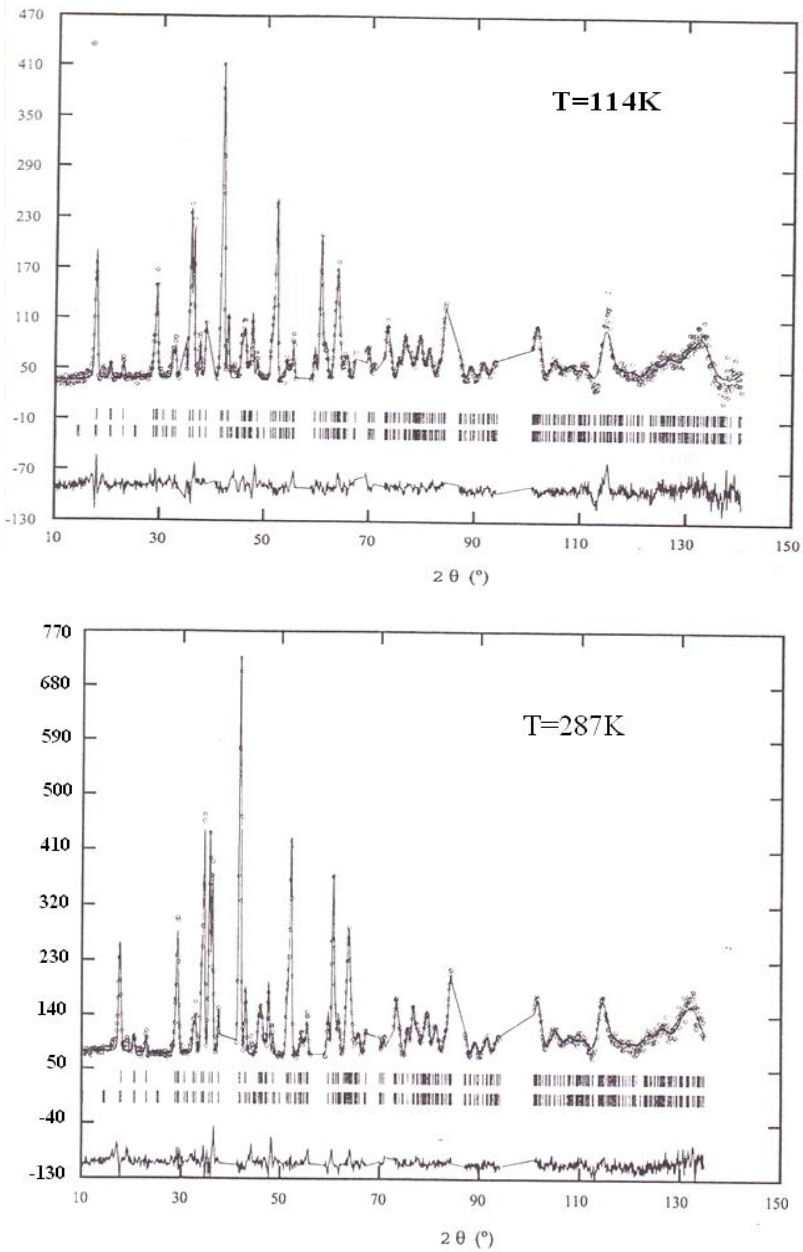

Fig. 4.10 *The neutron diffraction patterns of* $NdFe_{0.6}Mn_{0.4}O_3$ *at different temperatures.*

The obtained lattice parameters, positional and thermal parameters are in a good agreement with those given in the literature for similar compounds [8, 9]. The crystal structure does not change with changing the concentration of iron as all the samples have the same space group.

Table 4.3 *Cell parameters and Volume of* $Nd_{0.65}Sr_{0.35}Mn_{0.4}Fe_{0.6}O_3$.

X	*a*	*b*	*c*	V
0.2	5.4726(9)	7.6776(13)	5.4361(8)	228.406(3)
0.4	5.4527(9)	7.7283(10)	5.4441(8)	229.415(3)
0.6	5.4638(5)	7.7413(6)	5.4560(5)	230.772(2)
0.6*	5.4627(2)	7.7297(2)	5.4573(1)	230.435(1)
0.8	5.4249(14)	7.7210(17)	5.4622(17)	233.406(5)

* neutron diffraction

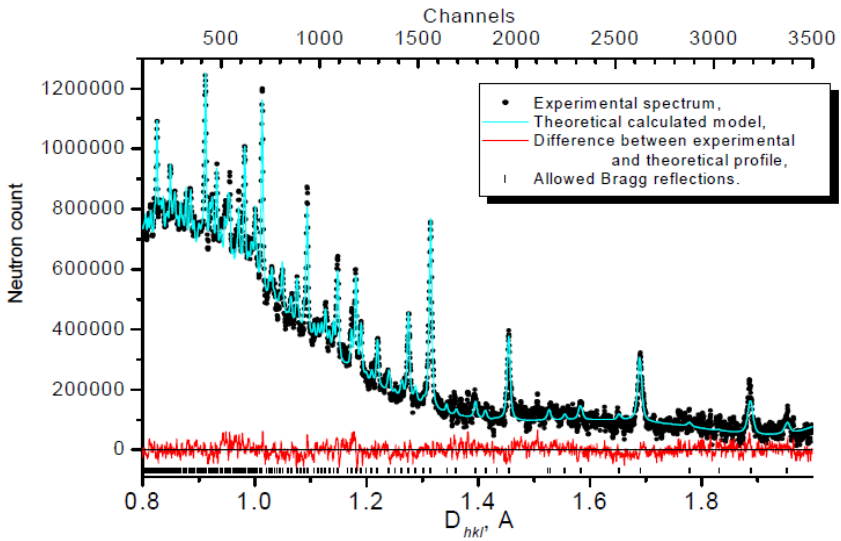

Fig. 4.11 *The neutron diffraction patterns of* $Nd_{0.65}Sr_{0.35}Mn_{0.4}Fe_{0.6}O_3$.

Table 4.4 *Thermal parameters of* $Nd_{0.65}Sr_{0.35}Mn_{0.4}Fe_{0.6}O_3$.

U_{ij}	X	Nd/Sr	Fe/Mn	O1	O2
U_{11}	0.2	0.0305	*0.0121*	*0.0880*	0.0701
	0.4	0.0102	*0.0880*	*0.0354*	0.0657
	0.6	0.0149	*0.0937*	*0.0299*	0.0960
	0.8	0.0106	*0.0601*	*0.0957*	0.0710
U_{22}	0.2	0.0305	*0.0121*	*0.0880*	0.0701
	0.4	0.0102	0.0880	0.1554	0.0657
	0.6	0.0149	0.0937	0.0299	0.0960
	0.8	0.0106	0.0601	0.0957	0.0710
U_{33}	0.2	0.0305	0.0121	0.0880	0.0360
	0.4	0.0102	0.0880	0.1554	0.0327
	0.6	0.0149	0.0937	0.0299	0.0477
	0.8	0.0109	0.0031	0.0470	0.0340
U_{12}	0.2	0	0	0	0
	0.4	0	0	0	0.0058
	0.6	0	0	0	0
	0.8	0	0	0	0
U_{13}	0.2	0.2787	0	0	0
	0.4	-0.0365	0	0	0.0006
	0.6	0	0	0	0
	0.8	0	0	0	-0.0085
U_{23}	0.2	0	0	0	0
	0.4	0	0	0	-0.0038
	0.6	0	0	0	0
	0.8	0	0	0	0

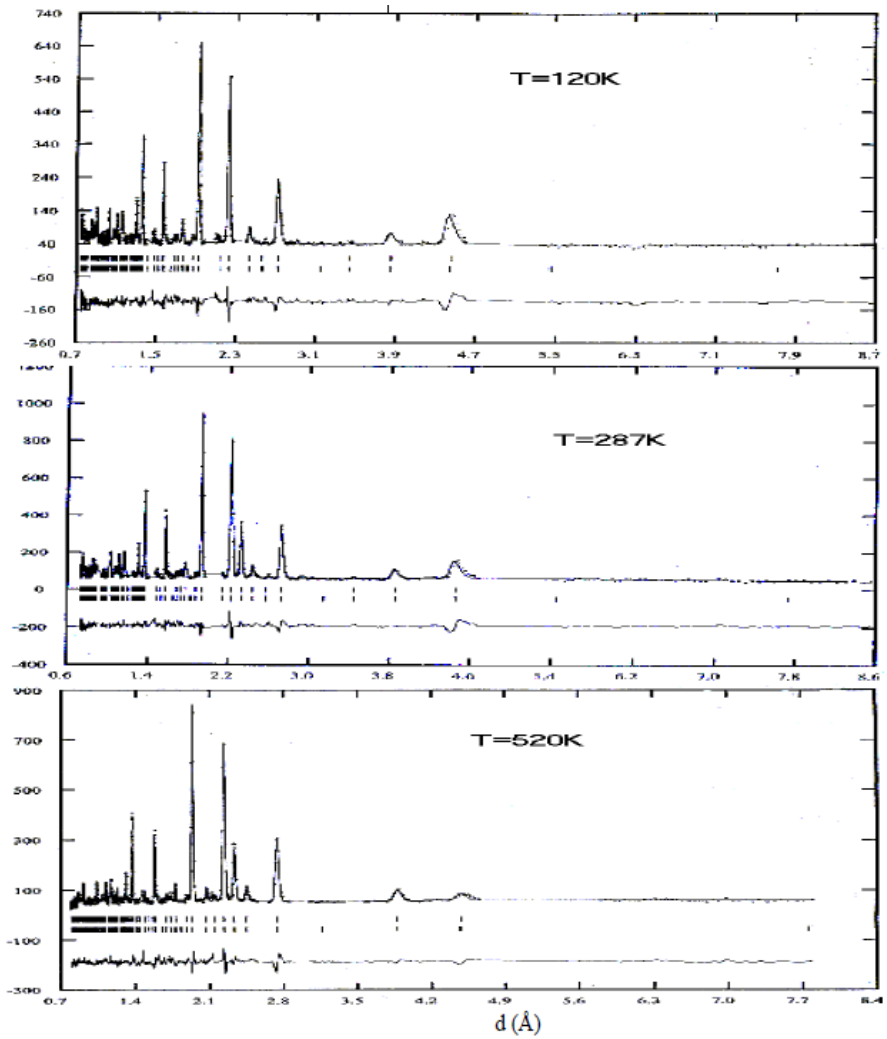

Fig. 4.12 *The neutron diffraction patterns of* $Nd_{0.65}Sr_{0.35}Mn_{0.4}Fe_{0.6}O_3$ *at different temperatures.*

Table 4.5 *The component of magnetic moment for $NdFe_{0.6}Mn_{0.4}O_3$ and $Nd_{0.65}Sr_{0.35}Fe_{0.6}Mn_{0.4}O_3$ at different temperatures.*

T, K	3d-atom	*μ(x)*	*μ(y)*	*μ(z)*	
114	Mn1/Fe1	2.719(40)	0(0)	0.922(127)	$NdFe_{0.6}Mn_{0.4}O_3$
	Mn2/Fe2	-2.719(40)	0(0)	0.922(127)	
	Mn3/Fe3	-2.719(40)	0(0)	0.922(127)	
	Mn4/Fe4	2.719(40)	0(0)	0.922(127)	
287	Mn1/Fe1	2.303(35)	0(0)	0.991(92)	
	Mn2/Fe2	-2.303(35)	0(0)	0.991(92)	
	Mn3/Fe3	-2.303(35)	0(0)	0.991(92)	
	Mn4/Fe4	2.303(35)	0(0)	0.991(92)	
120	Mn1/Fe1	-0.622(0)	0.113(0)	2.541(238)	
	Mn2/Fe2	-0.622(0)	0.113(0)	2.541(238)	
	Mn3/Fe3	-0.622(0)	0.113(0)	2.541(238)	
	Mn4/Fe4	-0.622(0)	0.113(0)	2.541(238)	
287	Mn1/Fe1	-0.622(0)	0.113(0)	2.023(253)	$Nd_{0.65}Sr_{0.35}Fe_{0.6}Mn_{0.4}O_3$
	Mn2/Fe2	-0.622(0)	0.113(0)	2.023(253)	
	Mn3/Fe3	-0.622(0)	0.113(0)	2.023(253)	
	Mn4/Fe4	-0.622(0)	0.113(0)	2.023(253)	
520	Mn1/Fe1	0.740(104)	0(0)	1.0(1)	
	Mn2/Fe2	-0.74 (10)	0(0)	1.0(1)	
	Mn3/Fe3	-0.74 (10)	0(0)	1.0(1)	
	Mn4/Fe4	0.740(104)	0(0)	1.0(1)	

Table 4.6 *The Fe-O bond length for $Nd_{0.65}Sr_{0.35}Fe_xMn_{1-x}O_3$.*

X	0.2	0.4	0.6	0.8
Fe-O_1	1.9954	1.9347	1.9451	1.9413
Fe-O_2	1.7124	1.7704	1.2207	1.4931
Fe-O_2	2.2182	2.1164	3.2971	4.3408
<Fe-O1>	1.9753	1.9754	2.1543	2.5917

The neutron diffraction patterns of the $Nd_{0.65}Sr_{0.35}Fe_{0.6}Mn_{0.4}O_3$ sample, using multi detector diffractometer, at different temperatures (120 K, 287 K and 520 K) are illustrated in Fig. 4.9. The magnetic structure analysis of these diffraction patterns shows that this compound has ferromagnetic character at

120 K and 287 K temperatures. The analysis allows to determine the projections of the magnetic moment at x-, y- and z-axis and the resulting magnetic moment (see Table 4.5). The resulting magnetic moments at 120K and 287 K are 2.6 μB and 2.1 μB, respectively. The projections of the magnetic moment in x and z - directions have the same value and orientation (0.1 μB and –0.6 μB) while there is a difference only in the value of magnetic moment in y-projection where it takes 2.5 μB at 120 K and 1.9 μB at 287 K. In the case of the T =520 K, there is a change in the magnetic ordering where non-collinear magnetic ordering of 1.2 μB resulting magnetic moment is obtained. The projection of magnetic moment in x-axis is equal to zero and in y-axis is equal to 1 μB while in z-axis there are two opposite values ± 0.7 μB between them angle of 73°. From the above, one can say that phase transition, from the pure ferromagnetic ordering into the non-collinear ordering (weak ferromagnetic), occurs near the 520 K temperature.

4.3 Raman Scattering

Raman spectra of $Eu_{0.65}Sr_{0.35}Fe_xMn_{1-x}O_3$ (x=0.1 and 0.5) are shown in Fig. 4.10 and Fig. 4.11, where the frequencies of the experimental peaks of are illustrated. With lower Fe content (x=0.1) in $Eu_{0.65}Sr_{0.35}Fe_xMn_{1-x}O_3$, the spectrum is exhibiting new spectral features. First, the A_{1g} mode is shifted toward lower frequency 210 cm^{-1} compared with A_{1g} in $Eu_{0.6}Sr_{0.4}MnO_3$ which is 238 cm^{-1}, see ref., [29]. With increasing the iron content the A_{1g} mode in x=0.5 is shifted toward higher frequency 216 cm^{-1}. As well as in lower iron concentration the $B_{2g}(1)$ mode is shifted toward lower frequencies, $B_{2g}(1)$ mode shift at frequency equal to 488 cm^{-1}, while it is shifted toward higher frequency 491 cm^{-1} with increasing iron concentration (x=0.5). For $B_{2g}(3)$ mode it is found at frequency equal to 610 cm^{-1} for samples of x=0.1. This $B_{2g}(3)$ mode of Raman spectrum for x=0.5 is shifted to higher frequency than in the case of

x=0.1 to give frequency equivalent to 632 cm^{-1}. The low-frequency mode at 210 cm^{-1} and 216 cm^{-1} have been attributed to the A_{1g} mode, which is the in phase rotation of the oxygen cage about the y-axis to adjacent MnO_6 octahedra. The two high-frequency modes at 488 and 610 cm^{-1} for x=0.1 and at 491 and 632 cm^{-1} for x=0.5) are associated with the out-of-phase bending of the MnO_6 octahedra ($B_{2g}(3)$) and the symmetric stretching of the basal oxygen ions ($B_{2g}(1)$), respectively. According to the Martin–Carron et al. [30], the peak corresponding to $B_{2g}(1)$ mode correlated with the Jahn –Teller distortion for compounds with large ionic radii. The increase in the distortion may lead to the increase of the frequency that is the same in our case the distortion of $Eu_{0.65}Sr_{0.35}Fe_xMn_{1-x}O_3$ increases with increasing the concentration of iron as reported by Farag et al., in ref [13]. The tilt angle increase with increasing the iron concentration. The tolerance factor are the same for both x=0.1 and x=0.5 (t=0.96).

The rare-earth manganites $RMnO_3$ where R with smaller ionic radius like Ho, Er, Tm, Yb, Lu of hexagonal structure and of space group P_{63cm} (C^3_{6v}) with Z=6 can be converted to the orthorohombic phase of space group $Pnma$ (D^{16}_{2h}) with Z=4. The results of group-theoretical analysis for the Γ-point phonons of orthorhombic gives the irreducible representations for the R, Mn and O atoms in the orthorhombic structure that occupy 4(c), 4(b) and 4(c), respectively (they are 12 for each Wyckoff position) [32]. For R atoms $\Gamma = 2A_g + B_{1g} + 2B_{2g} + B_{3g} + A_u + 2B_{1u} + B_{2u} + 2B_{3u}$, for Mn atoms $\Gamma = 3A_u + 3B_{1u} + 3B_{2u} + 3B_{3u}$ and for O atoms in 4(c) position $\Gamma = 2A_g + B_1g + 2B_2g + B_{3g} + A_u + 2B_{1u} + B_{2u} + 2B_{3u}$. For 8(d) oxygen atoms $\Gamma = 3A_g + 3B_{1g} + 3B_{2g} + 3B_{3g} + 3A_u + 3B_{1u} + 3B_{2u} + 3B_{3u}$. From the total 60 Γ-point phonon modes, there are 24 ($7A_g+5B_{1g}+ 7B_{2g} + 5B_{3g}$) are Raman active, 25 ($9B_{1u}+7B_{2u}+9B_{3u}$) are infrared-active, 8($8A_u$) are silent, and 3($B_{1u} + B_{2u}+ B_{3u}$) are acoustic modes [54]. According to Ghosh et al., [55] the

hexagonal rare earth manganites ($RMnO_3$ where R is Y, Yb, Ho or Er of P_{63cm} space group) which contain six formula units per unit cell (Z=6) have 38 Raman active phonon modes ($9A_1$, $14E_1$ and $15E_2$). From Fig. 4.10 one can note that Raman modes of $Yb_{0.6}Sr_{0.4}MnO_3$ and $Yb_{0.9}Sr_{0.1}MnO_3$ may correspond to both hexagonal and orthorhombic symmetries. Raman modes for $Yb_{0.6}Sr_{0.4}MnO_3$ are the observed at frequencies; 156. 178, 471, 526 and 678 cm^{-1} while the observed modes for those of $YMnO_3$ hexagonal structure reported by Yue-Feng [56] we can find the consistency only with the following Raman modes; A_1 (152 cm^{-1}), E_2 (308 cm^{-1}), E_2 (300 cm^{-1}), E_2 (412 cm^{-1}), A_1 (433 cm^{-1}) and A_1 (685 cm^{-1}) see table 4.7. These modes exist in our case but shifted little bit because the difference in the ionic radius of the elements constituent $YMnO_3$ and both $Yb_{0.9}Sr_{0.1}MnO_3$ and $Yb_{0.6}Sr_{0.4}MnO_3$. Comparing the remained modes with those modes belong to the orthorhombic symmetry, like the case given in ref. [34-35] for $NdMnO_3$ of the orthorhombic symmetry, may give interpretation for the coexistence of the hexagonal symmetry with the orthorhombic symmetry in the same time. The hexagonal symmetry are the predominated in both cases but the orthorhombic symmetry in $Yb_{0.9}Sr_{0.1}MnO_3$ is more pronounced than in $Yb_{0.6}Sr_{0.4}MnO_3$.

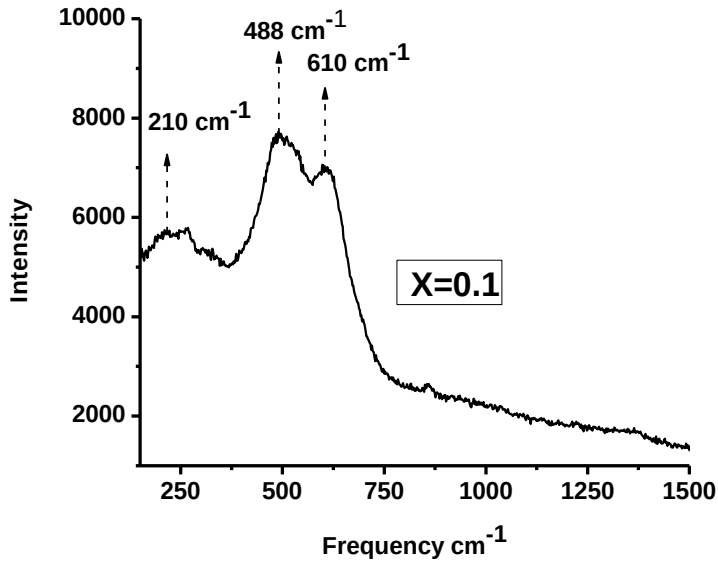

Fig. 4.13 *Raman Spectra of* $Eu_{0.65}Sr_{0.35}Mn_{0.9}Fe_{0.1}O_3$.

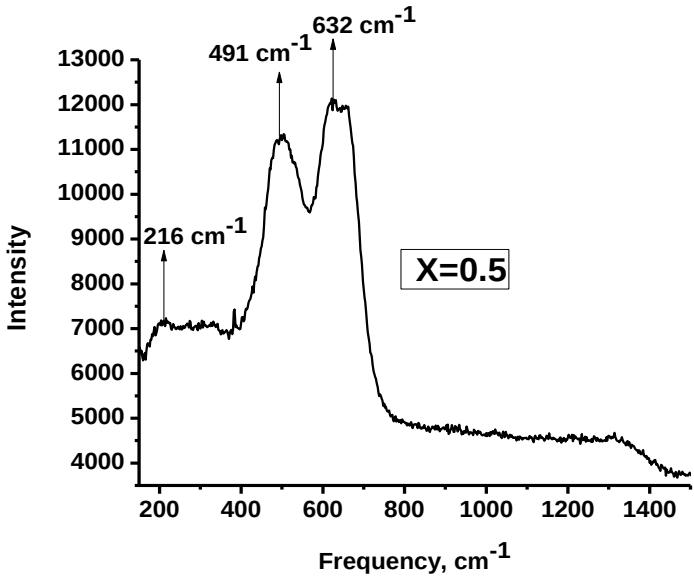

Fig. 4.14 *Raman Spectra of* $Eu_{0.65}Sr_{0.35}\ Fe_{0.5}Mn_{0.5}O_3$.

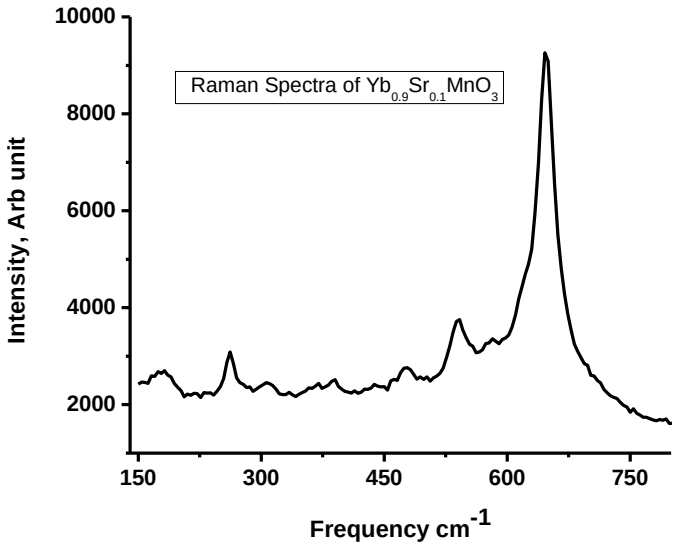

Fig. 4.15 *Raman spectra of both $Yb_{0.6}Sr_{0.4}MnO_3$ and $Yb_{0.9}Sr_{0.1}MnO_3$. $Yb_{0.9}Sr_{0.1}MnO_3$ at the following frequencies; 180, 261, 309, 379, 476, 540, 581 and 645 cm^{-1}. Compared these frequencies with.*

Table 4.7 *Raman modes of $Yb_{0.9}Sr_{0.1}MnO_3$ and $Yb_{0.6}Sr_{0.4}MnO_3$.*

Raman mode	$YMnO_3$	$NdMnO_3$ O	$Yb_{0.9}Sr_{0.1}MnO_3$	$Yb_{0.6}Sr_{0.4}MnO_3$
A1	h 152 [33],		-	156 [21]
Ag	O 151 [31]			
E2	h 300 [34]		309 [21]	-
E2	h 412 [33]		379 [21]	-
A1	h 433 [33]		476 [21]	471 [21]
A1	h 665 [33]		645 [21]	678 [21]
Ag	O 188 [31]	200 [34]	180 [21]	178 [21]
B1g		522 [35]	540 [21]	526 [21]
B3g		282 [35]	261 [21]	-
B2g		601 (23)	581 [21]	-

h = hexagonal and O = orthorhombic

5

Electrical and Magnetic Transport of 3d-4f Oxides

The electric, magnetic and dielectric properties of 3d-4f oxides are very interesting and give us possibility to use these oxides in the industrial scale and understanding their unique properties which makes these materials under the scopes of scientific interests. Let us take a look on some examples of these oxides and some results and their analysis.

5.1 Electric Properties of 3d-4f Oxides

The DC resistivity – temperature dependence measurements of $Eu_{0.65}Sr_{0.35}Fe_xMn_{1-x}O_3$ (x=0.1 and 0.5) after sintering at 1350 ℃ for 72 hours are shown in Fig. 5.1. The temperature dependence of the resistivity curve of both samples shows the semiconductor behavior where the resistivity of $Eu_{0.65}Sr_{0.35}Fe_xMn_{1-x}O_3$ decreases with increasing temperature. The relation between resistivity and temperature expressed in the exponential dependence and the well known Arrhenius equation gives the best fitting of the experimental measurements [36];

$$\rho = \rho_0 e^{\frac{-E}{kT}} \tag{5-1}$$

where ρ_0 is the resistivity at room temperature, E is activation energy, k is Boltzmann constant and T is absolute temperature (see fig. 5.1 and fig. 5.2).

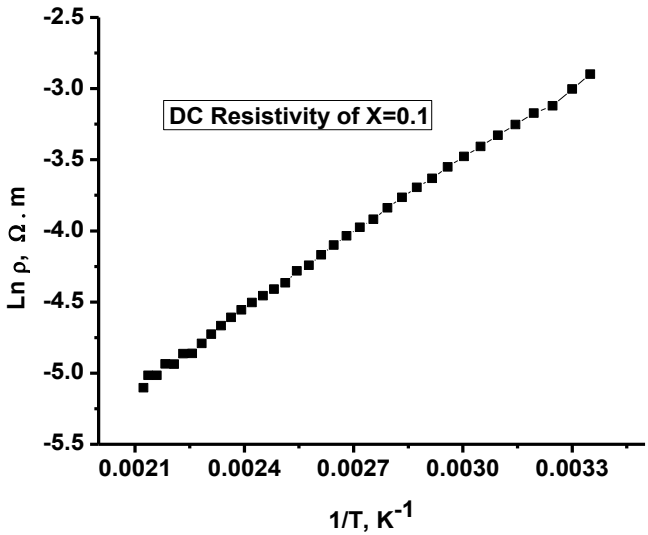

Fig. 5.1 *DC resistivity – temperature dependence of* $Eu_{0.65}Sr_{0.35}Mn_{0.9}Fe_{0.1}O_3$.

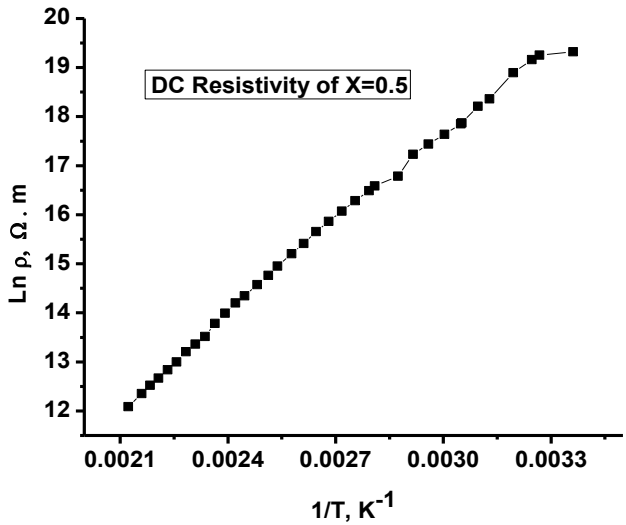

Fig. 5.2 *DC resistivity – temperature dependence of* $Eu_{0.65}Sr_{0.35}\ Fe_{0.5}Mn_{0.5}O_3$.

The electrical conductivity is generally expressed as,

$$\sigma = ne\mu \tag{5-2}$$

where e is the unit charge, n is the concentration of charge carriers and μ is the mobility of charge carriers. The concentration of charge carriers, n is given as

$$n = N.\exp\left(\frac{-E_g}{2KT}\right) = NC \tag{5-3}$$

where E_g is the energy required to create cations of different charges by separating an excited electron from the hole it leaves behind, [73] N is the concentration per formula unit of lattice sites that are available to the charge carriers and C is the fraction of the available lattice sites occupied by the charge carriers.

The mobility of charge carriers, μ is given as

$$\mu = \left[\frac{(1-C)e\ a^2v}{KT}\right]\exp\ (\frac{-E_a}{KT}) \tag{5-4}$$

where a is the lattice spacing, υ is vibration frequency, k is the Boltzmann constant, T is the absolute temperature and E_a is a hopping activation energy [74].

The temperature dependence of conductivity is described in the expressions of n and μ. For oxide semiconductors, n and μ usually increase with temperature. Nevertheless, at equilibrium condition and in air, the concentration of charge carriers is maintained to be constant. Therefore, Eq. (5-3) can be rewritten as $n = NC = Constant$ and thus the temperature dependence of conductivity is described only by μ, as in Eq. (4.4). With Eq. (5-4) being substituted in Eq. (5-2), the expression for the temperature-dependent electrical conductivity of the small polaron material becomes

$$\sigma = \left(\frac{A}{T}\right)\exp\ (\frac{-E_a}{KT}) \tag{5-5}$$

where A is the pre-exponential factor, defined as

$$A = \frac{NC\,(1-C)e^2a^2v}{K} \tag{5-6}$$

The semiconductor-like transport behavior is characterized with three models. (1) a band-gap model (An Arrhenius law), $\rho = \rho_0 \exp\left(\frac{-E_B}{KT}\right)$ is generally used to describe the thermally activated behavior due to a band gap E or a mobility edge; (2) Nearest-neighbor hopping model of small polarons, $\rho = (\rho_0.T)\exp\left(\frac{E_B}{K_BT}\right)$; (3) If the carriers are located in random potential, Mott's a variable - range hopping model (MVRH) expression $\rho = \rho_0 \exp\left(\frac{T_0}{T}\right)^{\frac{1}{4}}$ is appropriate [75]. Thus in order to understand the transport mechanism in $Nd_{0.6}Sr_{0.4}Mn_xCo_{1-x}O_3$, it is necessary to fit the resistivity curves based on these three models.

It has been believed that the electrical properties are controlled by the motion of an e_g electron from Mn^{3+} $(t_{2g}^3 e_g^1 : S = 2)$ to Mn^{4+} $(t_{2g}^3 e_g^0 : S = 3/2)$ via the intervening oxygen.

The influence of annealing on decreasing resistivity for $Nd_{0.6}Sr_{0.4}CoO_3$ composition is shown in ref [76]. One can note high resistivity for as prepared sample while resistivity vanished for sample heated at 850 ℃ which is attributed to the decrease of grain size relatively increases the insulating region due to the enhancement of the grain boundary effects. This behavior is in agreement with the earlier report [77].

The metal behavior for $Nd_{0.6}Sr_{0.4}CoO_3$, which keeps a full metallic-like behavior during temperature range 300–440 K is presented in ref [76]. No sharp peak in ρ is observed at 440 K (T_p) (Metal - insulator transition) but there is accompanied a broad maximum around ~ 440 K T_m, which is attributed to

oxygen deficient components having distribution of oxygen stoichiometry lead to the broad maximum at T_m. [78] These compound has a distinct metallic phase below the transition temperature (T_m) and above this temperature it becomes semiconducting. The (M–S) transition is believed to arise from the increase of Co–O–Co bonding angle. [79]

It is well established that cobalt exhibits different spin state. The low spin (LS, $t_{2g}^6 e_g^0$) state changes to either higher spin (HS, $t_{2g}^4 e_g^2$) or intermediate spin (IS, $t_{2g}^5 e_g^1$) state with increasing temperature [89]. Therefore, the population of Co(IS) changes to LS state at low temperature, which creates an additional distortion in the lattice due to the smaller ionic size of the low spin Co^{3+} ion. A a result, buckling of CoO_6 octahedral increases, which in turn affects the charge transfer integral along the Co-O-Co bonds. This effect is probably the reason for monotonous increase in the resistivity behavior of the Co-containing samples [175] [75].

The linear fitting of ln ($\rho/\ \rho_0$) virius 1/T for x = 0 as prepared sample according to band gap model (thermal activation conduction) (TAC). The activation energy can be calculated using this model to be E_p = 0.529 eV. It can be observed that the semiconductor behavior covered all temperature range for as prepared compound and a little resitivity dependence temperature is observed for heated at 850 ℃ compound, which is attributed to the increase of particles size due to thermal treatments. Fig. 5.3 shows the DC resistivity – temperature dependence of $Nd_{0.6}Sr_{0.4}CoO_3$.

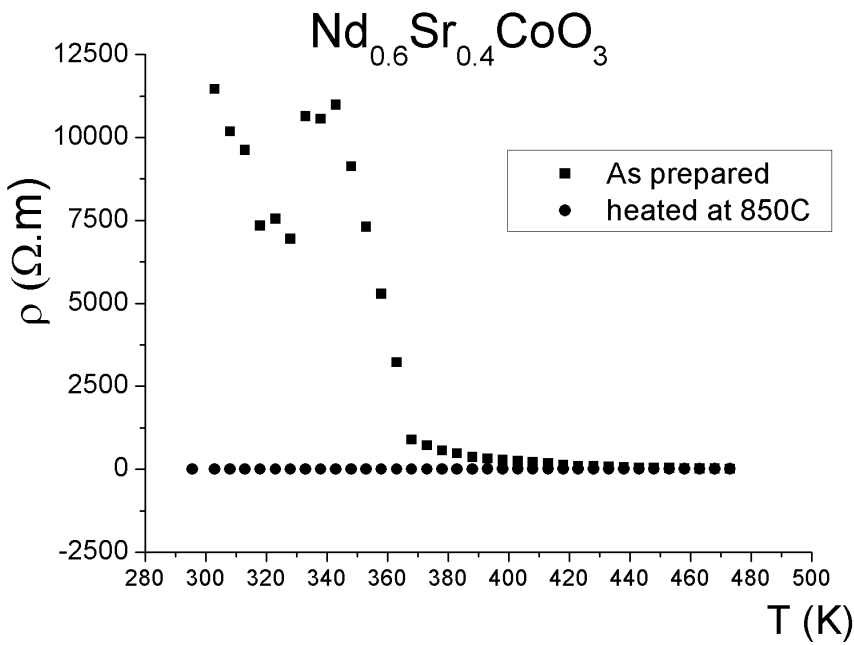

Fig. 5.3 *DC resistivity – temperature dependence of* $Nd_{0.6}Sr_{0.4}CoO_3$.

Similarly, the relation between electrical resitivity and temperature for x = 0.3 as prepared is shown where the semiconductor behavior is noticed in low temperature range, the curve has a peak at T_p = 90 ℃ and beyond T = 90 ℃ the resistivity is suppressed.

For thermal treatment samples the resistivity ρ(T) is so low and temperature independence of the resistivity ρ(T) is noticed. The influence of thermal treatment in decreasing resistivity for $Nd_{0.6}Sr_{0.4}Mn_{0.3}Co_{0.7}O_3$ compound is attributed to the increasing of the particles size. [80]

This large variation in the electrical behaviour could be due to the different annealing treatments which induce an important change in the crystallite and grain sizes, as evidenced by SEM and the comparison of the $D_{h\,k\,l}$ values. It can be considered that the increase of ρ with the reduction of grain size is mainly related

to the increase of both the height and width of tunneling barriers. Evidently, with the grain size decreasing the number of pores and consequently, the porosity increase. The increase of ρ with the grain size decrease is a result of carriers sampling and more grain boundary material. The large volume of grain boundary material produces a greater electrical conductivity change. In these cases, the influence on the electrical transport properties of the mixed valence manganese ions is less important. In fact, it was found that for fine-particle perovskite manganites, an increase in resistivity occurs as the particle size decreases and the grain boundary contribution increases due to the broken Mn–O–Mn bonds at the surface of the smaller articles that impede the conduction. This is a typical behaviour in the case of nanoparticles of the manganite system. [81]

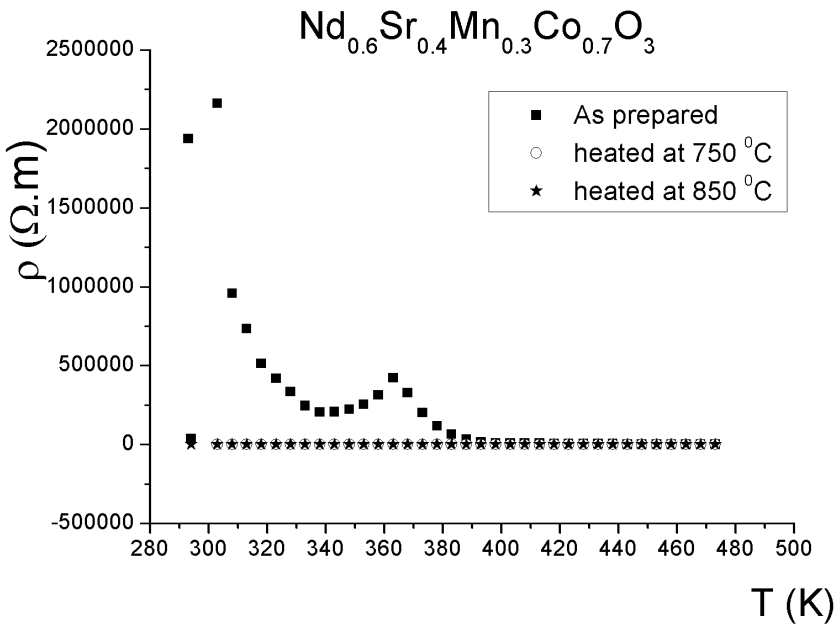

Fig. 5.4 *The DC resistivity – temperature dependence measurements of* $Nd_{0.6}Sr_{0.4}Mn_xCo_{1-x}O_3$ *(x = 0.3).*

The resistivity ρ increases systematically with decreasing grain size over the whole range of temperature. This is not surprising considering that ρ is increasingly influenced by the presence of grain boundaries, which act as regions of enhanced scattering for the conduction electrons and disorder. Isaac et al. and Sanchez et al. showed that the spin becomes heavily disordered at the grain boundary due to the strain with the lowering of the grain size which may result in a growth of the resistivity. It is also seen that the resistivity reduces drastically with grain growth, as the bound- arise of the grains consist of more magnetic disorder than the cores. Gupta et al. explain the variation in properties with grain size as the reflection of magnetic disorder induced canting of Mn spins near the surface of the grains.

From the DC resistivity – temperature dependence of $Nd_{0.6}Sr_{0.4}MnO_3$ composite annealed at 850 ℃ (see Fig. 5.5) it is clear that the semiconductor behavior is well represented with the exponential dependence. According to the well known formula given in equation (5.7) for resistivity – temperature dependence;

$$\rho = \rho_0 \exp\left(\frac{-E}{KT}\right) \tag{5-7}$$

According to this formula one can calculate the activation energy which has the value of E = 0.2154 eV which in good agreement with those reported in ref. [82]

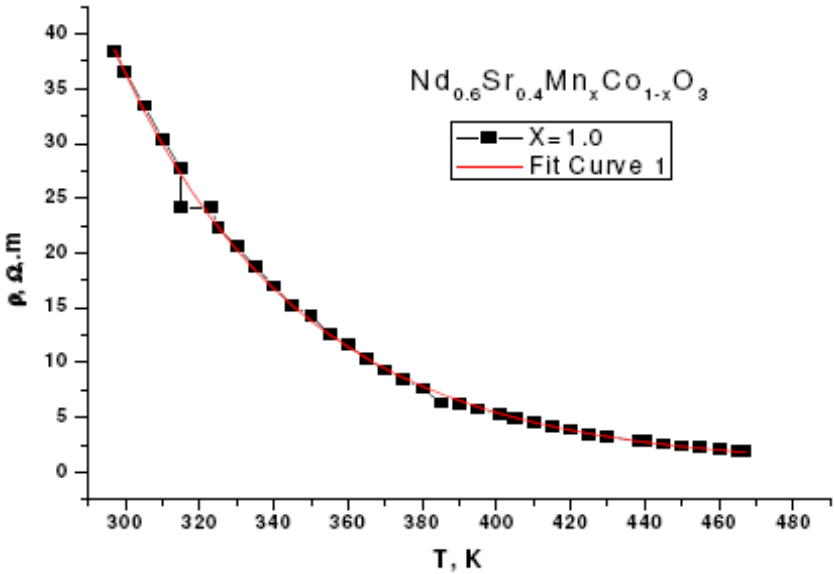

Fig. 5.5 *The DC resistivity – temperature dependence measurements of* $Nd_{0.6}Sr_{0.4}Mn_xCo_{1-x}O_3$ *(x=1).*

The DC resistivity – temperature dependence measurements (Fig. 5.5) of $Nd_{0.6}Sr_{0.4}Mn_xCo_{1-x}O_3$ as prepared showed decrease of resistivity with the increase of temperature which explains the semiconductor behavior of these compounds. From the DC resistivity – temperature dependence measurements it is clear that there are phase transition points at temperatures 338 K, 363.3 K, 358.5 K and 340 K corresponding to x = 0, 0.3, 0.7 and 1, respectively. The semiconductor behavior was noted for all samples without annealing. The observed resistivity for the samples as prepared are too high compared with those annealed. This high resistivity of the sample after chemical reaction without annealing is attributed to the small crystalline size. The crystalline size of the samples without annealing (as prepared) are 15.5 nm, 43.4 nm and 45.6 nm for x = 0, 0.3 and 0.7 respectively.

The DC resistivity – temperature dependence measurements of $Nd_{0.6}Sr_{0.4}Mn_xCo_{1-x}O_3$ after annealing at 850 ℃ for 12 hours are shown in

Fig. 5.4 and Fig. 5.5 (x = 0, 0.3 and 0.7). The temperature dependence of the resistivity curve of the samples where x = 0 shows the metallic behavior and there is transition to semiconductor at T = 443 K. The same behavior is represented by the sample where x = 0.3 but the transition temperature is observed at T = 333 K. In the case of x = 0.7 the behavior is completely different because there is linear relation between the temperature and resistivity indicating the metallic behavior without no transition point. This behavior is ascribed to the presence of an appreciable concentration of Mn^{3+} which introduces a large number of charge carriers (electrons) and facilitates the movement of those charge carriers by hopping mechanism. So the electron hopping between Mn^{3+} and Mn^{4+} can be responsible for both the metallic behavior and the relatively low electrical resistivity exhibited by the substituted phases. [24]

It was found that (ρ) always decreases with increasing temperature for the two compositions. Obviously, the resistivity increases with Co doping. On other hand, the figure shows that the peak transition (M–S) for x = 0.7 at T=313 K. This compound (x = 0.7) has a distinct metallic phase below the transition temperature (T_m) and above this temperature they become semiconducting. The (M–S) transition is believed to arise from the increase of Mn–O–Mn bonding angle [83] for composition with (x = 0.3), there are logarithmic decreasing in resistivity with increasing temperature which is implied the semiconductor behavior. Hence, the composition (x = 0.3) behaves as semiconducting material (no transition).

The reported resistivity results in $LaMn_{1-x}Co_xO_3$ reveal that ρ is increased considerably due to the Co substitution where the value of ρ for x = 0.15 is one order of magnitude lower than that of the value for x = 0. [85] The reported results suggest that Co^{2+} appears as a result of Co substitution which leads to the

charge redistribution, $Mn^{3+} + Co^{3+} \rightarrow Mn^{4+} + Co^{2+}$ Thus, appearance of Co^{2+} causes the increase in ratio of Mn^{4+}/Mn^{3+}, leading to the further enhancement of DE mechanism. [86]

Finally the DE interaction is stronger for Mn^{3+}- O^{2-} - Mn^{4+} in comparison to that of Co^{3+}- O^{2} -Co^{4+}. Then, the ratio of Mn^{3+}/Mn^{4+} decreases with Co content, increasing Co^{3+}/Co^{4+} ratio. The resistivity value increase as the concentration of cobalt ion increases due to suppression of DE that leads to ferromagnetism. [86]

The spin- spin scattering increase as the concentration of Co increases. The activation energy for polaron hopping as well as small polaron stabilization energy is high in the case of Co-substituted system. The number of charge carriers decreases with increasing Co content, as a result of which resistivity values increase [87].

In the present observation, the considerable decrease of ρ due to the small Co substitution might also be involved with the enhancement of DE mechanism which is more dominating than that of the disorder introduced by the Co substitution. The other plausible interpretation for the decrease of ρ is the modification of the grain boundary region due to the Co substitution where Co substitution weakens the grain boundary effect, leading to the considerable decrease of ρ. At low temperature a minimum in the temperature dependence of ρ is observed. The temperature at which minimum is observed, is shifted towards high temperature as a result of minimal substitution.

Fig. 5.7 plots the electrical conductivity (log σT) as a function of temperature versus 1/T, obtained for $Nd_{0.6}Sr_{0.4}Mn_xCo_{1-x}O_3$ (x = 0.3, 0.7) sintered at 750 ℃ temperature. The activation energy of electrical conduction calculated according to Bottger and Bryksin model $\sigma = \left(\frac{A}{T}\right) \exp\left(\frac{-E_h}{KT}\right)$ to be 0.142 and 0.6922 eV for x = 0.3 and x = 0.7 respectively. The activation energy of conduction shows that

these materials are oxide ion conductors. This emphases that the conductivity increases and the activation energy decreases with increasing the manganese concentration as in. [70]

In addition, it is well known that the mechanism of electrical conduction in (R,Sr)MnO_3 (R = Nd, Ce, Ho, Eu, Sm) is by hopping of polarons [12, 16, 24–27, 30]. For conduction to occur, Mn^{3+} and Mn^{4+} should be the nearest neighbours and the electron jumps from Mn^{3+} to Mn^{4+} must be via O^{2-} (i.e. Mn^{3+}–O–Mn^{4+} bonding). As a consequence the activation energy of total conduction can be evaluated using the Arrhenius equation:

$$\sigma = \left(\frac{A}{T}\right) Exp\ \left(\frac{-E_a}{KT}\right) \tag{5-8}$$

where σ is the conductivity, A the pre-exponential factor, k the Boltzmann's constant, T the absolute temperature and Ea the activation energy of conduction. Using Eq. (4.8) the activation energy of conduction values were estimated from the slope of the linear portion of log (σ.T) vs. 1/T.

The activation energies obtained for $Nd_{0.6}Sr_{04}Mn_xCo_{1-x}O_{3-\delta}$ (x = 0.3, 0.7) as substituted samples increases monotonically with Mn content for both sintering temperatures. The more substitution of Mn leads to a higher Mn^{3+} content and, as a consequence, the lowering of the energy barrier for polaron hopping. As mentioned earlier, [87-88] some authors verified that the activation energy values increase with decreasing grain size.

In fact, increasing grain size the interconnectivity between grains increases, which enhances the possibility of conduction electrons to hop to the neighboring sites, thereby decreasing the E_a value. Furthermore, for the Mn-substituted samples the activation energy increases slightly with manganese content, which can be linked to the increase of structural distortions, owing to the enhancement of energy barrier for polaron hopping. [89].

The activation energies for sintering compositions at 850 ℃ according to band gap model $\rho = \rho_0 \exp\left(\frac{-E_p}{KT}\right)$ are 0.141, 0.142, 0.133 and 0.2154 eV for x = 0.0, 0.3, 0.7 and 1.0 respectively. One can note that the increasing in sintering temperature lead to a reduction of the activation energy i.e the activation energy decreases with increasing the manganese concentration as in [105].

The transport mechanisms such as nearest neighbour hopping, Mott's variable range hopping and Efrose - hklovskii's variable range hopping mechanisms can exhibit semiconducting behaviour. In the nearest neighbour hopping process, the donor sites are randomly distributed in space and charge carriers hop to nearest empty donor sites. It is found that the deviation for the nearest neighbour hopping mechanism is the most suitable mechanism for describing the ρ-T characteristics of manganite in the semiconducting region. The obtained activation energies for four compositions are 0.529, 0.541, 0.466 and 0.327 eV for x = 0.0, 0.3, 0.7 and 1.0 respectively. The slight increasing in activation energy E_a with increasing Co content (decreasing Mn content) is attributed to the Co substitution suppresses the DE interaction; hence, the higher activation energy is required for hopping of the e_g electrons. [75]

It is commonly accepted that the electrical conductivity is simultaneously determined by the concentration of charge carriers and their mobility. Table (5.1) shows that the E_a value decline slightly with increasing Mn content. An improved carrier's mobility is confirmed by the decreased E_a value, which implies a decrease in the poloran binding energy or an increase in the bandwidth. [90] As mentioned before, the tolerance factor decreased gradually with increasing Mn doping ratio, which implies a decrease in the bending of (Mn,Co)-O-(Mn,Co) bond and a large degree of bond overlapping. This

variation is beneficial for the Zener double exchange process, and thus contributes to the lowered hopping energy E_a.

However, the slight change in E_a's magnitude is so small as to be neglected influence. Thus it is expected that the enhanced electrical conductivity is primarily attributed to the increased concentration of charge carriers.

Table 5.1 *Activation energy and Mn content and thermal treatment.*

X=0.3		**E_p(eV)**	**x (Mn content)**
E_p(eV)	*Thermal treatment*	0.5290	0.0
0.4840	As prep.	0.4840	0.3
0.1421	750 ℃	0.4660	0.7
0.1420	850 ℃	0.3270	1.0

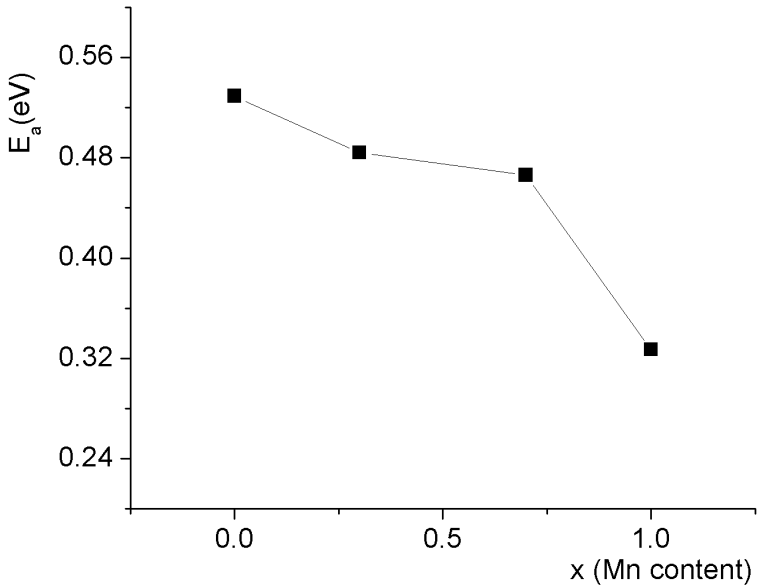

Fig. 5.6 *The relation between concentration of Mn and activiation energy of* $Nd_{0.6}Sr_{0.4}Mn_xCo_{1-x}O_3$.

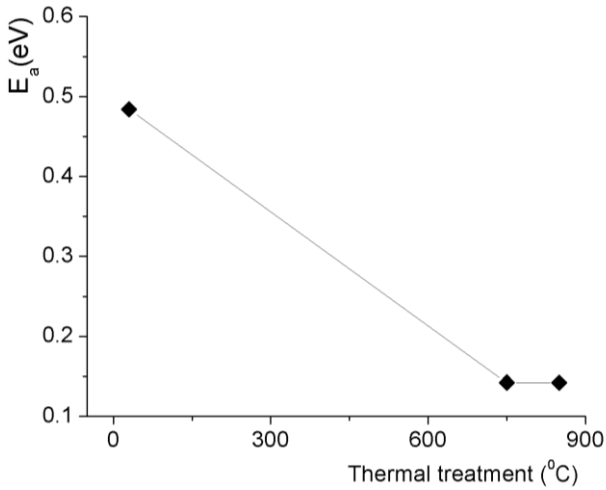

Fig. 5.7 *The effect of thermal treatment on the activation energy of* $Nd_{0.6}Sr_{0.4}Mn_xCo_{1-x}O_3$ *(x = 0.3).*

According to this formula one can calculate the activation energy which has the value of 0.152 eV and 0.535 eV for x=0.1 and x=0.5, respectively. From the linear dependence of the M – O bond length and the volume of unit cell of $Eu_{0.65}Sr_{0.35}Fe_xMn_{1-x}O_3$ on the iron concentration reported by Farag et al [13], one can correlate the increase of increase in the bond length and activation energy of $Eu_{0.65}Sr_{0.35}Fe_xMn_{1-x}O_3$ with the increasing iron concentration. This increase in bond length may explain the increase in the resistivity that is in good agreement with the case of the $Nd_{0.65}Sr_{0.35}Fe_xMn_{1-x}O_3$ in which the increase in the iron content related to the increase in resistivity as reported by Abdel-Latif *et al* [21].

The DC conductivity (σ) can be obtained from the current-voltage (I-V) characteristics at various temperatures $\sigma = \frac{G.t}{S}$, where G being the slope of the linear I-V plot, t is the thickness of the sample and S the sample area. The variations of the conductivity with temperature are usually expressed as

$\sigma = \sigma_0 e^{-E/kT}$. σ_0 can be temperature dependent and another common equation for is; $\sigma = (B/T)e^{-E/kT}$, where B is a constant, E is the activation energy defined as the energy required to release an electron hopping from one ion to the next and k is the Boltzmann constant. The variations of σ with temperature in ferrites is generally attributed to either an increase in the carrier concentration with increasing temperature (band theory) or to a hopping mechanism of electrons between ions of the same element but present in two or more valence states (example Fe^{+2} and Fe^{+3}). In both explanations an increase in temperature should lead to a consequent increase in conductivity.

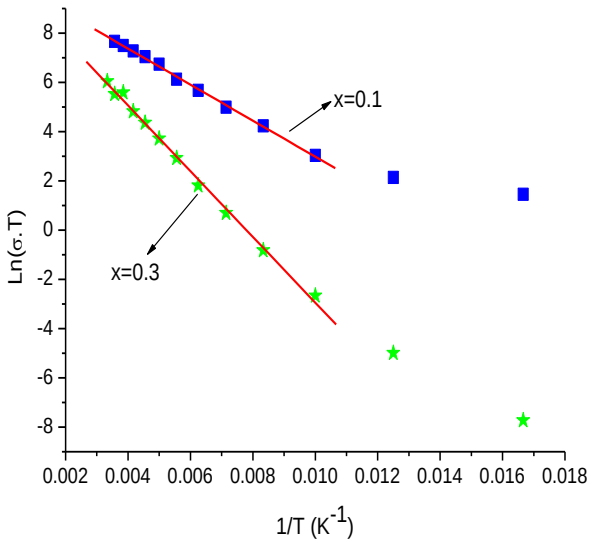

Fig. 5.8 *DC conductivity of $Nd_{0.65}Sr_{0.35}Fe_xMn_{1-x}O_3$ (x=0.1 and 0.3).*

DC conductivity of $Nd_{0.65}Sr_{0.35}Fe_xMn_{1-x}O_3$ (x=0.1 and 0.3) as a function of temperature is illustrated in Fig. 5.8. From the derived conductivities as a function of temperature it turns out that the data is better fitted with the equation $\sigma = (B/T)e^{-E/kT}$.

In fact, the Ln(σ.T) versus 1/T plots for both samples (x=0.1 and x=0.3) shown in figure 5.8 are perfectly linear except at very low temperatures (≤ 80K) where there is a slight deviation and may be a tendency to exhibit a second slope. It is quite clear that in both samples, the conductivity increases with increasing temperature. It is quite remarkable, however, that the increase in σ is by far much more pronounced in the case of the concentration of Iron at x=0.3 than in at the concentration (x =0.1). The activation energies (obtained from the slopes of plots of figure 5.8 are very much different. The obtained activation energy for the sample where x=0.1 is 0.063 eV while it is 0.115 eV for the sample where x=0.3. These activation energies are relatively low which could indicate that over the temperature range considered the samples are in the ferromagnetic regime. It is generally accepted that activation energies are higher in the paramagnetic regime than those in the ferromagnetic case [25]. Furthermore, in some ferrites two slopes are occasionally observed in the Ln(σ.T) versus 1/T plots over two temperature ranges corresponding to two different activation energies [26].

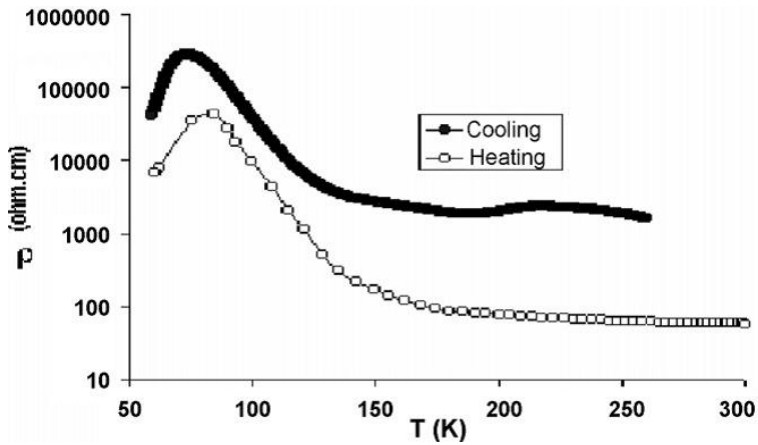

Fig. 5.9 *Temperature variation of resistivity at 0 T magnetic field of $Sm_{0.6}Sr_{0.4}MnO_3$ polycrystalline sample (in heating as well as in cooling).*

The variation in resistivity–temperature dependence behavior of $Sm_{0.6}Sr_{0.4}MnO_3$ at zero magnetic field in the case of heating from the cooling process is shown in Fig. 5.9. The resistivity increases with decreasing temperature, i.e., a semi-conducting behavior is predominant. At temperature of 71 K, a transition is observed on cooling. On heating this transition is shifted a little bit towards higher temperatures. After this temperature (T~74 K) a metallic behavior is observed. This behavior is similar to electron or hole doped manganites [36–40]. A hysteresis between heating and cooling of $\rho(T)$ is characterized. The strontium deficiency leads to an increase in the value of $\rho(T)$ as well as a decrease in the electrical transition temperature. Because we deal with granular materials where there is a possibility to get more or less insulating barriers at the grain boundaries. These barriers will limit the residual resistivity. This mechanism is well known in ceramics, in ferrite as well as in high T_c superconductors where insulating barriers cause the appearance of Josephson junction below the transition temperature of the super-conducting grains. The difference in resistivity is still obtained with applying magnetic field on the sample during the heating and cooling measurements. The dependence of phase temperature on strontium concentration in $Sm_{1-x}Sr_xMnO_3$ was reported in different papers [41-42]. There is a transition, which occurred for $Sm_{0.6}Sr_{0.4}MnO_3$ single crystal at $T_c \approx 107$K (see Ref. [41]) and at $T_c \approx 123$K. which is given in Ref. [42].

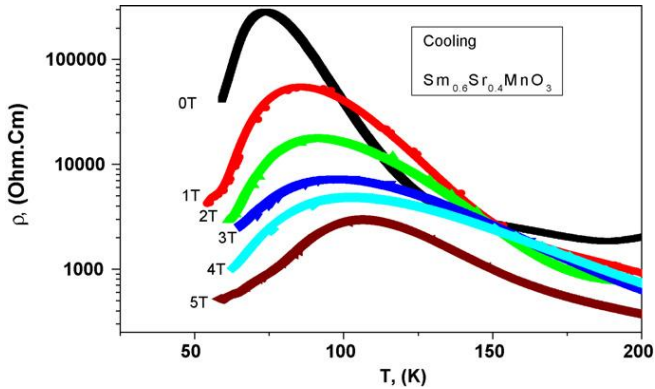

Fig. 5.10 *Thermal dependence of the resistivity at applied magnetic fields of 0 T, 1 T, 2 T, 3 T, 4 T and 5 T of $Sm_{0.6}Sr_{0.4}MnO_3$ for cooling runs.*

For the polycrystalline $Sm_{0.6}Sr_{0.4}MnO_3$ the transition temperature T_c is 125K while T_p is 131K [43]. It was reported by Martin et al. [44] that a transition to charge ordering phase occurred at T_{CO} ~ 140 K. From the above mentioned, in different works, the transition temperature is not the same for $Sm_{0.6}Sr_{0.4}MnO_3$. The crystal structure which is obtained from different works is the same for $Sm_{0.6}Sr_{0.4}MnO_3$. The lattice constants are identical but the oxygen atoms occupy different positions as a result of the tilt of the octahedron. The magnetic and electronic transport occur via oxygen atoms which construct this octahedron. This may lead to the difference in T_c. Also, the coexistence of the ferromagnetic, the canted antiferromagnetic, the charge and the orbital ordering leads to the appearance of the multicritical phase diagram. Looking at the resistivity–temperature dependence in our case (cooling run), one can note the transition from insulator to metallic behavior at T~74 K (see Fig. 5.11). In the metallic state there are two transition temperatures at T~108Kand T~157 K. This may be attributed to the coexistence of charge and canted antiferromagnetic (weak ferromagnetic) ordering at 74 K> T < 108 K. The ferromagnetic ordering predominates at T > 157 K. Similar behavior was reported for $Sm_{0.5}Sr_{0.5}MnO_3$ where the coexisting correlations of the charge or

orbital ordering, ferromagnetic and layered-antiferromagnetic ordering were observed [44].

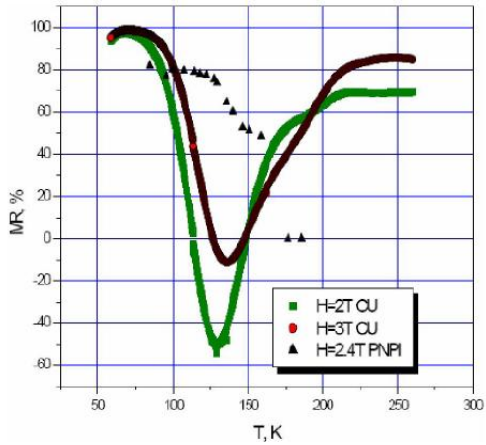

Fig. 5.11 *Magnetoresistance of $Sm_{0.6}Sr_{0.4}MnO_3$ at different applied magnetic fields.*

According to Abdel-Latif and El-Sherbini [4], in spite of both $Sm_{0.6}Sr_{0.4}MnO_3$ samples have the same structure (lattice constant are almost the same) and are prepared using the same method (solid state reaction) they have different MR values [1, 20] as shown in Fig. 5.21. The thermal treatment during preparation, are not the same which may lead to the difference in the tilt of MnO_6 octahedra and hence in the MR values. It is also well known that, the exchange interaction between Mn eg and O2p orbital is governed by the Mn-O1-Mn and Mn-O2-Mn angles which are the basic parameters in determining the magnetic and the electronic behavior of this compound. So we can conclude that the less distortion in the MnO6 octahedra in sample No. 1 (prepared in Cairo University [1]) leads to the increase in CMR value which became more than the corresponding value in sample No 2 (prepared in PNPI [20]).

The DC resistivity – temperature dependence measurements of $YbMnO_3$ is shown in Fig. 5.26. It is clear that as prepared sample has the semiconductor

behavior of this compound as well as the sample which fired at 750°C. Both have the semiconductor behavior but the difference only that as prepared sample has higher resistivity than that one fired at 750°C for 10h. The activation energy of (0.5742eV) of the sample as prepared is higher than the activation energy (0.255eV) of that sample fired at 750°C.

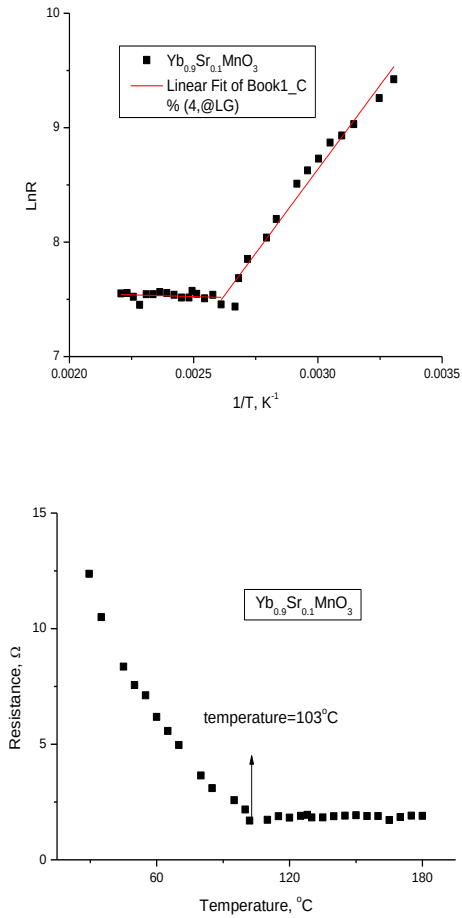

Fig. 5.12 *The DC resistivity – temperature dependence measurements of* $Yb_{0.9}Sr_{0.1}MnO_3$.

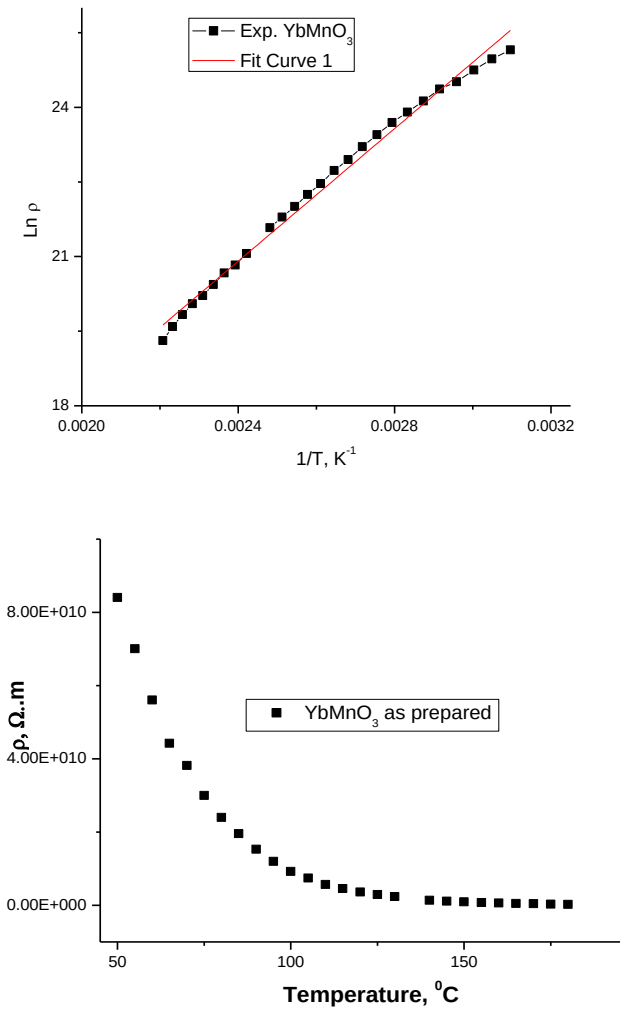

Fig. 5.13 *The DC resistivity – temperature dependence measurements of $YbMnO_3$ as prepared.*

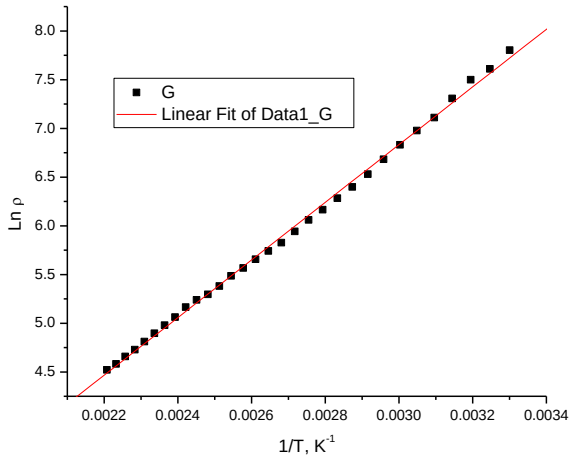

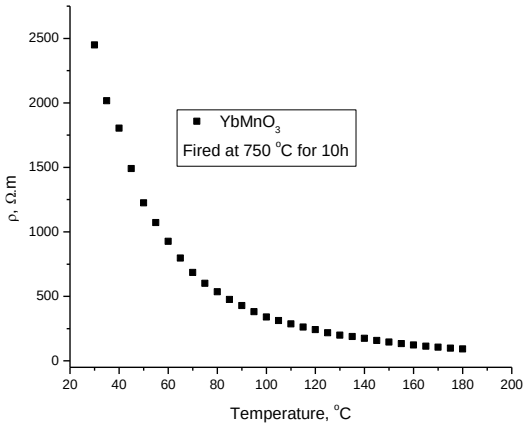

(b) at firing temperature 750 ℃

Fig. 5.14 *The DC resistivity – temperature dependence measurements of* $YbMnO_3$.

5.2 Magnetic Properties of 3d-4f Oxides

The temperature dependence of the magnetization curves of $SmFe_{1-x}Mn_xO_3$ under an applied field H=50 Oe is shown in Fig. 5.15 sad. A paramagnetic-to-weak-ferromagnetic transition with decreasing the temperature is observed for all samples. The corresponding transition temperature, i.e., the Curie temperature sTCd, monotonically decreases as the Mn content increases. It was reported 6 that the parent compound $SmFeO_3$ presents a spin reorientation sSRd at low temperatures Tk=433 Kd from weak-ferromagnetic sWFd ordering to antiferromagnetic sAFd ordering transition as the temperature decreases. The critical temperature sTkd corresponding to this WF–AF transition principally decreases except for the sample with x=0.1d as Fe ions are substituted by Mn ions. For the sample with x=0.3, the transition from WF to AF seems to be almost total with the magnetization less than 0.004 emu/g for T,T_k s=176 K. For the sample with x =0.2, the AF ordering is not totally established and it seems there is a competition between the WF and AF orderings below T_k=350 K since the magnetization is not totally vanished sM, 0.04 emu/g at Tkd. The sample with x=0.1, at first glance, seems to present the same behavior. However, one can observe from Fig. 5.12 sad the initiation of spin reorientation at about T_k=320 K and then WF takes over below 320 K. To explain the changes of these critical temperatures ~T_C and T_k, one has to consider the energies involved corresponding to possible interactions between different M_1–M_2 pairs M_1 and M_2 may be Fe ions or/and Mn ionsd. For the samples with x=0.2 and 0.3, The Mössbauer data show that the samples contain Fe^{3+} ions only, and the possible interactions are Fe^{3+}–Fe^{3+}, Fe^{3+}–Mn^{3+}, and Mn^{3+}–Mn^{3+} pairs. The interaction Fe^{3+}–Fe^{3+} is known to be antiferromagnetic. If we assume that the interaction Mn^{3+}–Mn^{3+} is ferromagnetic as was observed in $La_{1-x}A_xMnO_3$ A=Ca or Sr, the interaction Mn^{3+}–Fe^{3+} seems to be

antiferromagnetic since the AF ordering is well established as the Mn content increases. Moreover, this interaction may be weaker than that of Fe^{3+}–Fe^{3+} which may explain the decrease of *TC* as the Mn content increases. The increases of magnetization for *T*,*Tk* for the sample with *x* =0.1 may be due to the contribution from paramagnetic Sm^{3+} ions. However such contribution should also be expected for the two other samples with *x*=0.2 and 0.3, since the Sm^{3+} ions content was not changed and the interaction between iron smanganesed 3*d* electrons and samarium 4*f* electron ions is much weaker. The substitution of iron by manganese ions may generate different effective internal fields s*Hi*d acting on the central paramagnetic samarium ion leading to different magnetic contribution from Sm^{3+} ions. However the temperature dependence of the magnetizations of the samples with *x*=0.1 and 0.2 in an applied field of 13 kOe are almost identical, as shown in Fig. 5.11 sbd. This suggests that the variations observed in *Ms*T*d at 50 Oe are rather connected to the interactions of *M*1–*M*2 pairs. Unlike the samples with *x*=0.1 and 0.2, the AF magnetic ordering for the sample with *x*=0.3 seems to be not totally broken at 13 kOe. The existence of divalent ions Fe^{2+} - Fe^{2+} being Jahn–Teller ions orbitally frustrated in the sample with *x* =0.1, which yields necessary the presence of Mn^{4+} ions for the charge compensation, may lead to multiple and complex interactions of M_1–M_2 pairs with possibly the existence of ferromagnetic configurations ssuch as the ferromagnetic double-exchange interaction of Mn^{4+}–Mn^{3+} and Fe^{2+}–Fe^{3+}; the interaction Mn^{4+}–Fe^{3+} was demonstrated to be not strong12d that may explain the increase of magnetization at *T*,*Tk* for the sample with *x*=0.1. In addition, the Jahn–Teller effect of Fe^{2+} could be small in the sample with *x* = 0.1 which may reduce the AF coupling and enforce the ferromagnetic coupling. The existence of ferromagnetic ordering is confirmed by the coercivity for the sample with *x* =0.1 of H_c=195 Oe as compared to that of the

samples with x=0.2 and 0.3, with Hc=36 and 32 Oe, respectively. The shape of the hysteresis loop at T=113 K sT,Tkd for x=0.1 shows that the magnetization does not saturate up to an applied field of 13 kOe, with a characteristic slope $[M/]_H$ and slopes were taken in the linear variation of M with H, i.e., above H=5 kOe for all samplesd of 85 memu/g Oe. These features can be correlated to a strong AF interaction dominated by the interaction of Fe^{3+}–Fe^{3+} pairs. For the sample with x=0.2, the slope $[M/]_H$ is of 30 memu/g Oe, indicating that the AF coupling is weaker than that for x=0.1. This result suggests that the substitution of Fe ion by Mn ions weakens the AF coupling $M1$–$M2$ pairs and may be correlated to the weak AF interaction for Fe^{3+}–Mn^{3+}, as suggested above. The hysteresis loop of the sample with x=0.3 shows a similar shape as that for x=0.2 with a slightly greater slope, $[M/]_H$=40 memu/g Oe. However a substantial decrease in the magnetization sat 113 K and maximum field of 13 kOe is observed see Fig. 5.15. This result was expected since the magnetic moment of the free Fe^{3+} ion s5.9mBd is larger than that of Mn^{3+} s4.8mBd.13. The variation in the magnetic properties of $SmFe_{1-x}Mn_xO_3$ upon Mn ion content may also be correlated to the differences in the hybridization of the $t2g$ and O $2p$ electrons.

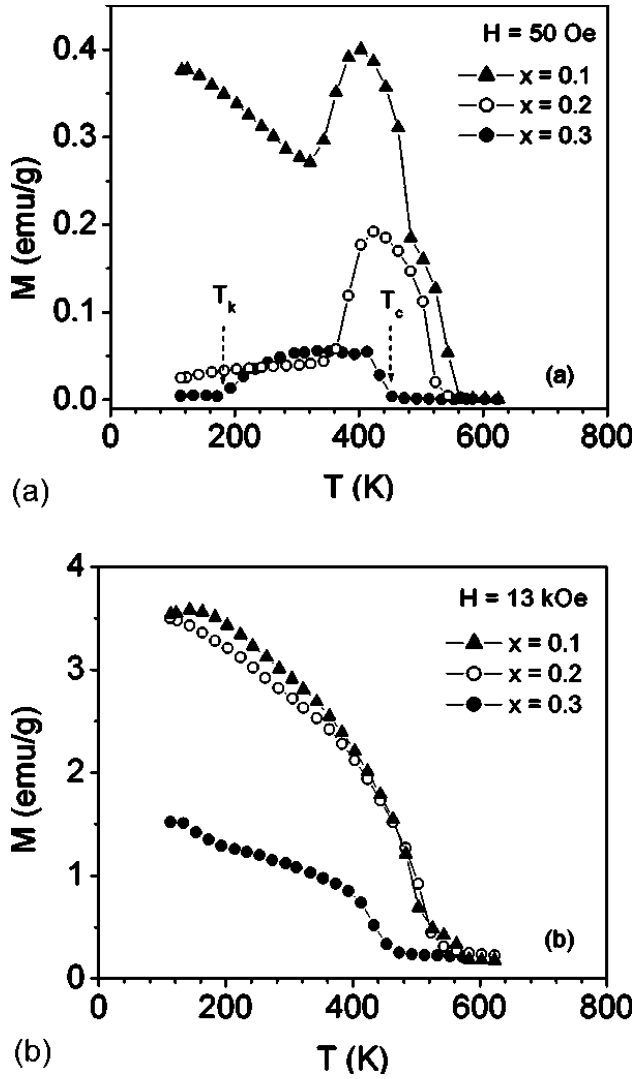

Fig. 5.15 *Temperature dependence of magnetization for the orthoferrites* $SmFe_{1-x}Mn_xO_3$ *(x=0.1, 0.2, and 0.3) in the applied fields of (a) 50 Oe and (b) 13 kOe.*

The resonant inelastic x-ray emission (RIXE) spectra have been measured at the Bach beamline at Elettra synchrotron radiation for the Mn3*d*-2*p*3/2 and also for Fe3*d*-2*p*3/2.

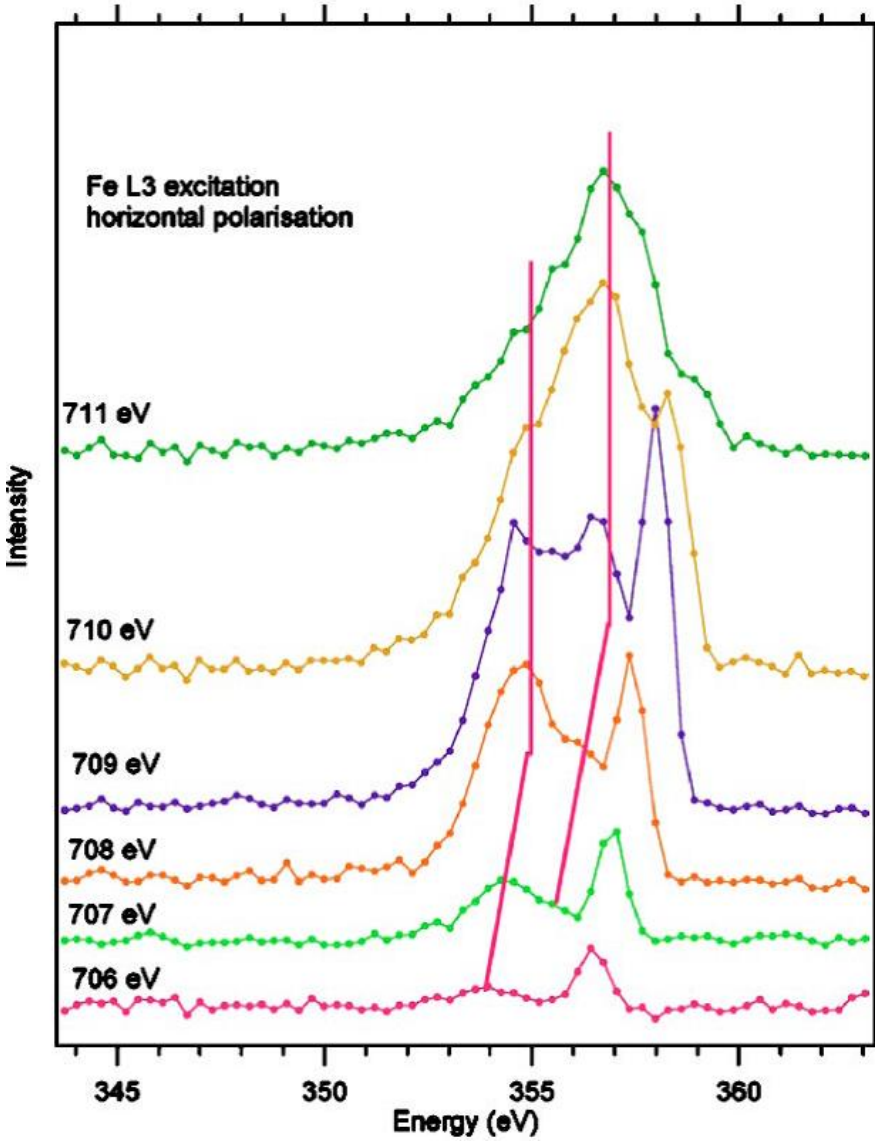

Fig. 5.16 *RIXE spectra of orthoferrite $SmFe_{0.7}Mn_{0.3}O_3$ at room temperature.*

Typical RIXE spectra at Fe *L*3 edges for orthoferrites $SmFe_{1-x}Mn_xO_3$ (x=0.3) are shown in Fig. 5.16. In all spectra, for both Fe and Mn thresholds, resonant and nonresonant features can be easily identified. The nonresonant features

appear at constant emission energy. These structures arise from photon excitation and subsequent x-ray emission and are possibly due to a process in which excitation and emission are incoherent. For instance, the onset of the Mn 2*p*3/2 3*d* excitation is located between 641.5 eV and 642 eV. Resonating inelastic loss features appear at constant energy loss with respect to the elastic peak. Two well-resolved inelastic emission peaks are observed at about 7 eV and at about 2.5 eV below the elastic peak. As for Fe emission, the onset of the Fe 2*p*3/2 excitation threshold is located between 709 and 710 eV. The electronic structure of iron in these compounds seems to be similar to Mn, because the inelastic emission peaks are observed at about 6 eV and at about 2.5 eV below the elastic peak, as is the case for the Mn resonant excitation. As reported in ref [11], Mössbauer data show that the samples contain Fe^{3+} ions only, and the possible interactions are Fe^{3+}–Fe^{3+}, Fe^{3+}–Mn^{3+}, and Mn^{3+}–Mn^{3+} pairs. The interaction Fe^{3+}–Fe^{3+} is known to be antiferromagnetic.

The multi-magnetic states appear either as a result of the inhomogeneity of the iron distributions in the next near neighboring [11, 12] or as a result of the coexistence of ferromagnetic and weak ferromagnetic ordering. The ferromagnetic ordering appears as a result of the Mn^{3+}-O-Mn^{4+} and Fe^{3+}-O-Mn^{3+} interactions, while the antiferromagnetic ordering as a result of Fe^{3+}-OFe^{3+} and Mn^{3+}-O-Mn^{3+} interactions. As a result of the competition between both the ferromagnetic and the antiferromagnetic ordering, the spin glass phase will appear [13-15]. So one can say that the coexistence of the ferromagnetic and weak ferromagnetic ordering is an indication for multi-magnetic states in such compounds while for the sample with x = 0.8 there is only weak ferromagnetic ordering with Curie temperature near 676 K. (See Fig. 5.15)

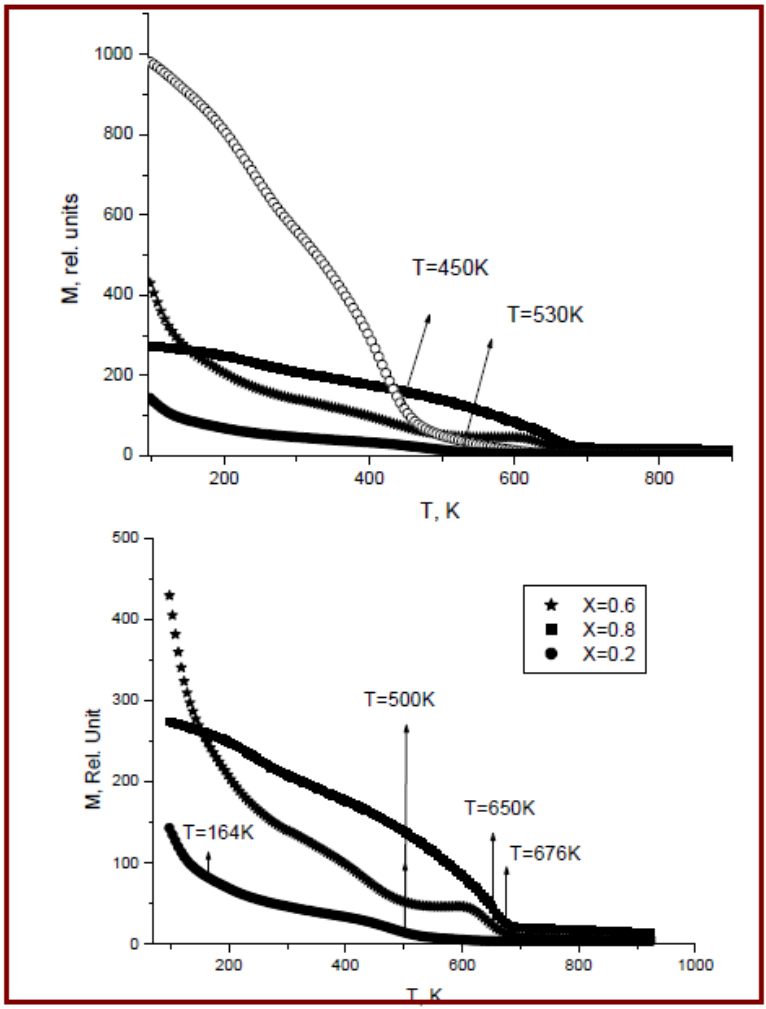

Fig. 5.17 *Magnetic susceptibility of the* $Nd_{0.65}Sr_{0.35}Mn_{1-x}Fe_xO_3$.

In fig. 5.17 we present the variations of the susceptibility with temperature. The figure reveals overall increase in magnetization as the Co contents increase. From the magnetization temperature dependence that is illustrated in Fig. 5.17, it is clear that for x = 0.2, 0.4 and 0.6 there are two phase transition points. These temperatures are indicated by arrows in Fig. 5.17. These results are in a good agreement with those obtained from neutron diffraction for x = 0.6,

where there are two phase transition points; the first transition from ferromagnetic into non-collinear ordering near 500 K and the second from non-collinear into paramagnetic phase near 660 K. According to the Mössbauer spectroscopy measurements at different temperatures for x = 0.4 and 0.6 samples the multi-magnetic states are confirmed [7].

The magnetization temperature dependence behavior of $Nd_{0.65}Sr_{0.35}Mn_{1-x}Fe_xO_3$ in the present case is in a good agreement with those reported for $La_{0.8}Sr_{0.2}Mn_{0.8}Ni_{0.2}O_3$ and $La_{0.7}Sr_{0.3}Mn_{0.8}Ni_{0.2}O_3$ [14], where the antiferromagnetic order is existed in addition to ferromagnetic order and the interaction between them leads to appearance of spin glass [14, 15]. The sample with x=0.0, the magnetization is very weak. The susceptibility shows a low temperature plateau that extends up to 10.5K, above which the susceptibility decreases rapidly to another plateau that extends to 140K. Moreover, the susceptibility shows a wide maximum that is centered around 40K.

As the Co-contents increase, the drop in the susceptibility seen at 140K develops to a sharp peak in x=0.3, and its position shifts to higher Tc (165K). For x=0.7 the peak occurs at 130K and for the Co-free sample, the peak is wide and centered around 175K. The possible magnetic states along with Tc and Co contents are given in Table 5.2.

Table 5.2. *Magnetic phases of* $Nd_{0.65}Sr_{0.35}Mn_{1-x}Fe_xO_3$.

Co-concentration	Tc (K)	Possible Magnetic state
0.0	140	FM (1) below 10K FM (2) between 10-140k
0.3	165	AF below 165
0.7	130	AF below 135
1.0	175	FM below 175

Mössbauer spectra at LN temperature show a superposition of a doublet and magnetic sub-spectra, with increase in the contribution of the latter as Fe

content increases. In the case of x=0.6 the ferromagnetic phase appear in LN temperature which in a good agreement with the neutron diffraction results given in ref. [24]. RT show dominant doublet spectra, but the magnetic sextet is more pronounced on the x=0.6 sample but in this case represent the non-collinear magnetic ordering. The distribution of the hyperfine fields reveals different configurations of Fe^{3+}.

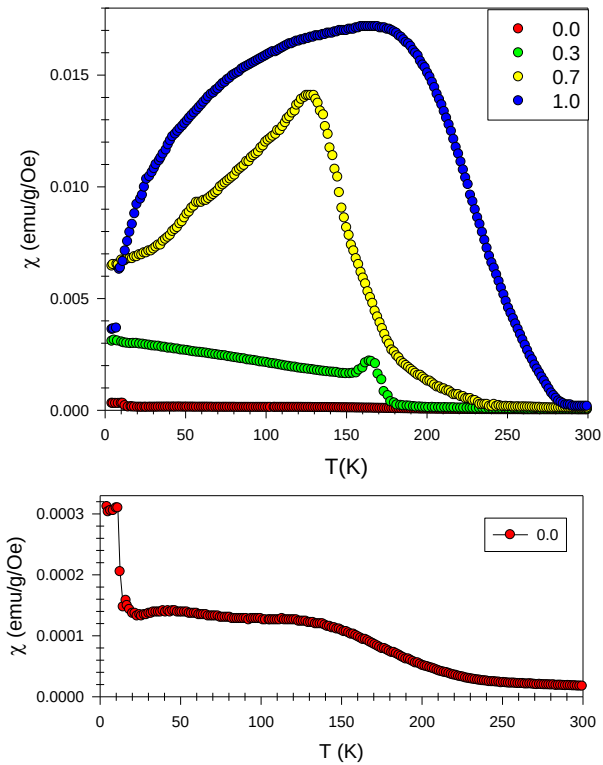

Fig. 5.18 *Magnetic susceptibility of* $Nd_{0.6}Sr_{0.4}\ Mn_xCo_{1-x}O_3$.

From neutron diffraction patterns of $Yb_{0.9}Sr_{0.1}MnO_3$ and $Yb_{0.6}Sr_{0.4}MnO_3$ reported in ref [21] and shown where the antiferromagnetic magnetic ordering is

clear because of the existence of magnetic peaks in these patterns which in good agreement with those works [46] reported before for similar compounds. Integrated intensity of magnetic peak (101) corresponding to antiferromagnetic ordering in hexagonal structure phase of both $Yb_{0.9}Sr_{0.1}MnO_3$ and $Yb_{0.6}Sr_{0.4}MnO_3$ are shown in Fig. 5.19. Mn atoms in the hexagonal structure are located at the center of the MnO_5 bipyramids and are linked by the corner-sharing equatorial oxygens. The displacement of each atom occurs when the temperature decreases below T_N and may lead to a tilt in the MnO_5. [47] From Fig. 5.19, Neil temperature T_N of $Yb_{0.9}Sr_{0.1}MnO_3$ near 87K and T_N of $Yb_{0.6}Sr_{0.4}MnO_3$ near 95K.

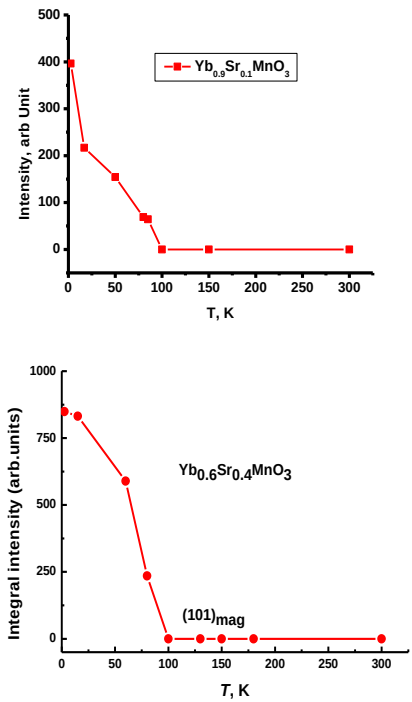

Fig. 5.19 *Integrated intensity of (101) representing antiferromagnetic ordering for $Yb_{0.9}Sr_{0.1}MnO_3$ and $Yb_{0.6}Sr_{0.4}MnO_3$ as a function of temperature.*

According to Capriotti *et al.*, [106-107] the relation between Neil temperature T_N and the nearest neighbor exchange integral J is given by the following formula;

$$T_N \approx 0.3J(S\text{-}1/2)^2$$

where S =2. The deduced values of the nearest neighbor exchange integral J for $Yb_{0.9}Sr_{0.1}MnO_3$ and $Yb_{0.6}Sr_{0.4}MnO_3$ are 11.1meV and 12.1meV, respectively. The DC resistivity – temperature dependence measurements (see Fig. 5.14) of $Yb_{0.9}Sr_{0.1}MnO_3$ showed decrease of resistivity with the increase of temperature which explains the semiconductor behavior of this compound at the temperature range from room temperature up to 103°C. It is noted also that there is transition at temperature t=103°C (or T=476K). From temperature of 103°C and up to 200°C the metallic behavior appeared. The coexistence of hexagonal and orthorhombic crystal systems may lead to the existence of antiferromagnetic and ferromagnetic magnetic ordering on the same for this composite. According to Fabreges et al [27] Néel temperature of $YbMnO_3$ is at T_N~80 K while the ferroelectric transition temperature is as high as T_c~900 K. The antiferromagnetic ordering is the predominant and at the temperature higher than 90K and one can explain the magnetic ordering diagram as follow; at the temperature lower than 90K the ferromagnetic phase will appear and a competition between them lead to a frustration of the net magnetic moment. So the super-paramagnetic semiconductor is the predominant on this temperature range. At the temperature equal to 476 K the metallic behavior is the predominant. The activation energy of first phase (the super-paramagnetic semiconductor) in $Yb_{0.9}Sr_{0.1}MnO_3$ has the value of 0.2527 eV while the activation energy of the second phase (the metallic) is 0.0014 eV.

The Mossbauer spectroscopy measurements were carried out for $SmFe_xMn_{1-x}O_3$ samples at room temperatures [11]. The experimental spectra

are shown in Fig. 5.20. All spectra are fitted using UNIVEM program [5]. The basic M ̈ossbauer parameters are given in Table 5.3. According to the isomer shift δ and quadrupole splitting $\_E_Q$ values, the iron ions in the present compounds are almost trivalent and occupy the octahedral sites [6].

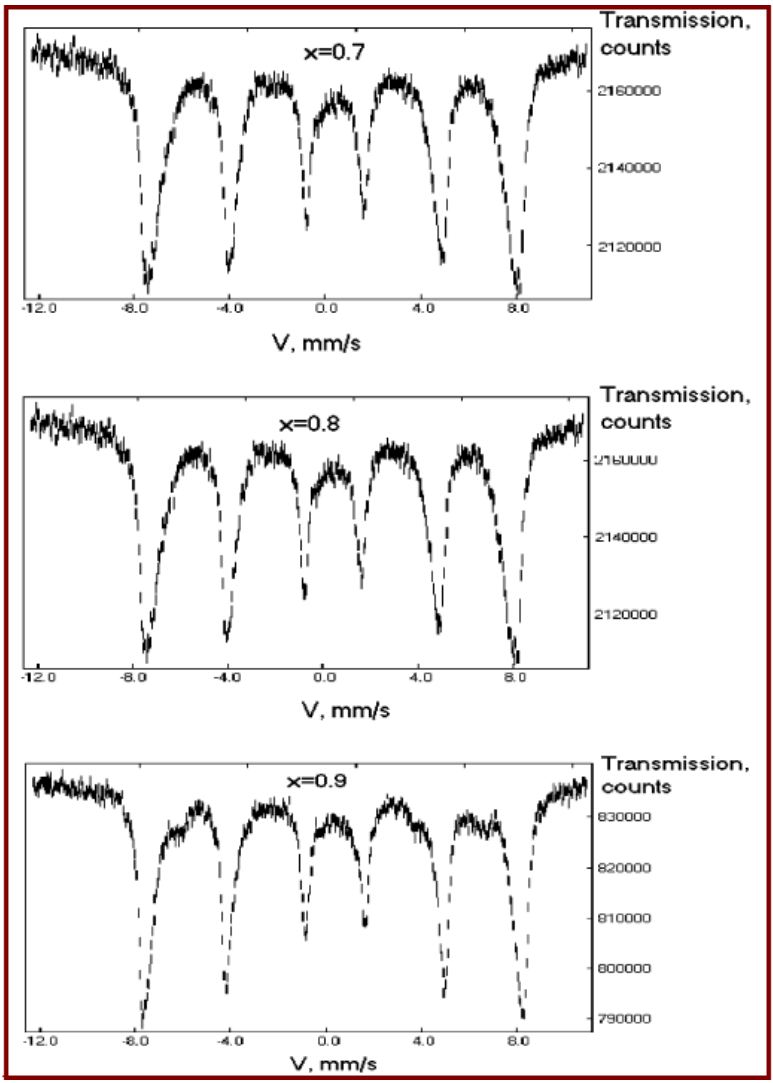

Fig. 5.20 *Mossbauer spectra of* $SmFe_xMn_{1-x}O_3$.

Table 5.3 *Mossbauer Parameters of $SmFe_xMn_{1-x}O_3$.*

Compound	C_i	δ (mm/s)	ΔE_Q (mm/s)	H(KOe)	S_{Exp} %	S_{cal} %
	C_1	0.38	-0.132	459	36	11.8
	C_2	0.37	-0.091	433	34	30.3
$SmFe_{0.7}Mn_{0.3}O_3$	C3	0.37	-0.091	404	22	32.4
	C_4	0.25	-0.029	371	7	18.5
	C_5	0.15	-0.460	294	1	6
	C_1	0.38	-0.121	487	39	26.2
	C_2	0.37	-0.090	465	35	39.3
$SmFe_{0.8}Mn_{0.2}O_3$	C3	0.37	-0.032	437	19	24.6
	C_4	0.25	-0.029	405	5	8.19
	C_5	0.21	-0.460	302	1	1.6
	C_1	0.36	-0.090	498	33	53.1
	C_2	0.36	-0.095	487	11	35.4
$SmFe_{0.9}Mn_{0.1}O_3$	C3	0.35	-0.083	475	31	9.8
	C_4	0.36	-0.080	452	8	1.5
	C_5	0.24	-0.043	405	17	0.1
$SmFeO_3$	C_1	0.54	-0.054	503	100	100

The results of the fitting of the experimental spectrum for $x = 0.7$ sample show that there are five magnetic sextets C_1–C_5. The isomer shift values of C_1–C_4 are close to each other and a good indication for the trivalent iron state while the isomer shift of C_5 are indicative of the divalent iron state [4]. The intensity of the latter sextet 1% is very small and one may neglect it. The quadrupole splitting values of C_1–C_4 show that the iron ions occupy the octahedral site. The hyperfine field Hin the first four sextets decreases systematically within decremental fields of $\_H \approx 29$ kOe (see Table 5.3). In similar way, for the sample with $x = 0.8$, the hyperfine field decreases within $\_H \approx 27$ kOe in the first four sextets and in the case of $x = 0.9$ sample the hyperfine field decreases in steps within $\_H \approx 17$ kOe in the C1–C4 sextets.

The nonrandom cation distribution model, proposed by Bashkirov et al. [7] is used in the present case to interpret the experimental spectra. This model is based

on the contribution of several magnetically split sextets forming the obtained spectra. Each one corresponds to a different iron concentration in the second coordination sphere. According to this model, the monotonic decrease in the hyperfine field is attributed to the decrease in the number of iron ions *n*(Fe) in the octahedral site, where *n*(Fe) takes values from 6 to 0. So from the above results, due to the replacement of iron ions by manganese in the next nearest neighbor (2^{nd} coordination sphere) various sextets were obtained. Every sextet has a hyperfine field that depends on the number of iron cations in the surrounding environments.

The probabilities of the various cation distributions *S*cal calculated using a binomial formula [4] are given in the 7^{th} column of Table 5.3. It is clear that the experimentally obtained probabilities *S* do not agree with *S*cal so that the distribution of iron ions in the octahedral sites is not governed by a random distribution. Such cations are formed together in nonrandom way and these results are in a good agreement with those for $NdFe_xMn_{1-x}O_3$ [8]. On the other hand, in Table 5.3 we included the Mossbauer parameters of $SmFeO_3$ [3]. From these parameters, it is clear that one sextet was obtained because there is only one probability that the Fe ions occupy the octahedral site surrounded by six Fe ions. The difference of hyperfine field (in the case of *n*(Fe) = 6) for $x = 0.9$, 0.8, 0.7 from the value of $x = 1$ may due to the effect of the 3rd coordination sphere that may also contain Mn ions. This value of Mn ions increases with decreasing the concentration of Fe cations.

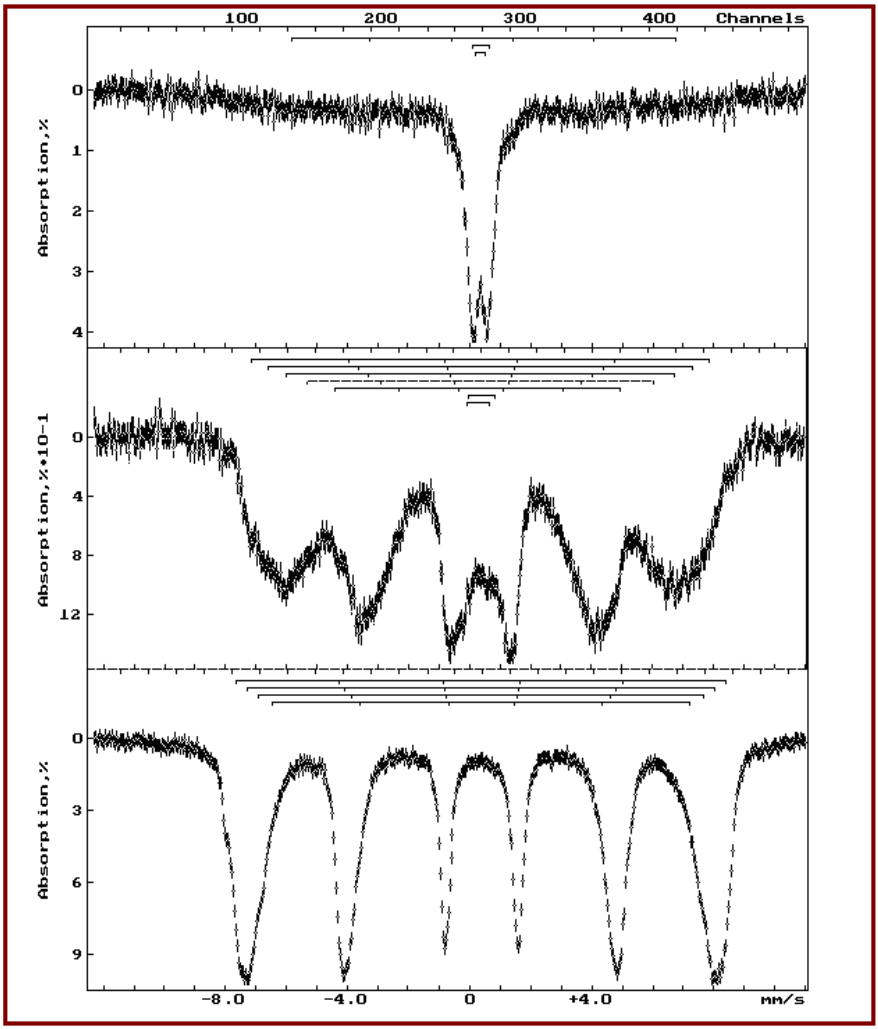

Fig. 5.21 *Mossbauer spectra of NdFex$Mn_{1-x}O_3$ (x=0.4, 0.6 and 0.8).*

Table 5.4 *Mossbauer parameters of $NdFe_xMn_{1-x}O_3$.*

Contents	**C_i**	**δ, мм/с**	**ΔE_Q, мм/с**	**H, кЭ**	**S, %**	**S_{cal}, %**	**n(Fe)**
$NdFe_{0,4}Mn_{0,6}O_3$	C_1	0,34	0,07	390	11	–	–
	C_2	0,36	0,56	–	58	–	–
	C_3	0,34	0,35	–	31	–	–
$NdFe_{0,6}Mn_{0,4}O_3$	C_1	0,37	-0,03	466	12	4,4	6
	C_2	0,36	-0,01	431	14	17,6	5
	C_3	0,36	-0,02	394	20	29,2	4
	C_4	0,37	-0,03	351	18	26,0	3
	C_5	0,32	-0,11	289	21	13,0	2
	C_6	0,39	0,88	–	10	–	–
	C_7	0,31	0,73	–	4	–	–
$NdFe_{0,8}Mn_{0,2}O_3$	C_1	0,38	-0,01	497	31	26,2	6
	C_2	0,38	0,00	475	33	39,3	5
	C_3	0,38	-0,01	451	24	24,6	4
	C_4	0,38	-0,02	423	12	8,1	3

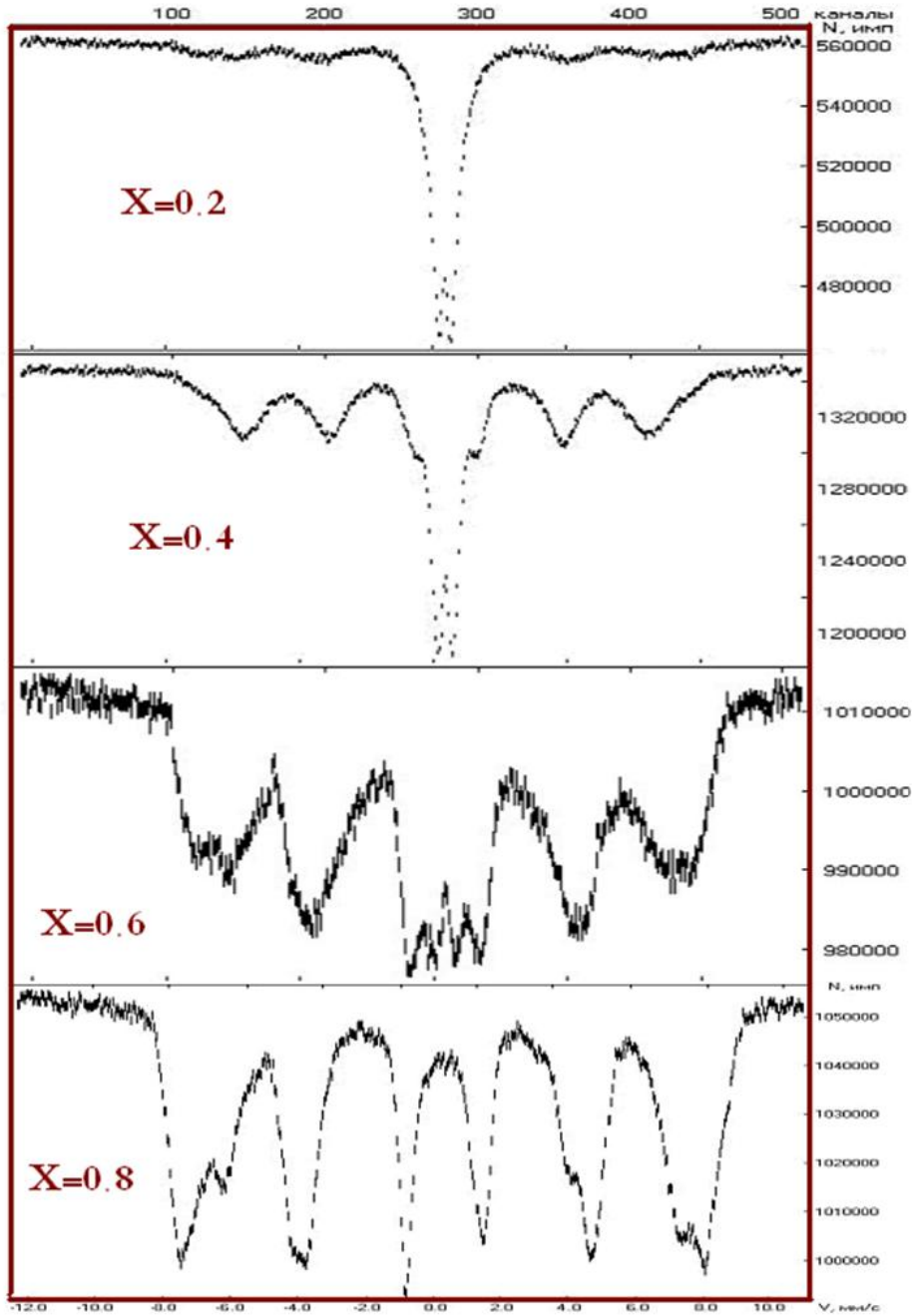

Fig. 5.22 *Mossbauer spectra of* $Nd_{0.65}Sr_{0.35}Fe_xMn_{1-x}O_3$ *(T=287K).*

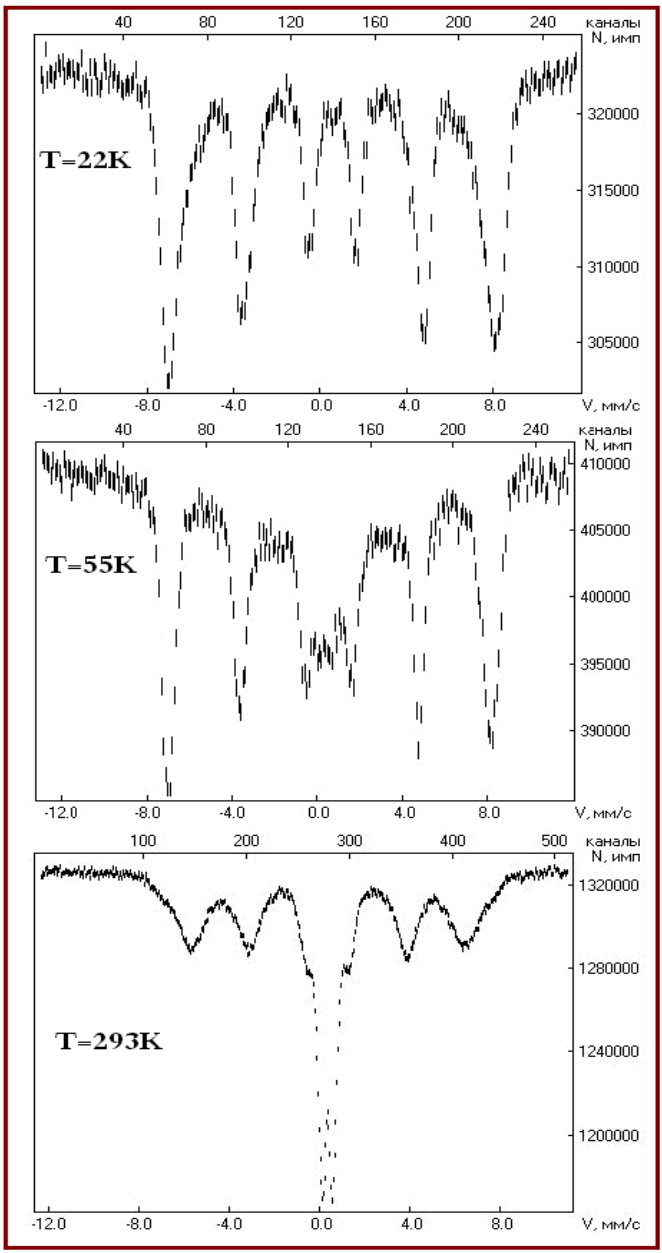

Fig. 5.23 *Mossbauer spectra of* $Nd_{0.65}Sr_{0.35}Fe_{0.4}Mn_{0.6}O_3$ *at different temperatures.*

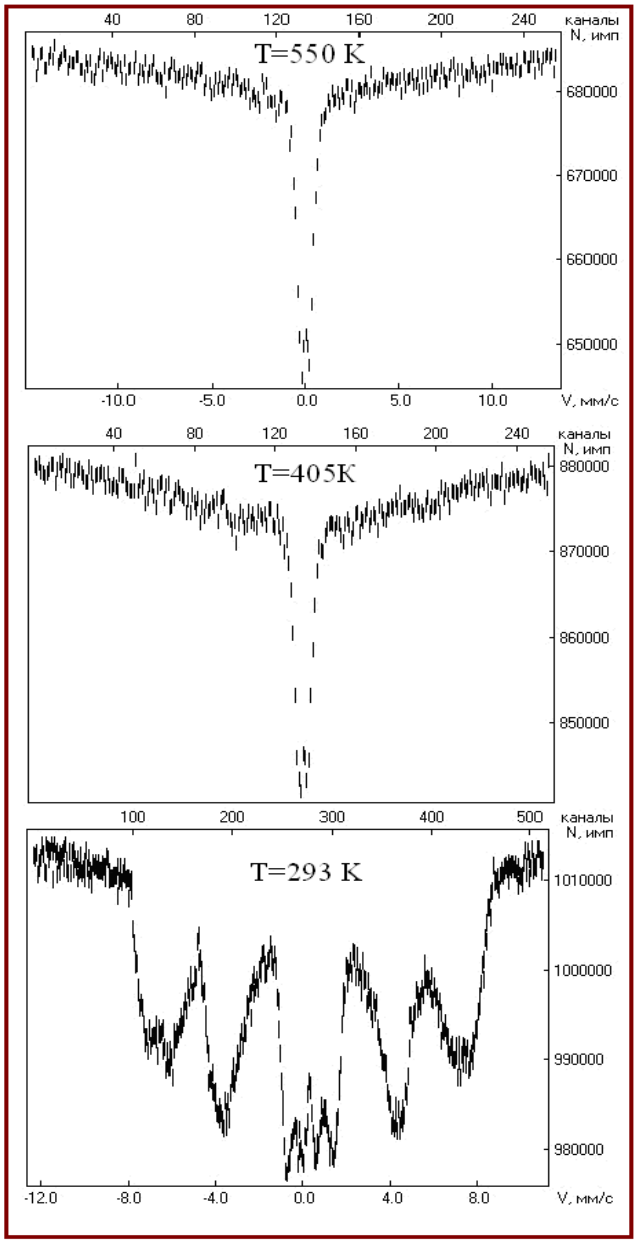

Fig. 5.24 *Mossbauer spectra of* $Nd_{0.65}Sr_{0.35}Fe_{0.6}Mn_{0.4}O_3$ *at different temperatures.*

Mössbauer spectra at LN temperature show a superposition of a doublet and magnetic sub-spectra, with increase in the contribution of the latter as Fe content increases. In the case of x=0.6 the ferromagnetic phase appear in LN temperature which in a good agreement with the neutron diffraction results given in ref. [24]. RT show dominant doublet spectra, but the magnetic sextet is more pronounced on the x=0.6 sample but in this case represent the non-collinear magnetic ordering. The distribution of the hyperfine fields reveals different configurations of Fe^{3+}.

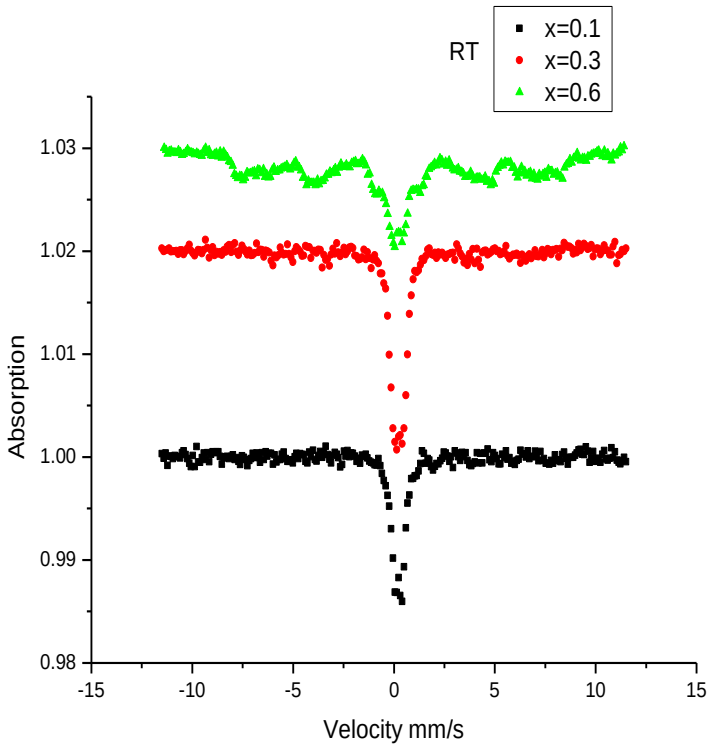

Fig. 5.25 *Mossbauer spectra of* $Nd_{0.65}Sr_{0.35}Fe_xMn_{1-x}O_3$ *at room (RT) temperatures.*

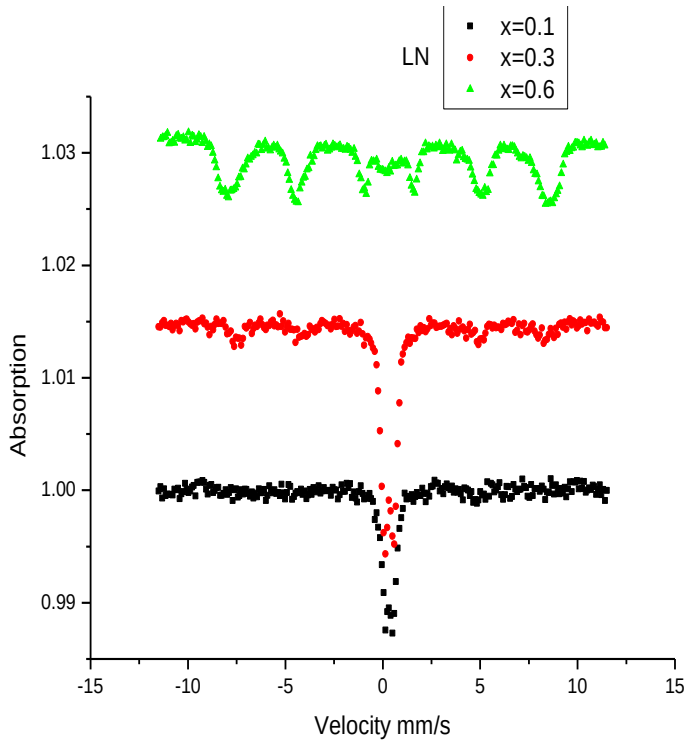

Fig. 5.26 *Mossbauer spectra of $Nd_{0.65}Sr_{0.35}Fe_xMn_{1-x}O_3$ at Liquid nitrogen (LN) temperatures.*

The magnetization measurements at 50 Oe show that the magnetic moment per unit volume as well as the Curie temperature increase with increasing Fe content. The magnetization at 13.5 kOe above T1=220K follow the same trend above. Interestingly, the trend is reversed below that temperature with the x=0.1 sample showing highest magnetization**.**

There is an indication of antiferromagnetic to ferromagnetic spin re-orientation below 200K (T2) in the x=0.1 sample only, but none observed for the x=0.3 or 0.6 samples.

Theoretical model for magnetisation and internal energy of $Eu_{0.65}Sr_{0.35}Fe_xMn_{1-x}O_3$

If we consider the manganese atoms have spin-up and when we dope the manganites with iron, Fe-ions substitute Mn-ions but with spin-down orientation causing antiferromagnetic ordering. With increasing the Fe doping the antiferromagnetic ordering increase and the ferromagnetic ordering decrease. Now we have two states, Mn-sites with a spin-up configuration and Fe-sites with a spin-down configuration.

The simplest theoretical description of that system is called the Ising model. The Ising model which is described earlier in [50] is a simple model of magnetism. The three-dimensional Ising model with two-states consists of N sites ($N = L^3$) where L is the number of sites for each dimension of the lattice. Because we are interested in the simulation of the three-dimensional Ising model for different temperatures and zero magnetic field, the Hamiltonian can be expressed in the form,

$$H = -\frac{J}{2}\sum_{<i,j>}^{N} S_i \,.\, S_j$$

Here, <I,j> refers to a sum over nearest neighbour pairs of atoms and S_i and S_j are the spin in i and i sites. Furthermore, J is called the exchange energy. The 1/2 is to avoid the double counting. The Hamiltonian of the Ising model with applied magnetic field, h, is given as follow;

$$H = -\frac{J}{2}\sum_{<i,j>}^{N} S_i.S_j - h\sum_{1}^{N} S_i$$

When we apply external magnetic field, the ordering of the spins increase, namely, the magnetization increase with increasing the applied external magnetic field.

The symmetry is broken at T_C so that the Monte Carlo simulations give one of the possible ground states and not an average of all of them, This model has been studied using MC simulations on 3d finite lattices with periodic boundary conditions (with size L^3 where L=12). All our simulations have made use of the Metropolis algorithm with averaging performed 10^5 Monte Carlo steps per site. Results were obtained by either cooling down from a high-temperature random configuration as discussed by Banavar *et al.* [51] or heating up from the ground state. The results from the two processes agree with each other.

The internal energy has ground state value equals to 6J/2 because each site has three nearest neighbours, where J is the exchange interaction which is equals to 1 for the antiferromagnetic interaction and to -1 for the ferromagnetic interaction. The internal energy curves continue stable until the transition temperatures, T_C, then, it goes down to an equal value for the whole doping. It is shown that the internal energy for x=0 is the highest value compared with the other x values which have nearly an equal ground state value, 2.7J. At a specific temperature, T=1 J/K, where K is the Boltzmann constant, the internal energy starts at high value at x=0, but it decreases with increasing Fe-doping, x to get its lowest value at x=0.2. The internal energy starts to increase again in the doping range $0.2<x<0.5$.

The ground state of magnetization value decreases with the increase of Fe-doping because the increasing of the spin-down with the increasing of Fe-doping. The magnetization as function of the temperature decreases with increasing of temperature in the range $1.0 > x > 0.5$, while it increase with increase of T for the range $0.5 > x > 0$, this is results because the Fe-content in

$Eu_{0.65}Sr_{0.35}Fe_xMn_{1-x}O_3$ becomes the dominant above x =0.5. We notice that the magnetisation at high-T does not go to zero as usual that is because the compound $Eu_{0.65}Sr_{0.35}Fe_xMn_{1-x}O_3$ always has residual some ordered spins which make the magnetisation has non zero values at high-T.

5.3 Dielectric Properties of 3d-4f Oxides

The dielectric constant ε' (real part) in the investigated system is contributed by several structural and microstructural factors. The real part of the materials was calculated by using the measured capacitance values and dimensions of the pellet by the following formula:

$$\varepsilon' = \frac{Cd}{\varepsilon_o A}$$

where C is the capacitance of the pellet in farad, d the thickness of the pellet in meters,

$$\varepsilon_o = 8.85x10^{-12} Fm^{-1},$$

is permittivity of free space and A is the cross-section area of the cylindrical pellet in m^2. The imaginary part of the dielectric constant ε'' was calculated using the relation: $\varepsilon'' = \acute{\varepsilon} \tan \delta$ where: $\tan \delta = \tan (90 - \phi)$, is the dispersion of the dielectric loss tangent. The plots of dielectric constant $\acute{\varepsilon}$ with frequency at room temperature for the system $Eu_{0.65}Sr_{0.35}Fe_{0.1}Mn_{0.9}O_3$ are shown in Fig. 5.27. A decrease in $\acute{\varepsilon}$ was observed with increase in frequency because at lower frequencies the compound exhibits different types of polarization (i.e. interfacial, dipolar, atomic, ionic and electronic). The observed variation can be explained on the basis of space charge polarization. At higher iron concentration (x = 0.5), the dielectric constant of the sample depends strongly on frequency. The $\acute{\varepsilon}$ decreases with increasing frequency. This shows that space charge polarization contributes more significantly to the

observed dielectric parameters in these compositions. The high value of $\acute{\varepsilon}$ observed in $Eu_{0.65}Sr_{0.35}Fe_xMn_{1-x}O_3$ system shows the ferroelectrics nature of the system. These values at low frequency may be due to voids, dislocations and other defects [43]. High dielectric constant decreases the penetration depth of the electromagnetic waves by increasing the skin effect. The frequency variation of loss tangent (tan δ) of $Eu_{0.65}Sr_{0.35}Fe_xMn_{1-x}O_3$ at room temperature shows that at relatively lower frequencies the values of tan δ is high and decreases rapidly with increasing frequency. The decrease of tan δ with increasing frequency is attributed to the fact that the hopping frequency of the charge carrier can not follow the changes of polarity of the external field beyond a certain frequency [43]. $\acute{\varepsilon}$ and saturated polarizations are dependent on grain size of the materials. However, SEM micrograph shows a granular structure with a dense morphology and little porosity can be seen, which offers much insulating grain boundary, leading to an increase in dielectric constant with decrease in grain size. Broadly speaking, these behaviors may be attributed to the reduced of grain size, compactness and the structural quality of the material.

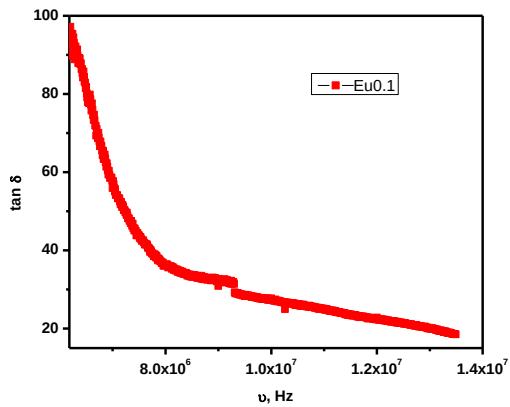

Fig. 5.27 *Dielectric constant ε with frequency at room temperature for the system* $Eu_{0.65}Sr_{0.35}Fe_{0.1}Mn_{0.9}O_3$.

Results show an increase of dielectric constants with increasing the iron content and a decrease with changing the measuring frequency at room temperature. This effect is attributed to the decrease in grain size, compactness and the structural quality of the specimen.

From above results it can be explained that the increase of σ_{ac} with temperature may be attributed to the increase in the drift mobility and hopping frequency of charge carriers with increasing temperature according to relation: $\sigma = ne\mu$, where e is the electronic charge and μ is the mobility of charge carriers and n is the total number of charge carriers per unit volume $n = n_e + n_h$, where e and h refer to the n- and p-type charge carriers, respectively.

The variation of electrical conductivity with frequency at different temperatures for $Nd_{0.6}Sr_{0.4}CoO_3$ as prepared is obviously shown in ref. [76] in which conductivity is increasing slowly at low frequency while increases strongly at high frequency. However, as the frequency increases the conductivity becomes more and more frequency dependent. Sharp drop in conductivity is observed at f = 4.5 MHz which is called the cutoff region. The very basic fact about ac conductivity in disordered solids is that σ_{ac} is an increasing function of frequency. In a hopping model, it is possible to distinguish different characteristic regions of frequencies [11, 12].

At low frequencies where the conductivity is constant, the transport takes place on infinite paths. For a region of frequencies where the conductivity increases strongly with frequency, the transport is dominated by contributions from hopping infinite clusters. Finally, the region where the high frequency cutoff starts to play a role is encountered. The electrical conduction mechanism can be explained in terms of the electron-hopping model. In other words, the conduction mechanism could be due to the electron hopping between two adjacent octahedral sites (B-sites) in the manganite lattice and a transition between $Co^{2+} \leftrightarrow Co^{3+}$ might

take place. Consequently, the increase in frequency enhances the hopping frequency of charge carriers resulting in an increase in the conduction process thereby increasing the conductivity. Further, at high frequencies, the resistivity remains invariant with frequency, because the hopping frequency no more follows the external field and thus lags behind it [13].

The disappearance of the conductivity peak during the decreasing temperature measurements can be attributed to the oxygen exhaustion from the sample during the heating cycle.

This variation in the conductivity may be caused by the oxygen exhaustion from the sample [92] The M-I transition behavior is observed at all frequencies, and the T_p is observed at 370 K at f = 50 Hz, it increases gradually with increasing frequency to reach 420 K at f =5 MHz.

In the case of low-mobility semiconductors such as ferrites, the activation energy is often associated with the mobility of charge carriers rather than their concentration. The charge carriers are considered as localized at the ions or vacant sites and conduction occurs via hopping-type process, which implies a thermally activated electronic mobility. ([100])

The activation energies for all samples at selected frequencies and below 400 K ($T<T_c$) are calculated. The calculated values of the activation energy are listed in Table 5.3. It can be seen that the activation energy decreases with increasing frequency for the studied ferrite which corresponding to ferrimagnetic region. In the ferromagnetic region, the activation energy for electric conduction decreases as the frequency increases corresponding to the thermally activated mobility (hopping conduction model) and not to thermally activated creation of charge carriers, while in the paramagnetic region of disordered state, the increase in frequency has no effect on the conductivity corresponding to thermally activated charge carriers (band conduction

mechanism). [5] The conduction at lower temperatures or below Curie temperature is due to hopping of electron between Fe^{2+} and Fe^{3+}, whereas at higher temperature or above Curie temperature is due to hopping of polarons. [16] Within the ferrimagnetic region of each sample, the activation energies of the prepared samples are found to be in the range 0.32344–0.2415 eV at 100 Hz, The values of E_f in the low frequency region are greater than 0.2 eV in present ceramics and suggests that conduction is due to hopping of charges [191].

6

Applications of Rare Earth Magnanites

Research devoted to rare earth manganites (3d-4f oxides) leads to a wide range of applications for example magnetic refrigeration (Environmentally friend technology) and spintronics. Magnetic refrigeration is a revolutionary, efficient, environmentally friend technology, which is on the threshold of commercialization.

6.1 Magnetic Refrigeration

One of Man daily need is environmentally friendly technology, which helps us to decrease pollutions in our world and keep our environment clean and safe. As well known using Freon refrigerators is one of the main sources which increases the Ozone hall and thus the harmful changes in climate. The progress in materials science allowed the appearance of new materials which can be used, in cooling system. Magnetic refrigeration is a cooling technology based on the magneto-caloric properties of these advanced materials to attain extremely low temperatures in ranges used in conventional refrigerators, depending on the design of the system [108]. These new materials are clean and environmentally friendly technology in order to reduce the harmful changing in the climate. From technological point of view, magnetic refrigeration is a revolutionary, efficient, environmentally friend technology, which is on the threshold of commercialization. Magnetic refrigeration was the first method developed to attain the temperature below about 0.3K (a temperature attainable by ^{3}He refrigeration that is pumping on the ^{3}He vapors) [108].

When a magnetic material is subjected to a sufficiently high magnetic field, the reorientation of magnetic moments is taken place as a result to this applied magnetic field. If the magnetic field is applied adiabatically, the raise of temperature of the material is obtained, and if the magnetic field is subsequently removed, the decrease in the temperature is observed. This warming and cooling which related to the application and removal of an external magnetic

field is so called the magneto-caloric effect 'MCE'. The basic idea of magnetic refrigeration is shown in fig. 6.1. When we apply a magnetic field on magneto-caloric material, for example Gadolinium alloy [108-110], thermodynamically process is occurred and resulting in the drastic decrease in temperature as we will see in details. The magneto-caloric effect can be mathematically represented in the following equation form, where ΔT is the change in temperature, ΔH is the change in applied magnetic field, C is the heat capacity of the working magnet (refrigerant), and M is the magnetization of the refrigerant: [1]

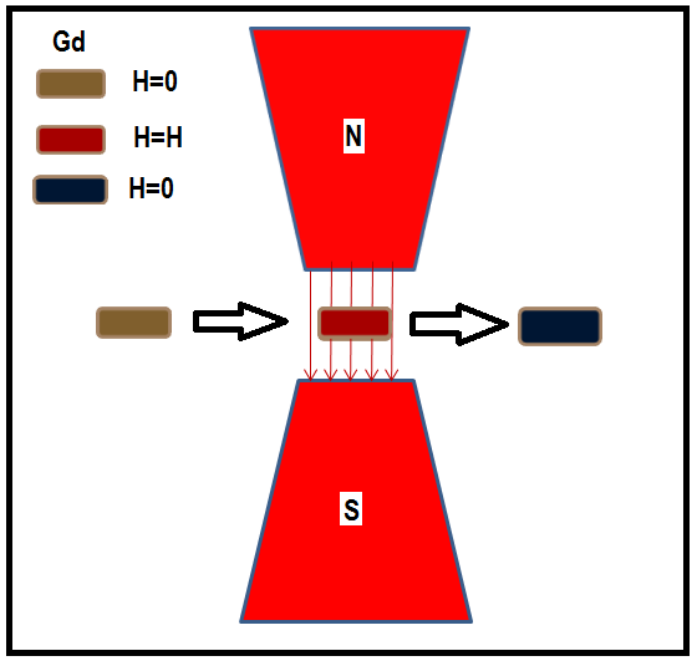

Fig. 6.1 *Gadolinium alloy inside the magnetic field and low temperature output.*

$$\Delta T_{ad} = -\int_0^{H_1} \left(\frac{T}{C(T,H)}\right)_H \left(\frac{\delta M(T,H)}{\delta T}\right) dH \qquad (1)$$

The change in magnetic entropy (ΔS_M) can be defined as the adiabatic change of temperature as a result of the application of the magnetic field. The isothermal entropy change is described by the following relation [4]:

$$\Delta S_M (T,H) = S_M(T,H) - S_M(T, 0) = \int_0^{H_{max}} (\frac{\delta M}{\delta T})_H \, dH \qquad (2)$$

where H_{max} is the maximum external field. ΔS_M can be approximated from magnetization measurements made at discrete field and temperature intervals according to the following relation [5]:

$$\Delta S_M = \sum_i \frac{M_i - M_{i+1}}{T_i - T_{i+1}} \Delta H_i \qquad (3)$$

where M_i and M_{i+1} are the magnetization values measured in a field H, at temperature T_i and T_{i+1}, respectively.

From the above equations one can say that magneto-caloric effect can be enhanced by [108]: applying a large magnetic field, a magnet with a small heat capacity and a magnet with a large change in magnetization vs. temperature, at a constant magnetic field.

THERMODYNAMIC CYCLE

The thermodynamic cycle is performed as a refrigeration cycle that is in analogous to the Carnot refrigeration cycle, where the magnetic refrigerator cycle depends on the increases and the decreases in magnetic field strength in instead of the increases and the decreases in pressure in which the Carnot refrigerator cycle depends [108]. Comparison between magnetic refrigeration and conventional refrigeration cycle is very important to evaluate the magnetic refrigeration and understand how magnetic refrigerator work. As is shown in schematic diagram in Fig. 6.2, there is an analogy between magnetic and conventional refrigeration cycle. [108]

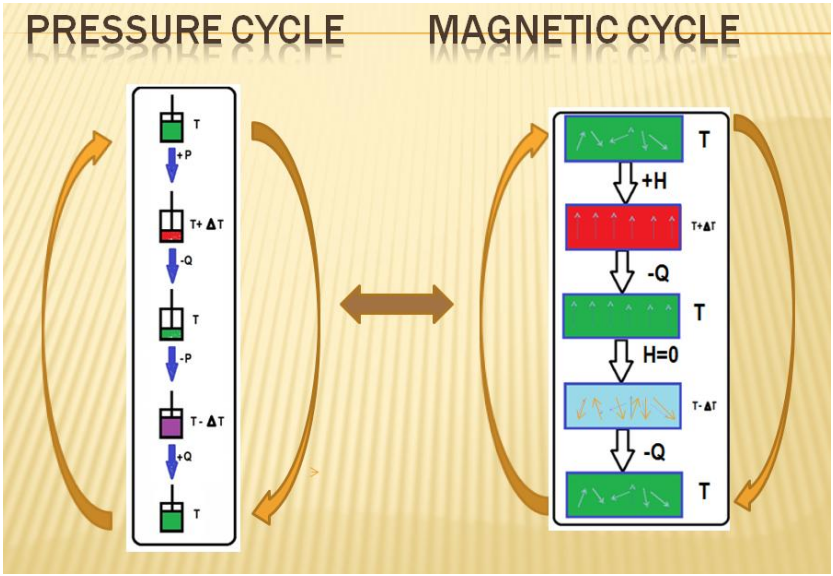

Fig. 6.2 *Conventional vapor refrigeration cycler and magnetic refrigeration cycle.*

In adiabatic magnetization, a magneto-caloric material is placed in an insulated environment, then, as a result of increasing an external magnetic field (+H) the magnetic moments are aligned in the direction which leads to increasing in the material temperature and decreasing in the magnetic entropy and heat capacity of substance. The total entropy does not change because there is no loss in energy and so heating up is observed ($T + \Delta T_{ad}$). [109-115]

For the conventional vapor refrigerator CVR cycle the gas is compressed by applying pressure P and similarly there is no loss in energy and so heating up is observed ($T + \Delta T_{ad}$). In isomagnetic enthalpic transfer: The added heat can then be removed (-Q) by a fluid or gas. To prevent the dipoles from reabsorbing the heat the magnetic field is kept constant and once sufficiently cooled, the magneto-caloric substance and the coolant are separated (H=0). In adiabatic demagnetization: In this stage the total entropy remains constant as a result to return to another adiabatic (insulated) condition. However, this time the decrease in magnetic field is obtained, the thermal energy leads to the magnetic

moments to overcome the field, and thus the sample cools, i.e., an adiabatic temperature change. Energy transfers from thermal entropy to magnetic entropy (as shown in Fig. 6.2, disorder of the magnetic dipoles is appeared). In isomagnetic entropic transfer: The magnetic field is kept constant to prevent the heating up again. Because of the difference in temperature according to our design, heat energy migrates into the working material (+Q). [116-120]

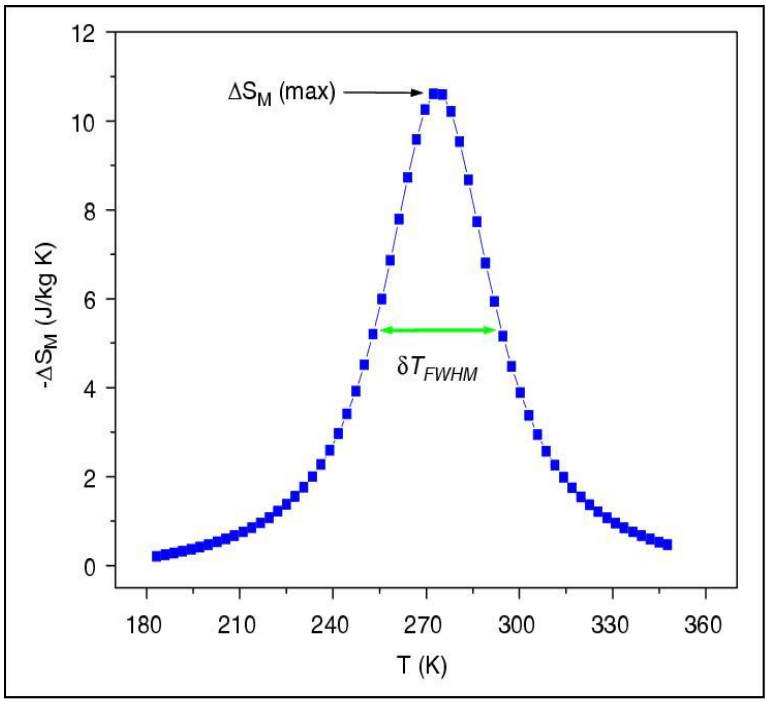

Fig. 6.3 *Magnetic entropy dependence on temperature [6].*

How to evaluate the relative cooling power RCP is an indication to the magnetic cooling efficiency [112] of the magneto-caloric material and it can be simply considered as the magnitude of ΔS_M or ΔT_{ad} multiplied by the full-width at half maximum (δT_{FWHM}) [110, 113]. ΔS_M, ΔT_{ad} and δT_{FWHM} are shown in Fig. 6.3 where the change in entropy is plotted as a function of temperature. The change in entropy could be deduced using equation 3 from

magnetization – temperature dependent measurements. On the time being the conventional vapor compression refrigerators are used for cooling applications; such as refrigerators and air conditioners AC. However, the low efficiency of the compressing and expanding processes of a gas in these refrigerators costs for 25% of residential and 15% of commercial power consumption [6]. In the conventional vapor compression refrigerators, the usage of gases such as chlorofluorocarbons (CFCs) and hydrochlorofluorocarbons (HCFCs) is dangerous because they damage our environment. Searching an alternative to the conventional gas compression (CGC) technique is very important issue to keep our environment safe and clean so that the development of new magnetic refrigeration (MR) technology, based upon the magneto-caloric effect (MCE) [114], has attracted the scientific interest. Now, the question is why MR is promising task for cooling technology. The answer is given in the Phan section in ref. [112] as following;

First, the cooling efficiency in MR is higher than CVR where the magnetic cooling efficiency can be reached up to 30-60% while the cooling efficiency in CVM according to a Carnot cycle is only 5-10%. Second, MR can be more compactly built by using solid substances as working materials and thus does not occupy big place. Third, the MR does not use any global-warming gases and therefore is an environmentally friendly cooling technology. Our main goals in the present proposal are introducing advanced and cheap materials with enhanced properties for cooling systems and developing a new generation of refrigerators and cooling systems environmentally friend to keep our environmental clean and safe.

The data of several typical magnetic materials that could be used in magnetic refrigeration are listed in table below in table 6.1 [121-127].

Table 6.1 *Typical magnetic parameters used for magnetic refrigeration.*

Sample	T_c (K)	$-\Delta S_{max}$ (J/KgK)	ΔH (T)	Reference of data
$La_{0.8}Ca_{0.2}MnO_3$	230	5.5	1.5	Ref [121]
$La_{0.67}Ca_{0.33}MnO_3$	267	6.4	3	Ref [122]
$La_{0.6}Ca_{0.4}MnO_3$	263	5.0	3	Ref [123]
$La_{0.65}Ca_{0.35}Mn_{0.9}Ti_{0.1}O_3$	103	1.3	3	Ref [123]
$La_{0.67}Sr_{0.33}Mn_{0.9}Cr_{0.1}O_3$	328	5.0	5	Ref [124]
$La_{0.87}Sr_{0.13}MnO_3$	197	7.5	8	Ref [125]
$La_{0.84}Sr_{0.16}MnO_3$	244	7.9	8	Ref [125]
Gd	294	4.2	1.5	Ref [121]
$Gd_{0.73}Dy_{0.27}$	265	10	5	Ref [126]
$Gd_5(Si_2Ge_2)$	276	14	2	Ref [127]
$Gd_5(Si_2Ge_2)$	300	7	5	Ref [127]

So the scientific efforts are devoted to get large (reasonable) magnetic entropy at or near room temperature. Different chemical formula is suggested. Large magnetic entropy change (ΔS_M~2.26J/Kg.K) at T_c=354K is observed by Mahn-Huong Phan et al [126] in $La_{0.6}Sr_{0.2}Ba_{0.2}MnO_3$ in magnetic field range from 0-10KOe. A large magnetocaloric effect in perovskites $(La_{1-x}Nd_x)_{0.7}Sr_{0.3}MnO_3$ at room temperature is reported by N. H. Luong et al. [127]. Magnetocaloric effect in Nd doped perovskite $La_{0.7-x}Nd_xBa_{0.3}MnO_3$ polycrystalline near room temperature was studied by Chen et al, [128]. The large ΔS_M was found in ref. [129] to occur around 300K for investigated manganese perovskites. The manganese perovskites in this work [129] have the large magnetic entropy changes induced by low magnetic field change, which is beneficial for the household application of active magnetic refrigerant (AMR) materials.

The mixed valance manganite perovskites are applied in ref [130] as magnetocaloric materials in a magnetic refrigeration device. The giant magnetocaloric effect with isothermal field-induced entropy change beyond the spin-multiplicity limit gave rise to some indistinctness regarding the

applicability of fundamental thermodynamics in data analysis is one of the important subject we found great number of research in the literature devoted to this subject. Those misleading interpretations concerning, for instance, the rigorousness of phenomenological thermodynamics are reported by Mukherjee et al., [131]. They showed that the Maxwell relation incorporates contributions from the spin degrees of freedom and potential lattice degrees of freedom into the isothermal entropy change. A minimalist model involving pairs of exchange-coupled, mobile Ising spins is investigated. It is explicitly shown that lattice degrees of freedom can be activated via applied magnetic fields and the integrated Maxwell relation contains this lattice contribution. A simple and intuitive analytic expression for the isothermal entropy change in the presence of field-activated lattice degrees of freedom is provided.

The electrocaloric effects accompanied with the ferroelectric to paraelectric phase transitions are investigated in ref [132] within the Landau–Devonshire theory. In this work they found that just changing the nature of the phase transition from the first-order to the second-order reduces the isothermal entropy change, adiabatic temperature change and refrigerant capacity. The isothermal entropy change in the second-order transition is reduced to one half of that in the first-order one, which is confirmed by experiments and is also consistent with the magnetocaloric counterpart.

Understanding the heat transfer phenomena taking place in the regenerator and the impact of the intrinsic properties of the magneto-caloric material will help us to optimize the performance of an active magnetic regenerative system [133]. Legait et al compared and tested three different materials ($Pr_{0.65}Sr_{0.35}MnO_3$, $La(FeCo)_{13-x}Si_x$, and gadolinium) using a permanent magnet based device. They concluded that even with a low δT_{ad}, the oxide $Pr_{0.65}Sr_{0.35}MnO_3$ can provide interesting results and they noted that the layered regenerator presents a better efficiency than the single layer. Moreover, a high

thermal conductivity material allows a great temperature span at high frequency to be obtained. The shape of sample they used in this work and isothermal entropy change in a 1 T field of LaFeCoSi are shown in Fig. 6.4 and Fig. 6.5.

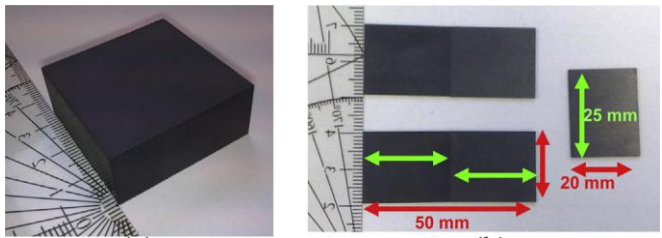

Fig. 6.4 *(a) A block of $Pr_{0.65}Sr_{0.35}MnO_3$ (b) Oxide plates with their dimensions after cutting [72].*

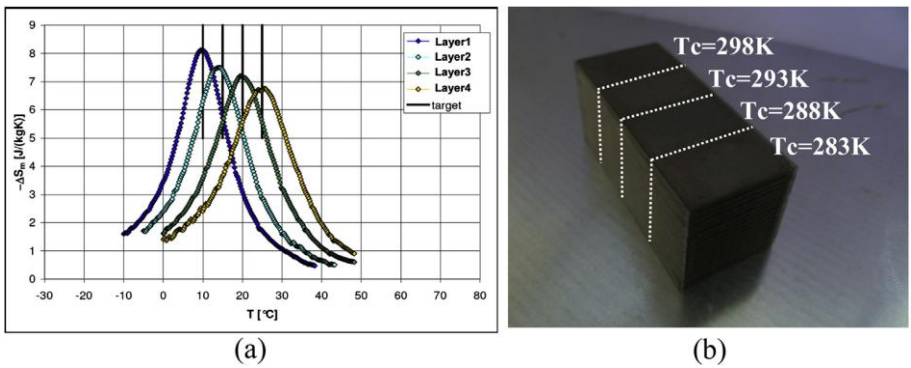

Fig. 6.5 *(a) Isothermal entropy change in a 1 T field variation of the four compounds of LaFeCoSi,. (b) LaFeCoSi regenerator with four different compounds [72].*

Looking at the recent research one can found that there is ongoing work on developing new materials that are both cost effective and operate in the temperature range of normal refrigeration. A giant magnetocaloric effect induced by sodium-deficiency in a Lanthanum manganites polycrystalline is recently reported by Wali et al., [134] where they found that the ability to tune the temperature transition close to room temperature is revealed to be possible by changing the sodium-deficiency content. The most important results in this work

are that a second-order magnetic phase transition from the ferromagnetic to the paramagnetic state at the Curie temperature (T_c) was found to be decreased from 335 to 260 K when the sodium deficiency rate increased. The change in the magnetic entropy increased from 2.38 J kg^{-1} K^{-1} to 3.48 J kg^{-1} K^{-1} under a magnetic field of 2 T when x increased from 0.00 to 0.15. Comparing the values obtained by Wali et al [135] and the values reported before underlines that the proposed oxide material has substantial advantages for magnetic refrigeration. Magnetic, specific heat and magnetocaloric studies have been carried out by Kalipada Das, Tapas Paramanik and I. Das [136] on rare earth calcium manganites; $Ln_{0.5}Ca_{0.5}MnO_3$ (Ln=Gd, Dy). They observed that the isothermal magnetic entropy change is fairly large at low temperature which is attributed to the magnetic precursor effect of rare-earth ions. The impact of the disorder on the magnetocaloric effect in Ti doped manganites was investigated by El. Kossi et al [136] where they found that the magnetic entropy change strongly depends on the Ti concentration. The most promising results are observed by I. A. Abdel-Latif et al., [137] where the $Nd_{0.6}Sr_{0.4}MnO_3$ nanocomposites showed MR of 99.84% at room temperature that makes it is possible to use these materials in fabrication of magnetic devices in the industrial scale.

Theoretical calculations will help us to design new materials with desired properties. Spin-dimer systems are a versatile playground for quantum phase transitions studies by using the magnetic field as the tuning parameter. According to the study of Straßel [138] it is possible to observe a crossover from the characteristic scaling near critical points to the behavior of a finite-temperature phase transition. In this work they studied two-dimensional coupled spin-dimer systems. Moreover, they found that the magnetocaloric behavior of the magnetization with temperature can be used to determine the critical fields with high accuracy. Gharsallah et al studied the magneto caloric effect for

$La_{0.6}Sr_{0.4}MnO_3$ and $La_{0.6}Ca_{0.4}MnO_3$ using theoretical calculations [139-140] which showed large and tunable suggesting their possible applications in moderate magnetic field and near room temperature.

It is quit clear that still great interest and effort that are devoted to studying the magnetocaloric effect in order to develop clean, cheap and environmentally friend refrigerator technology. The main challenge in the current magnetic cooling is that efficiency of cooling needs high magnetic field which is out of use in the industrial scale and very low temperature. So this work is a try to develop magnetic refrigerator materials with reasonable conditions for environmentally friend refrigeration based on the success of our recent work [137] and [134-135].

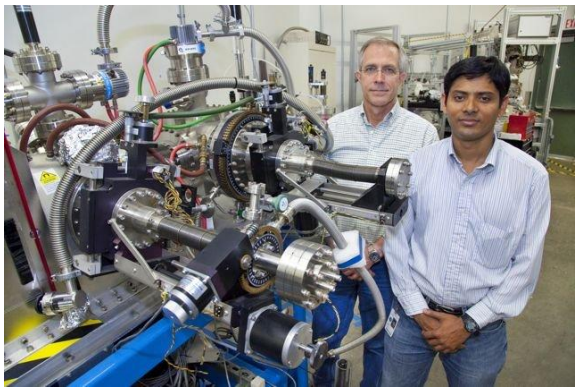

Fig. 6.6 *The Berkeley Lab prototype of magnetic refrigerator.*

(http://www.gizmag.com/giant-magnetocaloric-effect-in-fridges/15624/) [141]

The *Berkeley Lab research* was recently published in the journal *Physical Review* (http://www.gizmag.com/giant-magnetocaloric-effect-in-fridges/15624/) [142]

The magnetic rare earth materials are utilized as the magnetic refrigerants in most cooling devices. Recently, some data on the magnetocaloric effect in hole-doped manganites are reviewed. It is shown that the variation of interaction exchange energy, taking place under the effect of a magnetic field in the vicinity

of the phase transformation, provides a significant contribution to the change of magnetic entropy. Essebti Dhahri et al., reported [143] that different results found for electron-doped manganites $La_{1-x}Ce_xMnO_3$ (x = 0.3, 0.4 and 0.5). These manganites present a large magnetic entropy change induced by low magnetic change, which is beneficial for the household application of active magnetic refrigerant materials. It is believed that the manganite materials with the superior magnetocaloric properties in addition to cheap materials-processing cost will be the option of future magnetic refrigeration technology. So this very important application for perovskite will be one of the future works. Our plan is to synthesize different compounds with different nano-crystalline sizes and study magnetocaloric properties of the proposed compounds.

6.2 Magnetoresistive Random Access Memory (MRAM)

MRAM is a random access memory (RAM) technology (based on Spintronics) that uses electron spin to store information. MRAM has been called "the ideal memory", potentially combining the density of DRAM with the speed of SRAM and non-volatility of FLASH memory or hard disk, and all this while consuming a very low amount of power [144-146]. MRAM can resist high radiation, and can operate in extreme temperature conditions, very suited for military and space applications.

Transistors and other components with nanoscale dimensions, processors and memories are becoming so dense that even their infinitesimal individual currents are combining to produce scorching heat. Furthermore, quantum effects that were negligible before are now so pronounced that they're threatening to render circuits inoperable. The upshot is that we're fast approaching the point when moving charge is not going to be enough to keep Moore's Law chugging along.

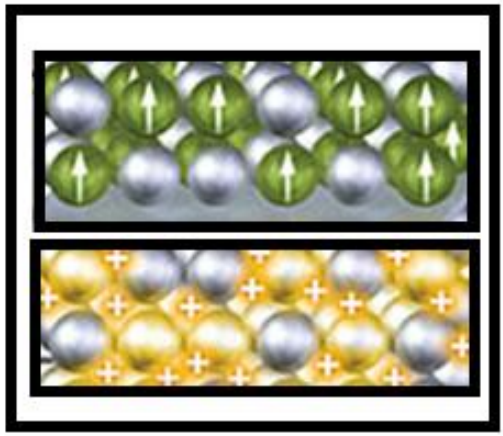

Fig. 6.7 *How a spin memory works (http://spectrum.ieee.org/image/MTcxODEyNg).*

In anticipation of that day, researchers all over the world are already working on a promising alternative. We have set our sights on a different property of electrons, which we hope to exploit for storing and processing data. This property is spin.

Spin is a fundamental yet elusive quantum attribute of electrons and other subatomic particles. It is often considered as a bizarre form of nano world angular momentum, and it underlies permanent magnetism. What makes spin interesting for electronics is that it can assume two states relative to a magnetic field, typically referred to as spin up or spin down. In other words you can use these two states to represent the two values of binary logic—to store a bit.

The development of spin-based electronics, or spintronics, promises to open up remarkable possibilities in the field of electronics. In principle, manipulating spin is faster and requires far less energy than pushing charge around, moreover it can take place at smaller scales. Chips built out of spin transistors would be faster and more powerful than traditional ones and, farther down the road, may feature such new and remarkable properties as the ability to change their logic functions on the fly. It is still decades away from being able to build such a

thing. But chips that exploit spin in a more modest way are already available. At least one company is now selling magnetoresistive random access memory, or MRAM, a kind of spintronic memory. And many others—including Free scale, Honeywell, IBM, Infineon, Micron, and Toshiba, as well as start-ups and university research groups—are busy investigating MRAM technology. The reason for all this interest is clear. Today's computers often use four kinds of storage. Dynamic random access memory, or DRAM, has high density but needs to be constantly refreshed and in addition to consuming lots of power. Static random access memory, or SRAM is used in caches. It is fast to read and write but from another side it takes up considerable space on a chip. Flash, unlike SRAM and DRAM, is nonvolatile but is quite slow to write to. And then there are hard disk drives; these have high density but rely on moving parts, which impose size and speed limitations. MRAM is attractive because it could, in principle, replace all other kinds of memory.

Rather than representing a bit as charge in a capacitor or as the state of an interconnected set of transistors, MRAM stores data using the spin of electrons in a ferromagnetic substance by creating a magnetic alignment in one direction or the other. In a tiny region of that material, spin up ↑ means 0, and spin down ↓ means 1. Proponents say that as MRAM improves, it could combine all the advantages of SRAM, DRAM, flash, and hard disks—with none of their shortcomings. MRAM would be a compact, speedy, low-power, and nonvolatile "universal memory." Using MRAM, a computer wouldn't have to juggle data between main memory, cache, and disk; instead, it could load all data into its working memory. This capability would change the way we think about computer architecture because it makes possible instant-on.

The challenge at the moment is that MRAM suffers from two problems: The density of bits is low, and the cost of chips is high. The early MRAM designs needed lots of current to change a 1 to a 0 or vice versa. This requirement

prevented their further miniaturization. Improved designs might overcome that hurdle using novel techniques and materials, but they would operate at only liquid-nitrogen temperatures. This is not going to work for your PC. This problem—the need for cryogenic temperatures to reduce the write current of MRAM—has been under the focus of the research. It's a major challenge, but there is hope to significant breakthrough. Recently, a device that shows potential as an MRAM memory cell was demonstrated. We can write using conventional voltage levels and almost no current at all. The key is a material called gallium manganese nitride, a semiconductor whose magnetic properties we can manipulate electrically. And here's the best part: It works at room temperature. Typical “classic” or “conventional” MRAM uses spin-dependent tunnel junction memory cells and magnetic row and column write lines.

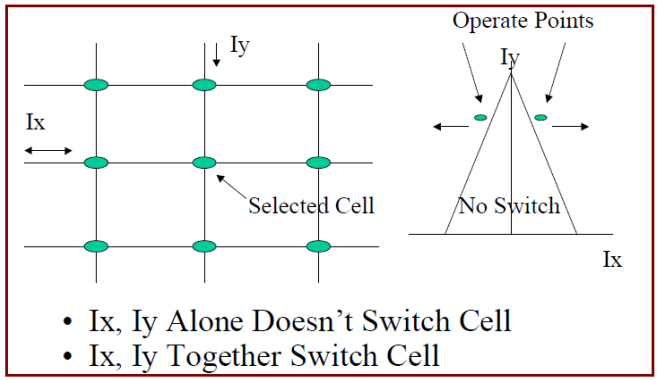

Fig. 6.8 *Magnetic Memory Cell Array.*

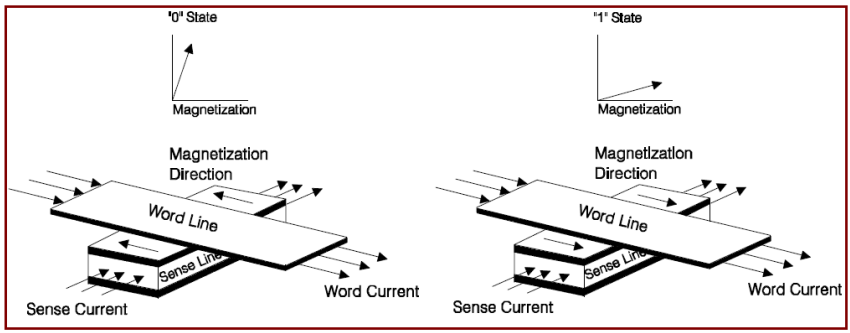

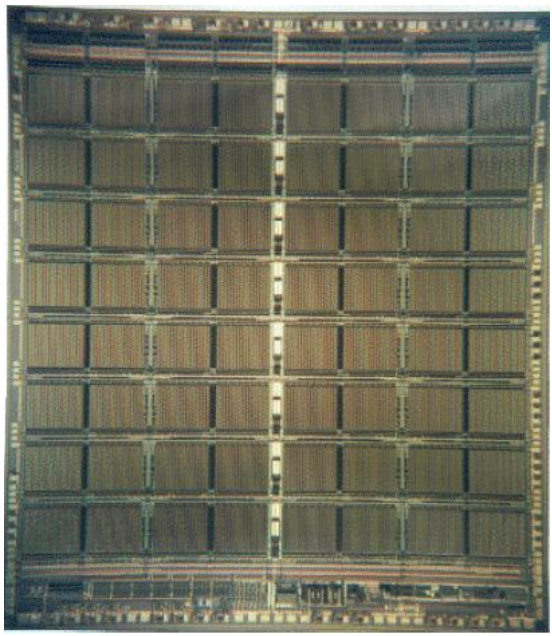

Fig. 6.9 *MRAM memory cell.*

The spin-dependent tunnel junction produces a large change in resistance depending on the predominant electron spin in a storage layer. The tunnel barrier is as thin as a few atomic layers--so thin that electrons can "tunnel" through the normally insulating material, causing a resistance change. Row and column magnetic write lines allow data to be written to a selected cell in a two-dimensional array.

Data are written by small electrical currents in the write lines that create magnetic fields, which flip electron spins in the spin-dependent tunnel junction storage layer, thus changing the junction's resistance. Data is read by the tunneling current or resistance through the tunnel junction.

Next-generation MRAM could reduce cell size and power consumption. Potential next-generation designs include Spin-Momentum Transfer, Magneto-Thermal MRAM, and Vertical Transport MRAM. Spin-Momentum

Transfer (also “Spin-Transfer,” “Spin Injection,” or “Spin Torque Transfer”) MRAM is based on changing the spin of storage electrons directly with an electrical current rather than an induced magnetic field. This method has the potential to significantly reduce MRAM write currents, especially with lithographic feature sizes less than 100 nanometers. M-T MRAM uses a combination of magnetic fields and ultra-fast heating from electrical current pulses to reduce the energy required to write data. Vertical Transport MRAM (VMRAM) is a high-density type of MRAM that employs current perpendicular to the plane to switch spintronic memory elements.

6.3 Magnetic Sensor

The earliest magnetic field detectors allowed navigation over trackless oceans by sensing the Earth's magnetic poles. Magnetic field sensing has vastly expanded as industry has adapted a variety of magnetic sensors to detect the presence, strength, or direction of magnetic fields not only from the Earth, but also from permanent magnets, magnetized soft magnets, vehicle disturbances, brain wave activity, and fields generated from electric currents. Magnetic sensors can measure these properties without physical contact and have become the eyes of many industrial and navigation control systems. This paper will describe the current state of several methods of magnetic sensing and how the sensors are used—many with integrated functions. Finally, several applications will be presented for magnetic sensing in systems.

Magnetic sensors have been in use for well over 2,000 years. Early applications were for direction finding, or navigation. Today, magnetic sensors are still a primary means of navigation but many more uses have evolved. The technology for sensing magnetic fields has also evolved driven by the need for improved sensitivity, smaller size, and compatibility with electronic systems. This paper will overview various types of magnetic sensors and their

applications. It is not intended as a how-to description of building sensor systems but more of what is this sensor and how does it detect magnetic fields. The newest types of silicon based magnetic sensors will be emphasized—anisotropic magnetoresistive (AMR) and giant magnetoresistive (GMR) sensors. Applications for AMR and GMR magnetic sensors are presented.

A unique aspect of using magnetic sensors is that measuring magnetic fields is usually not the primary intent. Another parameter is usually desired such as wheel speed, presence of a magnetic ink, vehicle detection, or heading determination. These parameters cannot be measured directly, but can be extracted from Figure 6.8. Conventional vs. Magnetic Sensing changes, or disturbances, in magnetic fields. Scheme 6.1 shows other sensors, such as temperature, pressure, strain, or light that can be detected using an appropriate sensor. The output of these sensors will directly report the desired parameter. On the other hand, using magnetic sensors to detect direction, presence, rotation, angle, or electrical currents only indirectly detect these parameters. First, the enacting input has to create, or modify, a magnetic field. A current in a wire, a permanent magnet, or sensing the Earth's magnetic field can create this field. Once the sensor detects that field, or change to a field, the output signal requires some signal processing to translate the sensor output into the desired parameter value. This makes magnetic sensing a little more difficult to apply in most applications, but it also allows for reliable and accurate sensing of parameters that are difficult to sense otherwise. One way to classify the various magnetic sensors is by the field sensing range. These sensors can be arbitrarily divided into three categories—low field, medium field, and high field sensing. Sensors that detect magnetic fields less than 1 microgauss will be classed low field sensors. Sensors with a range of 1 microgauss to 10 gauss will be considered Earth’s field sensors and sensors that detect fields above 10 gauss will be considered bias

magnet field sensors for this paper. In scheme 6.1 the various sensor technologies are listed and illustrates the magnetic field sensing ranges [1].

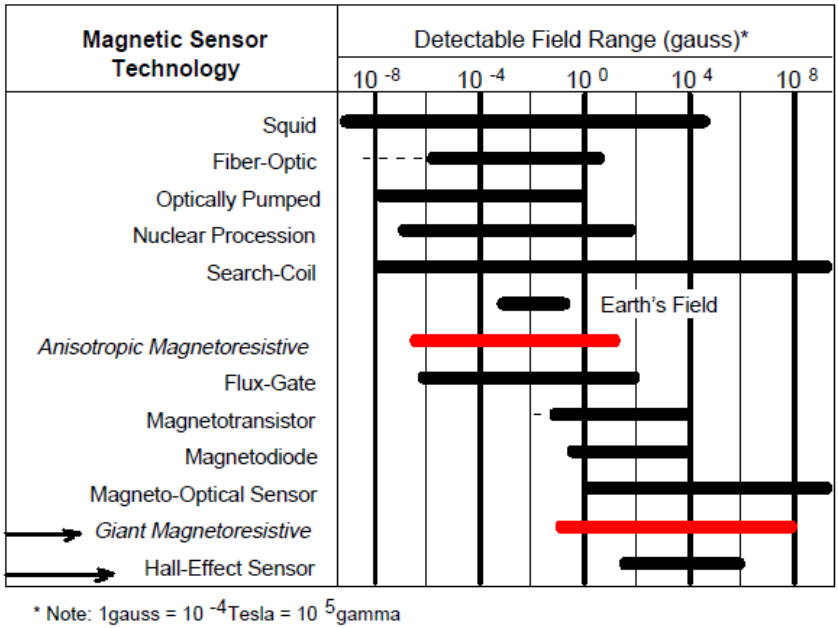

Scheme 6.1 *Various sensor technology.*

http://www.sensorsmag.com/sensors/electric-magnetic/a-new-perspective-magnetic-field-sensing-855

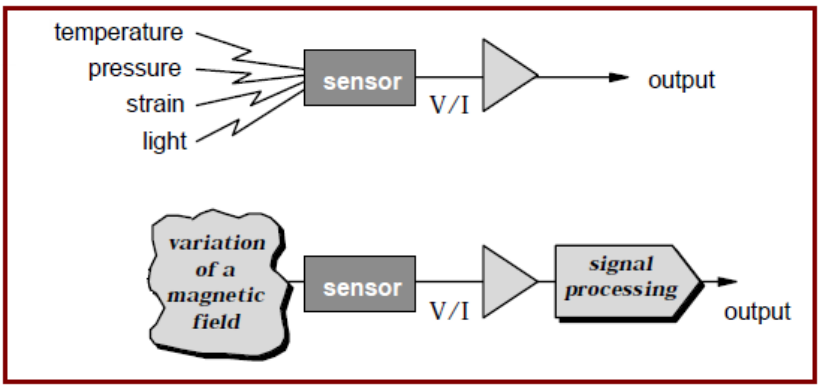

Fig. 6.10 *The magnetic field sensing.*

6.4 Hydrogen Storage

The use of hydrogen as the basis for a future sustainable energy economy with low carbon emissions is one of the worldwide interest in the time being. Production, Storage and utilization of hydrogen are the main factors for considering the economy of using these materials. It is significant scientific and technological challenges to satisfy these main factors. For hydrogen-fuel cell transportation use a suitable material for on-board storage should be able to store a high weight-percent and high volume density of hydrogen and rapidly discharge and charge the same amount of hydrogen at acceptable temperatures (typically around 50–100 ℃). This represents a particular challenging set of credentials for an ideal storage material and at present no known material meets these critical requirements.

According to Chen et al work [145] in 2002 the system Li_3N-Li_2NH-$LiNH_2$ could reversibly cycle hydrogen with a theoretical maximum of over 11wt% H_2. In practice, only cycling between lithium imide and amide is feasible at realistic pressures and temperatures. Ammonia, NH_3, is formed as portion of the H_2 desportion process. This dispotion occurred in two steps:

$$2LiNH_2+LiH \Rightarrow (Li_2NH+NH_3)+LiH$$

$$Li_2NH+(NH_3+LiH) \Rightarrow Li_2NH+LiNH_2+H_2$$

NH_3 absorption by LiH is a rapid and efficient process. However, in practice it is difficult to reduce NH_3 levels to below 200 ppm, a value that still is high enough to poison current fuel-cell operation.

David et al, [146] demonstrated from synchrotron X-ray diffraction refinement that the mechanism of the transformation between lithium amide and lithium imide during hydrogen cycling in the important Li-N-H hydrogen storage system is a bulk reversible reaction that occurs in a non-stoichiometric manner within the cubic anti-fluorite-like Li-N-H structure.

The hydrogen desorption and structural properties of the Li−Mg−N−H systems with different LiH/$Mg(NH_2)_2$ ratios are systemically investigated by Haiyan Leng et al. [147] The system with the LiH/$Mg(NH_2)_2$ ratio of 6/3 transforms into Li_2NH and MgNH, and then, the mixture forms an unknown phase by a solid−solid reaction, which presumably is the ternary imide $Li_2Mg(NH)_2$; the system with the LiH/$Mg(NH_2)_2$ ratio of 8/3 transforms into $4Li_2NH$ and Mg_3N_2 after releasing H_2 at T < 400 ℃; the system with the LiH/$Mg(NH_2)_2$ ratio of 12/3 transforms into $4Li_3N$ and Mg_3N_2 after releasing H_2 at T > 400 ℃, where the LiMgN phase is formed by the reaction between Li_3N and Mg_3N_2. The characteristics of the phase transformations and the thermal gas desorption behaviors in these Li−Mg−N−H systems could be reasonably explained by the ammonia mediated reaction model, irrespective of the difference in the LiH/$Mg(NH_2)_2$ ratios.

The combination of X-ray and neutron diffraction studies (see Fig. 6.11) led to a precise determination of the full crystal structure, which has been independently corroborated by computational studies as the most precise determination of a number of recent studies [149].

The maximum available weight percentage and the hydrogen capacity per volume are 10.6 wt.% and 96 kgm^{-3}, respectively. Chen *et al.* [150] recently showed that titanium chloride-doped LiAlH4 lowered the decomposition temperature of $LiAlH_4$, which resulted from the enhanced kinetics for a dehydriding cycle. Thus development of catalysts for the enhanced kinetics of LiAlH4 is very attractive since it can eliminate the need for high temperature and high pressure previously required for the rehydriding/dehydriding cycle.

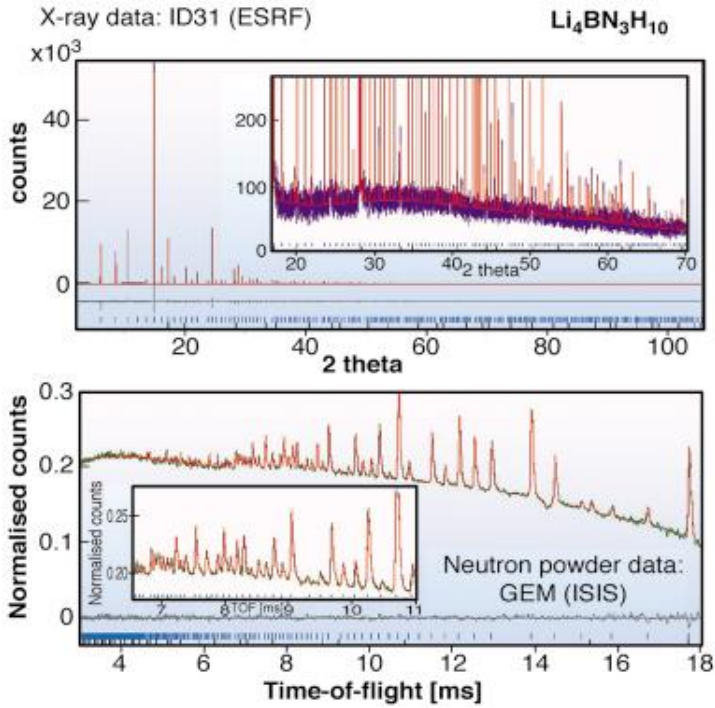

Fig. 6.11 *X-ray and neutron powder diffraction patterns of $Li_4BN_3H_{10}$. Both datasets are fitted simultaneously to high precision providing strong validation of all aspects of the crystal structure including hydrogen positions.*

Most promising future scenario is the hydrogen economy especial concerning ideal replacement in the transportation application. Hydrogen is the ideal means of energy storage, transportation and conversion in a comprehensive clean-energy concept. [151] It is non-polluting as its combustion only generates water. It is abundant and can be produced from a variety of conventional and renewable energy resources, mainly water which covers 71% of earth planet area. For these reasons, there is now world widespread agreement that hydrogen will play a key role in the developed countries energy policy towards the middle of the century. [152-154] However, the storage of hydrogen is still the bottleneck problem which faces its commercial application. Inefficient storage in liquid form is because of hydrogen very low boiling point around -250 ℃.

Add to that, its low density in the gaseous state requires storage in risky high-pressure vessels not accepted by safety regimes for mobile applications and in particular in the future "zero-emission vehicle" [155-160].

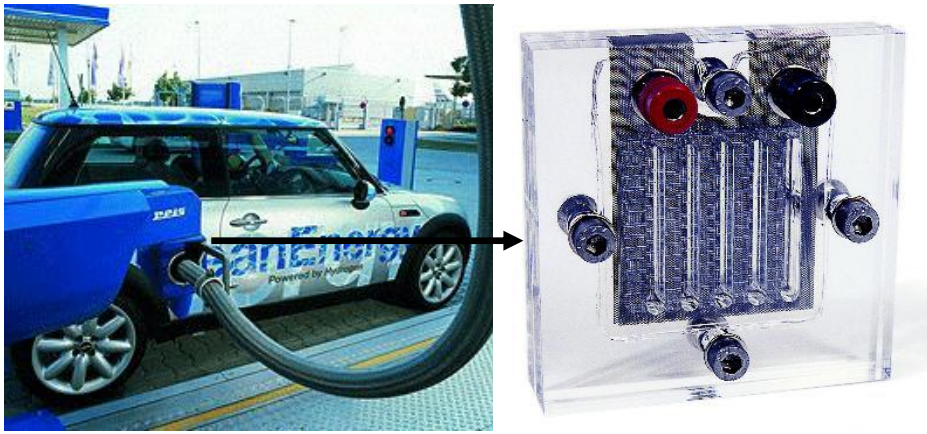

Hydrogen car fueling Material hydride design

Fig. 6.12 *Hydrogen fuel.*

Alternative safe offer has been introduced by storing hydrogen storage in matter for transportation. Several promising systems are under discussion: adsorbed hydrogen on nano-structures (nano tubes, metal organic frameworks), and hydrogen absorbed in metal hydrides (transition metal based hydrides, complex hydrides). [156-159] Requirements for hydrogen fuel tanks to be used in vehicles is put down by US Department Of Energy (DOE) which have been taken as international target for onboard application, at least 6 mass% hydrogen has to be stored (6.5 mass% and 62 kg H_2/m^3) in a time as short as 5-10 minutes which allows the vehicle to cut a distance of about 500Km. [160-170] Qualification for the carrier matter is to have high gravimetric and volumetric density, to be suitable for the already designed transport technologies. Achieving all of these targets in one hydrogen storage material system is not available in the present nevertheless, studding different storage material systems with different treatments,

like doping a catalyst and structure treatments already have improved some of them that they become promising for application. [161, 163] Examples are adsorbed nano-structures like carbon nanotubes and other carbon materials as well as absorbed in transition metal-based materials. Recently, intense interest has developed in light-weight complex hydrides such as alanates and borohydrides beside the peroviskites which newly appear on the scene of the hydrogen energy storage field. The above mentioned materials still need to adjust thermodynamics and kinetics properties to technical needs for on board application.

The peroviskite crystal structure is associated with unique octahedral with hydrogen atoms prefer to occupy. The noticed high mobility of hydrogen atoms in the peroviskite crystal structure can be used to improve the slow hydrogenation kinetics of some strongly bound light-metal-hydride system such as MgH_2 and possibly to design new alloy hydrides with desirable hydrogen-storage properties. [164-198]

References

[1] A. Abdel-Latif, A. Hassen C. Zybill, M. Abdel-Hafiez, S. Allam, Th. El-Sherbini, *Journal of Alloys and Compounds*, 452, (2008) 245.

[2] K. Uusi-Esko, J. Malm, N. Imamura, H. Yamauchi, M. Karppinen, *Materials Chemistry and Physics*, 112, (2008) 1029.

[3] I. A. Abdel-Latif, A. S. Khramov, V. A. Trounov, A. P. Smirnov, Sh. Sh. Bashkirov, V. V. Parfenov, E. A. Tserkovnaya, G. G. Gumarov, Z. Ibragimov, *Egypt. J. Solids*, V. 29, II, (2006) 341.

[4] A. Abdel-Latif, Th. El-Sherbini, *Journal of Material Science Indian Journal*, 6, (2010) 109.

[5] M. Fiebig, Th. Lottermoser, D. Fro ̈hlich, A. V. Goltsev, and R. V. Pisarev, *Nature*, 419, (2002) 818.

[6] N. A. Hill and K. M. Rabe, *Phys. Rev*. B 59, (1999) 8759.

[7] A. Sharan, J. Lettieri, Y. Jia, W. Tian, X. Pan, D. G. Schlom, and V. Gopalan, *Phys. Rev. B* 69, (2004) 1341.

[8] J. M. D. Coey, M. Viret, S. V. Molnar, *Advances in Phys*., 48, (1999) 167.

[9] A. Munoz, J. A. Alonso, M. J. Martinez-Lope, M. T. Casais and J. L. Martinez, M. T. Fernandez Diaz, *Phys. Rev. B* 62 (2000) 9498.

[10] Sh. Sh. Bashkirov, V. V. Parfenov, I. A. Abdel-Latif, L. D. Zaripova, *Journal of Alloys and Compounds*, 387, (2005) 70.

[11] K. Bouziane, A. Yousif, I. A. Abdel-Latif, K. Hricovini, C. Richter, *J. Appl. Phys.*, 97, (2005) 504.

[12] H. A. Salama, G. A. Stewart, D. H. Ryan, M. Elouneg-Jamorz and A. V. J. Edge, J. *Phys.; condens. Matter* 20, (2008).

[13] I. A. Abdel-Latif, *Arab. J. Nucl. Sc. Appl.*, Vol. 44, No 4, (2011).

[14] A. Hendi, I. A. Abdel-Latif, S. A. Saleh, *Journal of American Science*, 7(10) (2011) 749.

[15] A. Abdel-Latif, *Arab. J. Nucl. Sc. Appl.*, V. 43 No. 4 (2010) 243.

[16] A. Abdel-Latif, *AIP Conf. Proc.*, 1370, (2011), 108.

[17] S. Rößler, J. Jesudasan, K. Bajaj, P. Raychaudhuri, F. Steglich and S. Wirth, *Journal of Physics*: Conference Series 150 (2009) 042164.

[18] B. Martínez, L. Balcells, J. Fontcuberta, C. H. Cohenca and R. F. Jardim, *J. Appl. Phys*., 83, (1998) 7058.

[19] S. M. Dunaevsky, A. I. Kurbakov, V. A. Trounov, D. Yu. Chernyshov, V. V. Papov, V. V. Chernyshev, J. Roudriguez-Carvajal, *Solid State Phys.* (*Fiz. Tverd. Tela*) 40 (1998) 1271.

[20] I. A. Abdel-Latif, A. Kurbakov, A. Al-Hajry and V. A. Trounov, *Arab. J. Nucl. Sc. Appl*., Vol. 44, No 4, (2011) 7.

[21] G. Pang. et al., *Materials Research Bulletin* 38, 2003, 11-16.

[22] Z. F. Zi et al., *Journal of Magnetism and Magnetic Materials* 15, 2009, 2378-2381.

[23] S. Farhadi, et al, *Journal of Alloys and Compounds* 471, Issues 1–2, 2009, Pages L5-L8.

[24] R. F. C. Marques, et al, IEEE TRANSACTIONS ON MAGNETICS, VOL. 38, NO. 5, SEPTEMBER 2002 2892.

[25] Zhike Liu, Yajun Qi, *Journal of Materials Science: Materials in Electronics*, 21, 2010, 380-384.

[26] I A Abdel-Latif, *JOURNAL OF PHYSICS* 1(2012) 15-31.

[27] Dragan P. Uskokovic, Slobodan K. Milonjic, Djan I. Rakovic, *Materials Science Forum* 494 2005 155.

[28] V. Uskokovic, M Drofenik,. *Journal of Magnetism and Magnetic Materials*, 303, 2006, 214.

[29] Seyedeh Behnaz, Alireza Babaei, Abolghasem Ataie, *Rare Metal*s 2016 1-10.

[30] Gwan-Hyoung Lee and Shinhoo Kang, *J. Electrochem. Soc. 153 2006 H105-H109*.

[31] M. N. Iliev, M. V. Abrashev, H.-G. Lee, V. N. Popov, Y. Y. Sun, C. Thomsen, R. L. Meng and C. W. Chu, *Phys. Rev. B*, 57, No. 5 (1998) 2872.

[32] M. M. Rahman, A. Jamal, S. B. Khan, M. Faisal, *J. Phys. Chem. C 115* (2011) 9503-9510.

[33] Hayashi, H.; Torii, K., *J. Mater. Chem.* 2002, *12*, 3671-3676.

[34] S. A. El-Safty, A. A. Ismail, H. Matsunaga, T. Hanaoka, F. Mizukami, Adv. Funct. Mater. 18 (2008) 1485-1500.

[35] Y. Hakuta,; H. Ura,; H. Hayashi; K. Arai, *Mater. Lett.* 2005, *59*, 1387-1390.

[36] J Lu; Y Hakuta; H Hayashi; T Ohashi; T Nagase; Y Hoshi; K Sato; M Nishioka; T Inoue; S Hamakawa,. *J. Supercrit. Fluid*. 2008, *46*, 77-82.

[37] Buassi-Monroy, C. C. Luhrs, A. Chavez-Chavez, C. R. Michel, Materials Letters 58(5): 2004 716-718.

[38] J. L. G. Fierro, Metal Oxides: Chemistry and Applications; CRC Press: Boca Raton, FL, 2006.

[39] C. N. R Rao,.; B. Raveau, Transition metal oxides; VCH Publishers Inc.: New York, 1995.

[40] Livage, J.; Henry, M.; Sanchez, C. Prog. Solid State Chem. 1988, 18, 259-341.

[41] Niederberger, M.; Garnweitner, G. Chem.—Eur. J. 2006, 12, 7282-7302.

[42] Maneesha Gupta, Poonam Yadav, Wasi Khan, Ameer Azam, Alim H. Naqvi, R. K. Kotnala, Adv. Mat. Lett. 3(3) 2012, 220-225.

[43] M Lanki, A, Nourmohammadi, M., Feiz, Ferroelectrics. 448 2013: 123-33.

[44] E. P ́erez, Seminario, M ́etodos de Preparaci ́on de nanopart ́ıculas (Universidad de los Andes, M ́erida Venezuela, 2012.

[45] Z. A. Munir, J. B. Holt, J. Mater. Sci. 22 (1987) 710-714.

[46] E. Chinarro. E. Chinarro, B. Moreno, D. Martin, L. Gonzalez, E. Villanueva, D. Guinea y J. R. Jurado, Bol. Soc. Esp. Ceram. Vol 44 (2005) 105-112.

[47] Klaus D. Sattler., Handbook of Nanophysics: Nanoparticles and Quantum Dots, CRC press 2011.

[48] Qi et al, Nanoscale Research Letters 2011, 6: 466.

[49] Angew. Chem. Int. Ed. 2006, 45, 6564-6566.

[50] M. Yazdanbakhsh, H. Tavakkoli and S. M. Hosseini,, S. Afr. J. Chem., 2011, 64, 71-78.

[51] Sh. Sh. Bashkirov, V. V. Parfenov, I. A. Abdel-Latif, L. D. Zaripova, *Journal of Alloys and Compounds*, 387, (2005) 70.

[52] I. Farag, A. Mostafa, I. A. Abdel-Latif, *Egypt. J. Solids*, Vol. (30), No. (1), (2007) 149.

[53] A. Abdel-Latif, S. A. Saleh, Journal of Alloys and Compounds, Volume 530, 2012, PP. 116-120.

[54] Brinker, C. J., Scherer, G. W. Sol-Gel Science: The Physics and Chemistry of Sol-Gel Processing. Academic Press, London, 1990.

[55] A. Ghosh, J. R. Sahu, S. V. Bhat, C. N. R. Rao, *Solid State Sciences*, 11 (2009) 1639.

[56] L. Yue-Feng, W. Bei, Z. Hai-Wu, L. Xiang-Yang, GU Yu-Zong and Z. Wei-Feng., Chin. *Phys. Lett.*, 27, No. 5 (2010) 056801.

[57] S. Jandl, S. N. Barilo, S. V. Shiryaev, A. A. Mukhin, V. Yu. Ivanov and A. M. Balbahov, *J. Mag. Magn. Matter.* 264 (2003) 36.

[58] H. C. Gupta, V. Sharma, U. Tripathi and N. Rani, *J. Phys. Chem. Solids*, 66 (2005) 1314.

[59] Mart ńez, L. Balcells, J. Fontcuberta, C. H. Cohenca and R. F. Jardim, *J. Appl. Phys*., 83, (1998) 7058. D. Grossin, J. G. Noudem, *Solid State Sciences*, 6 (2004) 939.

[60] R. F. C. Marques, P. R. Abernethy, J. A. D. Matthew, C. O. Paiva-Santos, L. Perazolli, M. Jafelicci Jr., S. M. Thompson, *J. Magn. Magn. Mater.* 272-276 (2004) 1740.

[61] G. Li, G.-G. Hu, H.-D. Zhou, X.-J. Fan, X.-G. Li, *Mater. Chem. Phys*. 75 (2002) 101.

[62] I. Panagiotopoulos, N. Moutis, M. Ziese, A. Bollero, *J. Magn. Magn. Mater.*, 299 (2006) 94.

[63] B. I. Belevtsev, A. Ya. Kirichenk, N. T. Cherpak, G. V. Golubnichay, I. G. Maximchuk, E. Yu. Beliayev, A. S. Panfilov, J. Fink-Finowicki, J. Magn. Magn. Mater. 281 (2004) 97.

[64] V. Yu. Ivanov, A. A. Mukhin, V. D. Travkin, A. S. Prokhorov, A. M. Balbashov, *J. Magn. Magn. Mater.*, 258-259 (2003) 535.

[65] Y. Tomioka, H. Hiraka, Y. Endoh, Y. Tokura, *Phys. Rev. B* 74 (2006) 104420.

[66] F. Damay, N. Nguen, A. Maignan, M. Hervieu, B. Raveau, Solid State Commun. 98 (1996) 997.

[67] J. Rodriguez-Carvajal, *Physica B.* 192, (1993) 55.

[68] B. Van Aken, A. Meetsma and T. M Palstra, *Acta Cryst.* E57 (2001) i87-i89.

[69] C. Martin, A. Maignan, M. Hervieu, B. Raveau, *Phys. Rev. B* 60 (1999) 12191.

[70] T. Katsufuji, S. Mori, M Masaki, Y Moritomo, N Yamamoto and H Takagi, *Phys Rev* B 66, (2002) 134434.

[71] N. N. Greenwood and T. C. Gibb, *Mössbauer Spectroscopy*, Chapman and Hall, London, (1971), p. 273

[72] X. Fabreges, I. Mirebeau, P. Bonville, S. Petit, G. Lebras-Jasmin, A. Forget, G. Andr é, and S. Pailh ès, *Phys. Rev. B*, 78 (2008) 214422.

[73] J. B. Goodenough, J. Appl. Phys. 37 (3) (1996) 1415.

[74] R. Koc, H. U. Anderson, J. Eur. Ceram. Soc. 15 (9) (1995) 867.

[75] M. Viret, L. Ranno, J. M. D. Covy, Phys. Rev. B 55 (1997)8067.

[76] G. Venkataiah, Y. Kalyana Lakshmi, V. Prasad, P. Venugopal Reddy, J. Nanosci. Nanotechnol. 7 (2007) 2000.

[77] Z. F. Wu, Z. H. Wanga, Z. Bai, P. J. Li, H. Tian, L. Qiu, X. S. Wu, Y. W. Chen, J. Gao, J. Magn. Magn. Mater. 311 (2007) 623.

[78] J. B. Torrance, P. Lacorre, A. I. Nazzal, Phys. Rev. B 45 (1992) 8209.

[79] C. Krishnamoorthy, K. Sethupathi, V. Sankaranarayanan, R. Nirmala, S. K. Malik, J. Alloys Compd. 438 (2007) 1-7.

[80] L. I. Balcell, J. Fontcuberta, B. Martinez, X. Obadors, Phys. Rev. B5 (1998) R14697-R14700

[81] I. A. Abdel-Latif, A. S. Khramov, V. A. Trounov, O. P. Smirnov, Sh. Sh. Bashkirov, V. V. Parfenov, E. A. Tserkovnaya, G. G. Gumarov and Sh. Z. Ibragimov, Egypt. J. Solids, 29 (2006) 341.

[82] J. B. Torrance, P. Lacorre, A. I. Nazzal, Phys. Rev. B 45 (1992) 8209.

[83] G. Venkataiah, D. C. Krishna, M. Vithal, S. S. Rao, S. V. Bhat, V. Prasad, S. V. Subramanyam, P. Venugopal Reddy, Physica B 357 (2005) 370-379.

[84] S. H-ebert, C. Martin, A. Maignan, R. Retoux, M. Hervieu, N. Nguyen, B. Raveau, Phys. Rev. B65(2002)104420.

[85] K. De S. Majumdar, S. Giri "Low-temperature transport anomaly in the self doped manganite, $La_{0.9}Mn_{0.98}M_{0.02}O_3$ (M = 0, Fe, and Co) "Journal of Magnetism and Magnetic Materials" 322 (2010) 337–341.

[86] Arita Banerjee, et al, J. Appl. Phys. 91 (2002), 5212-5134.

[87] Y. Wang, Y. Sui, J. Appl. Phys. 104 (2008), 093703-1-093703-7.

[88] H. Muguorra, et al "J. Alloys compound, 509 (2011) 7710-7716.

[89] Yuanli, et al "Systematic investigation on structure stability and oxygen permeability of Sr-doped $BaCo_{0.7}Fe_{0.2}Nb_{0.1}O_3$ ceramic membranes" Journal of memberane cience 362 (2010) 460-470.

[90] A. M. M Farea, et al, Physica B 403 (2008) 684-701.

[91] M. M. El-Nahas, et al, Organic electronics. 7(2006) 260-270.

[92] S. R. Elliott, Philos, Mag. 36 (1977)1291.

[93] Pike G. F., Phys. Rev. B, 1572 (1972) 6.

[94] Michael. C. Martin and G. Shrane "magnetism and structure distortion in the $La_{0.7}Sr_{0.3}MnO_3$ mettalic ferromagnet" Physical Review B vol. 53, No. 21 (1996).

[95] M. Marezio, J. P. remeika "the crystal chemistry of the Rare earth orthoferrites" Acta Cryst. (1970) B 26.

[96] R. N. Jadhav, et al "Journal of Alloys and compounds" 507 (2010) 151-156.

[97] Anantharanan M. R, Sincthus., Tagtheesan S., Molini K. A., Kurian P., J. Phys. D. Appl. Phys. 32 (1999)1801.

[98] P. Kameli, H. Salamati, A. Aezami" Influence of grain size on magnetic and transport properties of polycrystalline $LaSrMnO_3$ manganites" Journal of Alloys and compounds 450 (2008) 7-11.

[99] N. F. Moot, E. A. Davis, Electronic Processes in Noncrystalline Materials (Clarenden Press, Oxford, 1979).

[100] G. Demazeau, M. Pouchard, and P. Hagenmuller, J. Solid state Chem. 9. 202 (1974).

[101] G. Venkataiah, P. Venugopal Reddy " structure, magnetic and magneto transport behavior of some Nd-based perovskite manganites" Solid state communications 136 (2005) 114-119.

[102] Y. Kalyana. Laskshmi, et al "influence of sintering temperature and oxygen stoichiometry on electrical transport properties of $La_{0.67}Na_{0.3}MnO_3$" Journal of Alloys and compounds 470 (2009) 67-74.

[103] Yue Ying, Jiyu Fan, Lipi et al, "the effect of Ca doping in $Nd_{0.7}Sr_{0.3}MnO_3$ system" solid state communication 144 (2007) 300-304.

[104] M. Tlili, M. Bejar, E. Dhahri, et al, Materials characterization 62 (2011) 243-247.

[105] Y. Ying, T. W. Eom, N. V. Dai, Y. P. Lee, Journal of Magnetism and Magnetic Materials 323 (2011) 94–100.

[106] L. Capriotti, R. Vaia, A. Cuccoli, and V. Tognetti, Phys. Rev. B 58, (1998)273.

[107] L. Capriotti, A. Cuccoli, V. Tognetti, P. Verrucchi, and R. Vaia, *Phys. Rev. B* 60, (1999)7299.

[108] http://en.wikipedia.org/wiki/Magnetic_refrigeration

[109] J. B. Goodenough, Phys. Rev. 100 (1955) 564.

[110] V. K. Pecharsky, K. A. Gschneidner, A. O. Tsokol, Rep. Prog. Phys. 68 (2005) 1479.

[111] H. Zhu, H. Song, Y. H. Zhang, Appl. Phys. Lett. 81 (2002) 3416.

[112] A. H. Morrish, The Physical Principles of Magnetism (Wiley, New York, 1965, Chap. 3.

[113] A. M. Tishin, K. A. Gschneidner, Jr., and V. K. Pecharsky, Phys. Rev. B59, (1999) 503.

[114] Z. B. Guo, Y. W. Du, J. S. Zhu, H. Huang, W. P. Ding, D. Feng, Phys. Rev. Lett. 78 (1997) 1142.

[115] LEE *et al.*, *Phys. Rev. B*, B 71, (2005) 180413 (R).

[116] Manh-Huong Phan, Seong-Cho Yu, Journal of Magnetism and Magnetic Materials 308 (2007) 325.

[117] E. Bruck, J. Phys. D: Appl. Phys. 38 (2005) R381.

[118] E. Warburg, Ann. Phys. 13 (1881) 141.

[119] V. K. Pecharsky, K. A. Gschneidner, Phys. Rev. Lett. 78 (1997) 4494.

[120] X. Hu, B. G. Shen, J. R. Sun, G. H. Wu, Phys. Rev. B 64 (2001) 132412.

[121] Z. B. Guo, Y. W. Du, J. S. Zhu, H. Huang, W. P. Ding, D. Feng, Phys. Rev. Lett. 78 (1997) 1142.

[122] Young Sun, X. Xu, Yuheng Zhang, J. Magn. Magn. Mater. 219 (2000) 183.

[123] X. Bohigas, J. Tejada, E. Del Barco, X. X. Zhang, M. Sales, Appl. Phys. Lett. 73 (1998) 390.

[124] Young Sun, Wei Tong, Yuheng Zhang, Journal of Magnetism and Magnetic Materials 232 (2001) 205.

[125] I. A. Abdel-Latif, et al., AIP Conf. Proc., 1370, (2011) 158.

[126] V. K. Pecharsky, K. A. Gschneidner, Appl. Phys. Lett. 70 (1997) 3299.

[127] K. A. Gschneidner Jr., V. K. Pecharsky, J. Appl. Phys. 85 (1999) 5365.

[128] Mahn-Huong Phan, Seong-Cho Yu, A. N. Ulyanov, M. K. Lachowicz, Material Science Vol 21 No 1 (2003) 133.

[129] N. H. Luong, N. T. M. Phuong, P. T. Hien, H. N. Nhat, L. H. Hoang, N. Chau, N. H. Hai, VNU Journal of Science, Mathematics - Physics 24 (2008) 30.

[130] W. Chen, L. Y. Nie, W. Zhong, Y. J. Shi, J. J. Hu, A. J. Li, Y. W. Du, J. Alloys. Compd. 395 (2005) 23.

[131] Manh-Huong Phan, Hua-Xin Peng, Seong-Cho Yu, N. D. Tho, H. N. Nhat, N. Chau, Journal of Magnetism and Magnetic Materials 316 (2007) e562.

[132] C. R. H. Bahl, D. Velázquez, K. K. Nielsen, K. Engelbrecht, K. B. Andersen, R. Bulatova, N. Pryds, Appl. Phys. Lett. 100 (2012) 121905.

[133] T. Mukherjee, S. Michalski, R. Skomski, D. J. Sellmyer, and Ch. Binek, Phys. Rev. B 83 (2011) 214413.

[134] B. Li, W. J. Ren, X. W. Wang, H. Meng, X. G. Liu, Z. J. Wang, and Z. D. Zhang Appl. Phys. Lett. 96 (2010) 102903.

[135] U. Legait, F. Guillou, A. Kedous-Lebouc, V. Hardyb, M. Almanza, Inter. Joural of refrigeration 37 (2014) 147.

[136] M. Wali, R. Skini, M. Khlifi, E. Dhahri and E. K. Hlil, Dalton Trans., 44 (2015), 12796-12803.

[137] Kalipada Das' Tapas Paramanik, I. Das, Journal of Magnetism and Magnetic Materials 374 (2015) 707-710.

[138] S. El. Kossy, S. Ghadhbane, S. Mnefigue, E. Dhahri and E. K. Hlil, Journal of Magnetism and Magnetic Materials 395 (2015) 134-142.

[139] I. A. Abdel-Latif, Adel A. Ismail, H. Bouzid, A. Al-Hajry, Journal of Magnetism and Magnetic Materials 293 (2015) 233.

[140] Dominik Straßel, Peter Kopietz, and Sebastian Eggert, Phys. Rev. B 91 (2015) 134406.

[141] http://www.gizmag.com/giant-magnetocaloric-effect-in-fridges/15624/

[142] *Physical Review* (http://www.gizmag.com/giant-magnetocaloric-effect-in-fridges/15624/)

[143] E. Dhahri, M. Bejar, S. Othmani, A. Tozri and E. Hlil, *Journal of Magnetism and Magnetic Materials* 321 (2009), Issue: 7, Pages: 777.

[144] http://spectrum.ieee.org/semiconductors/memory/spintronic-memories-to-revolutionize-data-storage (by Salah M. Bedair, John M. Zavada, Nadia El-Masry).

[145] Magnetoresistive Random Access Memory (MRAM) By James Daughton Copyright © 2/4/00.

[146] http://www.sensorsmag.com/sensors/electric-magnetic/a-new-perspective-magnetic-field-sensing-855

[147] Riabov M. V., Stranadko E. Ph., Volkova N. N., *J. Laser Medicine*, 6 № 1 (2002) 12.

[148] Y. Dimitriev, Y. Ivanova, R. Iordanova *Journal of the University of Chemical Technology and Metallurgy, 43, 2, 2008, 181-192*.

[149] Rajashree Rajagopal, J. Mona, S. N. Kale, Tanushree Bala, Renu Pasricha, P. Poddar, M. Sastry, and B. L. V. Prasad, Darshan C. Kundaliya and S. B. Ogale, APPLIED PHYSICS LETTERS 89, 023107 (2006).

[150] S. Rößler, J. Jesudasan, K. Bajaj, P. Raychaudhuri, F. Steglich and S. Wirth, *Journal of Physics*: Conference Series 150 (2009) 042164.

[151] S. M. Dunaevsky, A. I. Kurbakov, V. A. Trounov, D. Yu. Chernyshov, V. V. Papov, V. V. Chernyshev, J. Roudriguez-Carvajal, *Solid State Phys.* (*Fiz. Tverd. Tela*) 40 (1998) 1271.

[152] K. Y. Choi, P. Lemmens, G. Guntherdodt, M. Pattabiraman, G. Balakrishnan, D. McK. Paul and M. R. Les, *J. Phys. Condens. Matter* 15 (2003) 3333.

[153] W. J. Li, Bo. Zhang and W. Lu, *Solid State Communications*, 140 (2006) 503.

[154] L. Martin-Carrron, A. de Andr ́es, M. J. Martıner-Lope, M. T. Casais, J. A. Alonso, *J. Alloys Compounds*, 323 (2001) 494.

[155] M. N. Iliev, M. V. Abrashev, H.-G. Lee, V. N. Popov, Y. Y. Sun, C. Thomsen, R. L. Meng and C. W. Chu, *Phys. Rev. B*, 57, No. 5 (1998) 2872.

[156] Ghosh, J. R. Sahu, S. V. Bhat, C. N. R. Rao, *Solid State Sciences*, 11 (2009) 1639.

[157] L. Yue-Feng, W. Bei, Z. Hai-Wu, L. Xiang-Yang, GU Yu-Zong and Z. Wei-Feng., Chin. *Phys. Lett.*, 27, No. 5 (2010) 056801.

[158] S. Jandl, S. N. Barilo, S. V. Shiryaev, A. A. Mukhin, V. Yu. Ivanov and A. M. Balbahov, *J. Mag. Magn. Matter.* 264 (2003) 36.

[159] H. C. Gupta, V. Sharma, U. Tripathi and N. Rani, *J. Phys. Chem. Solids*, 66 (2005) 1314.

[160] Grossin, J. G. Noudem, *Solid State Sciences*, 6 (2004) 939.

[161] R. F. C. Marques, P. R. Abernethy, J. A. D. Matthew, C. O. Paiva-Santos, L. Perazolli, M. Jafelicci Jr., S. M. Thompson, *J. Magn. Magn. Mater.* 272-276 (2004) 1740.

[162] G. Li, G.-G. Hu, H.-D. Zhou, X.-J. Fan, X.-G. Li, *Mater. Chem. Phys*. 75 (2002) 101.

[163] Panagiotopoulos, N. Moutis, M. Ziese, A. Bollero, *J. Magn. Magn. Mater.*, 299 (2006) 94.

[164] B. I. Belevtsev, A. Ya. Kirichenk, N. T. Cherpak, G. V. Golubnichay, I. G. Maximchuk, E. Yu. Beliayev, A. S. Panfilov, J. Fink-Finowicki, J. Magn. Magn. Mater. 281 (2004) 97.

[165] V. Yu. Ivanov, A. A. Mukhin, V. D. Travkin, A. S. Prokhorov, A. M. Balbashov, *J. Magn. Magn. Mater.*, 258-259 (2003) 535.

[166] Y. Tomioka, H. Hiraka, Y. Endoh, Y. Tokura, *Phys. Rev. B* 74 (2006) 104420.

[167] Damay, N. Nguen, A. Maignan, M. Hervieu, B. Raveau, Solid State Commun. 98 (1996) 997.

[168] C. Martin, A. Maignan, M. Hervieu, B. Raveau, *Phys. Rev. B* 60 (1999) 12191.

[169] N. Greenwood and T. C. Gibb, *Mössbauer Spectroscopy*, Chapman and Hall, London, (1971), p. 273.

[170] X. Fabreges, I. Mirebeau, P. Bonville, S. Petit, G. Lebras-Jasmin, A. Forget, G. André, and S. Pailhès, *Phys. Rev. B*, 78 (2008) 214422.

[171] M. V. Riabov, E. Ph. Stranadko, N. N. Volkova, *J. Laser Medicine*,6 № 1 (2002) 12.

[172] P. Chen, Z. T. Xiong, J. Z. Luo, J. Y. Lin, K. L. Tan, *Nature* 420, 302-304 (2002).

[173] W I F David et al. Journal of the American Chemical Society 129 (6), 1594 (2007.

[174] Haiyan Leng,* Takayuki Ichikawa, and Hironobu Fujii, *J. Phys. Chem. B*, 2006, *110* (26), pp 12964-12968.

[175] D. J. Siegel, C. Wolverton, V. Ozolins, *Phys. Rev. B* 75, 014101 (2007).

[176] Y. E. Filinchuk, K. Yvon, G. P. Meisner, F. E. Pinkerton, M. P. Balogh, *Inorg. Chem.* 45, 1433-1435, (2006); T. Noritake, M. Aoki, S. Towata, A. Ninomiya, Y. Nakamori, and S. Orimo, *Appl. Phys. A: Mater. Sci. Process.* 83, 277 (2006).

[177] J. Chen, N. Kuriyama, Q. Xu, H. T. Takeshita, and T. Sakai, J. Phys. Chem. B 105, 11214 (2001).

[178] Greene, D. L., Hopson, J. L., J. Energy Policy, 2006; 34: 515-31.

[179] Eunju Jun, Yong Hoon Jeong, Soon Heung Chang, International Journal of Energy Research, Volume 32, Issue 4, Date: 25 March 2008, Pages: 318-327.

[180] J. Van Mierlo, G. Maggetto, Fuel Cells, Volume 7, Issue 2, Date: April, 2007, Pages: 165-173.

[181] Ewald Wicke, Chemie Ingenieur Technik, Volume 54, Issue 1, Date: 1982, Pages: 41-52.

[182] Sarmistha R. Majumdar, Review of Policy Research, Volume 22, Issue 2, Date: March 2005, Pages: 157-169.

[183] Edward Dean Tate Jr, Jessy W. Grizzle, Huei Peng, International Journal of Robust and Nonlinear Control, Volume 18, Issue 14, Date: 25 September 2008, Pages: 1409-1429.

[184] Vincent Bérubé, Gregg Radtke, Mildred Dresselhaus, Gang Chen, International Journal of Energy Research, Volume 31, Issue 6-7, Date: May 2007, Pages: 637-663.

[185] sSamuel S. Mao, Xiaobo Chen, International Journal of Energy Research Volume 31, Issue 6-7, Date: May 2007, Pages: 619-636.

[186] T. E. Rufford, Z. H. Zhu, G. Q. Lu, Developments in Chemical Engineering and Mineral Processing, Volume 14, Issue 1-2, Date: 2006, Pages: 85-99.

[187] Yuichi Mitsutake, Masanori Monde, Kengo Shigetaka, Shigeru Tsunokake, Tatsuya Fuura, Heat Transfer - Asian Research, Volume 37, Issue 3, Date: May 2008, Pages: 165-183.

[188] Paul Vermeulen, Emile F. M. J. van Thiel, Peter H. L. Notten, Chemistry - A European Journal, Volume 13, Issue 35, Date: December 7, 2007, Pages: 9892-9898.

[189] US Department of energy, 2006 Annual Proceedings, Hydrogen Storage. http://www.sc.doe.gov.

[190] Gerardo Jose La O', Hyun Jin In, Ethan Crumlin, George Barbastathis, Yang Shao-Horn, International Journal of Energy Research, Volume 31, Issue 6-7, Date: May 2007, Pages: 548-575.

[191] Karran Woan, Georgios Pyrgiotakis, Wolfgang Sigmund, Adv. Mater. 2009, 21, 1-7.

[192] John Lloyd; John Mitchinson. *"What's the commonest material in the world". QI*: The Book of General Ignorance. *Faber & Faber*. ISBN 0-571-23368-6.

[193] Hui Wu, Wei Zhou, Terrence J. Udovic, John J. Rush, and Taner Yildirim, *Chem. Mater.*, 2008, 20 (6), 2335.

[194] Elizabeth J. Duplock, 1 Matthias Scheffler, 2 and Philip J. D. Lindan1, Physical Review Letters, Vol. 92 (22), (2004), 225502.

[195] Serguei Patchkovskii, John S. Tse, Sergei N. Yurchenko, Lyuben Zhechkov, Thomas Heine §, and Gotthard Seifer, PNAS, vol. 102 (30), 2005, 10439.

[196] N. Ismail, A. A. El-Meligi, M. Uhlemann, A. Gebert, J. Eckert, L. Schultz, Hydrogenation of Zr-Cu-Ni-Al-Pd metallic glass by electrochemical means, Journal of Alloys and Compounds, in press, (2009).

[197] N. Ismail, M. Uhlemann, A. Gebert, J. Eckert, L. Schultz, Effects of electrochemical hydrogenation of Zr-based alloys with high glass-forming ability, Intermetallics 10 (2002) Nr. 11-12, S. 1207-1213.

[198] N. Ismail, A. Gebert, M. Uhlemann, J. Eckert, L. Schultz, Effect of hydrogen on $Zr_{65}Cu_{17.5}Al_{7.5}Ni_{10}$ metallic glass, Journal of Alloys and Compounds 314 (2001) Nr. 1-2, S. 170-176.

Short Introduction to the Book

In the recent years, a lot of interests have been devoted to research on the 3d-4f oxides, within perovskites-like structure. The great attention increased due to the potential applications of such oxides in spintronics devices, clean magnetic refrigerators, magnetic sensors, hydrogen storage technology, magnetic recording media and ferroelectromagnets. This book highlights on the recent advances in such materials: synthesis, crystal structure, electrical, magnetic and thermal properties, besides the technological applications.

Brief Biography of the Author

Dr Ihab Abdel-Latif Abdel-Latif, the author of this book, is an Associate Professor of Physics in Reactor Physics Department, Nuclear Research Center, Cairo, Egypt and Physics Department, Najran University, Najran, Saudi Arabia. He defended PhD dissertation at Kazan Federal University, Kazan Russia in 2003 and published 66 publications and books in the field of advanced materials and neutron physics.

To order additional copies of this book, please contact:
Science Publishing Group
book@sciencepublishinggroup.com
www.sciencepublishinggroup.com

ISBN 978-1-940366-62-3
9 781940 366623 >
Price: US $80